NASA/CR-1999-209524

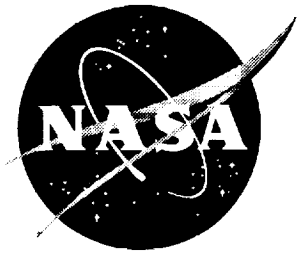

Low Speed Analysis of Mission Adaptive Flaps on a High Speed Civil Transport Configuration

Victor R. Lessard
ViGYAN, Inc., Hampton, Virginia

December 1999

The NASA STI Program Office . . . in Profile

Since its founding, NASA has been dedicated to the advancement of aeronautics and space science. The NASA Scientific and Technical Information (STI) Program Office plays a key part in helping NASA maintain this important role.

The NASA STI Program Office is operated by Langley Research Center, the lead center for NASA's scientific and technical information. The NASA STI Program Office provides access to the NASA STI Database, the largest collection of aeronautical and space science STI in the world. The Program Office is also NASA's institutional mechanism for disseminating the results of its research and development activities. These results are published by NASA in the NASA STI Report Series, which includes the following report types:

- TECHNICAL PUBLICATION. Reports of completed research or a major significant phase of research that present the results of NASA programs and include extensive data or theoretical analysis. Includes compilations of significant scientific and technical data and information deemed to be of continuing reference value. NASA counterpart of peer-reviewed formal professional papers, but having less stringent limitations on manuscript length and extent of graphic presentations.

- TECHNICAL MEMORANDUM. Scientific and technical findings that are preliminary or of specialized interest, e.g., quick release reports, working papers, and bibliographies that contain minimal annotation. Does not contain extensive analysis.

- CONTRACTOR REPORT. Scientific and technical findings by NASA-sponsored contractors and grantees.

- CONFERENCE PUBLICATION. Collected papers from scientific and technical conferences, symposia, seminars, or other meetings sponsored or co-sponsored by NASA.

- SPECIAL PUBLICATION. Scientific, technical, or historical information from NASA programs, projects, and missions, often concerned with subjects having substantial public interest.

- TECHNICAL TRANSLATION. English-language translations of foreign scientific and technical material pertinent to NASA's mission.

Specialized services that complement the STI Program Office's diverse offerings include creating custom thesauri, building customized databases, organizing and publishing research results . . . even providing videos.

For more information about the NASA STI Program Office, see the following:

- Access the NASA STI Program Home Page at ***http://www.sti.nasa.gov***

- Email your question via the Internet to help@sti.nasa.gov

- Fax your question to the NASA STI Help Desk at (301) 621-0134

- Telephone the NASA STI Help Desk at (301) 621-0390

- Write to:
  NASA STI Help Desk
  NASA Center for AeroSpace Information
  7121 Standard Drive
  Hanover, MD 21076-1320

NASA/CR-1999-209524

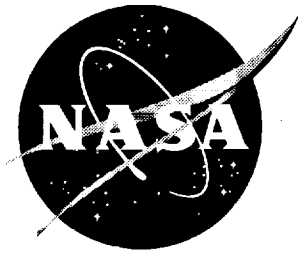

Low Speed Analysis of Mission Adaptive Flaps on a High Speed Civil Transport Configuration

Victor R. Lessard
ViGYAN, Inc., Hampton, Virginia

National Aeronautics and
Space Administration

Langley Research Center
Hampton, Virginia 23681-2199

Prepared for Langley Research Center
under Contract NAS1-19672

December 1999

Available from:

NASA Center for AeroSpace Information (CASI)
7121 Standard Drive
Hanover, MD 21076-1320
(301) 621-0390

National Technical Information Service (NTIS)
5285 Port Royal Road
Springfield, VA 22161-2171
(703) 605-6000

Low Speed Analysis of Mission Adaptive Flaps on a High Speed Civil Transport Configuration

Summary

Thin-layer Navier-Stokes analyses were done on a high speed civil transport configuration with mission adaptive leading-edge flaps. The flow conditions simulated were Mach=0.22 and Reynolds number of 4.27 million for angles-of-attack ranging from 0° to 18°. Two turbulence closure models were used. Analyses were done exclusively with the Baldwin-Lomax turbulence model at low angle-of-attack conditions. At high angles-of-attack where considerable flow separation and vortices occurred the Spalart-Allmaras turbulence model was also considered. The effects of flow transition were studied. Predicted aerodynamic forces, moments and pressures are compared to experimental data obtained in the 14- by 22-Foot Subsonic Tunnel at NASA Langley. The forces and moments correlated well with experimental data in terms of trends. Drag and pitching moment were consistently underpredicted. Predicted surface pressures compared well with experiment at low angles-of-attack. Above 10° angle-of-attack the pressure comparisons were not as favorable. The two turbulent models affected the pressures on the flap considerably and neither produced correct results at the high angles-of-attack.

Introduction

The overall design of a high speed civil transport will be dictated by the supersonic cruise flight condition. Only a small percentage of the flight time will be at subsonic take-off and landing conditions with some time allocated for holding patterns around airports. A greater amount of subsonic flying may occur over land if the sonic boom noise is environmentally disruptive. Since the high speed civil transport is designed mainly for cruise, the wing shape is likely to be a low aspect ratio delta or cranked-delta type wing tailored for supersonic speeds with low drag and low sonic boom characteristics. The disadvantage of this wing design is that it is inefficient for take-off and landing scenarios. Improved aerodynamic performance in terms of increased maximum lift coefficient, C_{Lmax}, and increased lift-to-drag ratio, L/D, are needed for reduced engine noise, shorter take-off distances, slower runway speeds and faster climb and descent rates similar to the conventional transport aircraft of today. Hence, there is a considerable amount of experimental and computational research being done by NASA and industry in developing a high-lift system for subsonic conditions which will have a minimal impact on the supersonic cruise efficiency and at the same time enable the aircraft to land and take-off at most airports.

The objective of this paper is to predict the aerodynamic performance and flow field characteristics of a high-lift device on a generic high speed civil transport configuration. The high-lift device is a leading-edge mission adaptive (MA) flap system which was previously tested in NASA Langley's 14- by 22-Foot Subsonic Tunnel [ref. 1]. The MA flap system was tested on a crank-delta wing/body model with inboard and outboard leading-edge sweep angles of 71° and 50°, respectively. The flap system was designed by NASA using a linearized-theory code [refs.

2,3,4] based on potential flow solutions of a zero-thickness lifting surface. It was designed for a lift coefficient of 0.45 with trailing-edge flaps deflected at 10°/10°/12.9°, from inboard to outboard respectively. The objective of the leading-edge flap system was to reduce flow separation by keeping the leading edge of the flap aligned with the local upwash field at the design lift coefficient. This resulted in a considerable amount of twist and camber on the flaps. During the tunnel test, the flap system was shown to improve the low-speed, high-lift performance characteristics although flow separation was suspected at the designed condition.

The ability to predict flow separation and other nonlinear effects can play a key role in improving the overall flap design and the high-lift performance characteristics of a high speed transport. Computational fluid dynamics (CFD) methods which solve the Navier-Stokes equations can capture the surface and off-body viscous and other nonlinear effects in the flow field which makes it ideal for detailed flap analysis. Navier-Stokes computations for wing/body configurations have become practical with the increasing computer processor speeds and memory capabilities as well as the maturing CFD methods. An advantage of three dimensional Navier-Stokes calculations is that the nonlinear viscous effects are captured without some of the problems associated with panel and potential flow solvers coupled with boundary layer equations. Some of boundary layer coupling problems include determining correct boundary layer edge conditions, surface boundary conditions and predicting what happens after flow separation. Hence, solving the Navier-Stokes equations is the approach taken in this study with the objective of predicting the aerodynamic performance and flow field characteristics of a leading-edge MA flap system on a generic configuration.

Symbols

c	wing chord
$\bar{c}$	mean aerodynamic chord
c_{local}	local projected flap chord
C_D	drag coefficient
C_L	lift coefficient
C_M	pitching moment coefficient
M	freestream Mach number
P_t	normalized total pressure
$P_{t\infty}$	normalized freestream total pressure
Re_L	Reynolds number per unit length
T	freestream temperature, °R
y^+	turbulent boundary layer Reynolds number
α	angle-of-attack, deg.
η, ξ, ζ	curvilinear coordinate directions

Abbreviations

BL	butt line of model
CPU	central processing unit
FV	mission adaptive flap vortex
FSV	mission adaptive flap secondary vortex
HLV	hinge-line vortex
IPV	inboard primary vortex

ISV	inboard secondary vortex
LE	leading edge of wing
MA	mission adaptive
MS	model station
RL	reattachment line
SL	separation line
TR1, TR2, TR3	flap transition regions 1, 2 and 3

Experimental Aspects

The numerical results in this paper are compared to test data obtained from the Langley 14- by 22-Foot Subsonic Tunnel [ref. 1]. The wind tunnel test investigated two leading-edge flap systems; one was designed to capture and exploit a LE vortex and the other was designed to maintain attached flow. The attached-flow flap system (which will be referred to as the mission adaptive (MA) flap throughout the paper) is numerically studied in this paper. The tunnel test conditions of interest were M=0.22, Re_L=1.39x10^6 /ft., T=555°R and -2°≤ α ≤ 20°. A transition strip was placed 1.5 inches from the leading edge of the entire wing, but it was never determined if the flow along the leading edge transitioned from laminar to turbulent at the strip location, or somewhere else. The uncertainty of a transition location presented considerable difficulties in predicting the correct flow physics on the flap especially at the higher angles-of-attack where vortical flow existed. This will be discussed in more detail in the Results and Discussion section of the paper.

Geometry definition:

A plan-view schematic of the analyzed geometry is shown in figure 1. This configuration will be referred to as the 71-50 MA for the rest of the paper. The overall geometric characteristics of the model are given in table 1. Note, the wing reference area is defined by the planform projection of the cruise wing where the inboard leading edge line and the outboard trailing edge line extended toward the centerline. The gross area is the entire wing planform area. The inboard and outboard MA leading-edge flaps are blended together at the crank such that no gap exists when deflected. The small leading-edge radius of the inboard part of the wing transitions to a sharp leading edge on the outboard. The inboard leading-edge flap deflection varies linearly from approximately 16° inboard to 18.5° approaching the crank, and the outboard flap deflection was at a constant 21°. The model was tested with several different trailing-edge flap deflection angles of 0°, 10°, 12.9°, and 20°. Since this study focused mainly on the flow over the MA flaps, the 0° trailing-edge flap deflection configuration was chosen for the numerical model.

Pressure tap locations on the model are shown in figure 2 as dotted lines and are numbered 1 through 9. The lines of pressure taps will be referred to as strips. The strips 1 to 5 are on the inboard upper surface of the mission adaptive flap perpendicular to the leading edge. The x and y locations of the taps nearest to the leading edge are included in figure 2. Strips 6 and 7 are on the inboard wing section and they include pressure taps on both the upper and lower surfaces. Strips 8 and 9 are on the outboard wing section and the associated taps are on the upper surface only. Strips 6 through 9 will be referred to as butt-line strips and their spanwise locations are also given in figure 2.

Table 1:

Aspect Ratio	2.116
Reference Area, ft.^{2}	10.664
Gross Area, ft.^{2}	11.005
Span, ft.	4.750
Centerline Root Chord, ft.	5.288
Tip Chord, ft.	0.529
Mean Aerodynamic Chord, ft.	3.071
Moment Reference Center, ft. x y z	 6.018 0.0 0.0
Leading Edge Sweep, degrees	
Inboard Wing	71.0
Outboard Wing	50.0

Grid Generation

The surface grid was generated by NASA Langley's geometry laboratory, GEOLAB group, using a CAD system definition of the 71-50 MA configuration (see fig. 3). Part of the wind tunnel sting support system connected to the base of the model's fuselage is included in the numerical model. The sting was modeled for two reasons. First, it made grid generation simpler because it eliminated some of the difficulties in generating a volume grid around a fuselage with a flat base, and, second the sting effects the flow over the wing trailing-edge to some extent and should be

accounted for numerically. The grid at the base of the fuselage is blended into the support sting. This differed from the actual step that existed in the wind tunnel model due to the flat fuselage base meeting the sting. The volume grid was generated using an interactive grid tool package (GRIDGEN). A discretization of the entire flow field around the geometry was done using a domain decomposition approach. The domain was split into two domains (or blocks) by a constant x-coordinate plane at the wing apex and fuselage intersection location. A body-fitted structured grid is generated for each block where the upstream block (containing the forebody) has a C-O type topology and the downstream block (containing the fuselage/wing and sting/wake) has a H-O type topology (see fig. 4). The above blocking strategy was done for efficient grid point distribution and geometry resolution. The first block consisted of 41 points streamwise (ξ or I-direction), 49 points around the forebody (η or J-direction) and 57 points away from the surface (ζ or K-direction), giving a total of 114,513 points. The downstream block had 129 points streamwise, 129 points around the wing (and wake) surface and 57 points away from the surface, totaling 948,537 points. The total number of points in the global domain was 1,063,050.

The far field boundary extended (10.833 ft.) 3.5 $\bar{c}$ upstream, (6.449 ft.) 2.1 $\bar{c}$ downstream and (10.833 ft.) 3.5 $\bar{c}$ away from the surface. The normal spacing at the surface of the grid was approximately 8.3×10^{-6} ft., which resulted in nondimensional turbulent y+ values of approximately 1.5. In the normal direction, grid point stretching was done with a hyperbolic tangent function.

Numerical Aspects

Analysis Code:

All computations were done using a Navier-Stokes solver (CFL3D), developed by J.L. Thomas et al. [ref. 5]. The CFL3D solver has been extensively used and validated by researchers and is noted for its robustness and accuracy as an upwind scheme as well as for its multigridding and multiblock capabilities [refs. 6,7,8]. Details of the governing equations and the computational method used in the CFL3D code are presented in the above references. The governing equations solved are the three-dimensional, Reynolds-averaged, compressible thin-layer Navier-Stokes equations. The thin-layer Navier-Stokes equations are considered valid for high Reynolds number flow because the viscous effects are limited to a thin-layer near the surface. If the full Navier-Stokes equations were used the viscous terms would not be properly evaluated since the computational grid for a full configuration is normally too coarse in regions away from the surface [ref. 9]. Hence, the flow away from the surface is treated essentially as rotational inviscid. The state equations are written assuming the ideal gas assumption. Molecular viscosity is calculated using the Sutherland's law and the Stokes' hypothesis. For the closure of the governing equations the Reynolds stresses are modeled using a chosen turbulence model. The governing equations are discretized in such a way to be consistent with conservation laws in integral form.

An implicit, finite volume, upwind approach is used to solve the governing equations. Roe's flux-difference splitting is used to construct the upwind differences for the convective and the pressure terms. The spatial derivatives are written conservatively as a flux balance across the cell, and the shear stress and heat transfer terms are centrally differenced. Spatial approximate factorization, and Euler backward integration after linearization in time, results in the solution

through 5x5 block-tridiagonal matrix inversions in three directions. An approximate diagonal form of the spatial factors is employed to reduce computational time. The convergence rate is accelerated using a multigrid full-approximation scheme (FAS) [ref. 10]. The accuracy of the solution algorithm is second-order spatially and first-order temporally.

Turbulence Models:

Two turbulence closure models are considered in this paper; they are Baldwin-Lomax (B-L), and Spalart-Allmaras (S-A). The baseline calculations were done with the B-L closure model. The B-L model is a two layer algebraic eddy viscosity model developed for use in two- and three-dimensional Navier-Stokes calculations [ref. 11]. In general, the B-L model performs well for attached flow but is inadequate for separated and recirculation regions [ref. 12]. A modification made by D. Degani and L.B. Schiff [ref. 13] was included in the model to account for vortical flow near the surface. The second model developed by P.R. Spalart and S.R. Allmaras is a one-equation turbulence model. The model was derived "using empiricism and arguments of dimensional analysis, Galilean invariance, and selective dependence on the molecular viscosity" [ref. 14]. The model is localized in the sense that the solution at a point is not dependent on another point, which makes the model compatible with grids of any structure and with Navier-Stokes solvers of two and three dimensions. It is considered robust and converges to steady state rapidly.

Transition Method:

For the wind tunnel test, transition grit was placed 1.5 inches from the entire leading-edge of the model. Since no measurements were made to determine if the flow transitioned or not, the

actual location of the flow transition was never determined, which made accurate numerical predictions difficult. In order to study the effects of transition flow on a delta-wing leading-edge flap system, a simple numerical technique was employed. The technique involved simply turning off the turbulence model for cells located in a predefined area. Two approaches were used to implement this method. The first approach set the off or laminar region based on the surface grid lines where beginning and ending grid indices defined the region. Choosing the indices for the laminar region was to some extent arbitrary because the grid lines did not exactly follow the transition strip used in the experiment. For this approach two cases were considered and are given in table 2. The I-index indicates a streamwise point location on the grid and the J-index indicates a spanwise point location on the grid. For case TR1 the laminar region extended from the leading-edge to approximately the hinge-line on the upper surface of the inboard MA flap. The laminar region of case TR2 extended from the leading-edge to approximately mid-chord of the inboard MA flap.

The second approach closely mimicked the intended tripping of the flow in the experiment. The turbulence model was turned off for cells located upstream of the leading-edge transition location of 1.5 inches. Hence, the upstream cells are computed as laminar. The 1.5 inch distance from the leading-edge was approximate because the turbulence model was applied to entire grid cells and the correct distance was dependent on the grid topology and cell sizes.

Table 2: Transition Information

Approach	Case Name	I-begin index	I-end index	J-begin index	J-end index	Distance from LE
I	TR1	1	57	60	85	$\sim c_{local}$
I	TR2	1	57	60	80	$\sim c_{local}/2$
II	TR3	---	---	---	---	1.5 in.

Boundary Conditions:

The boundary conditions are specified explicitly in the CFL3D algorithm. At the solid boundaries, the conditions of no-slip and impermeability with zero-normal-gradient for pressure and temperature are imposed for the Navier-Stokes calculations. Along the wake surface a flow-through boundary condition was set. Here the wake surface refers to a grid plane behind the trailing edge of the wing and not the true physical wake. Locally one-dimensional characteristic boundary conditions are used in the farfield. First-order extrapolation for the conserved variables are used at the downstream boundary. The reflection boundary condition is used at the centerline symmetry plane. A time-flux conservation approach is used across the patched surface (or zonal interface) between two grid blocks. This procedure consists of interpolating to the cell centers of one grid assuming a bilinear or biquadratic variation of the flux within the cells of the other grid [ref. 15].

Convergence Criteria:

All solutions were run to a steady state condition which was determined when the L-2 norm of the residual decreased approximately four orders of magnitude and the lift coefficient was "constant". Calculations were done using a Courant-Friedrichs-Lewy (CFL) number of 1.0 and three levels of multigrid V-cycles were used to increase the convergence rate. Mesh sequencing with multigridding was used to initialize the flow and to speed up convergence rate. An example of a typical convergence history curve for a single solution is shown in figure 5 for the case of $\alpha=8°$ and Mach=0.22. The lift predicted on the medium grid level is approximately the same as on the fine level, which is an indirect indication that the fine grid level is sufficient for resolving the flow. The total CPU time on the CRAY-YMP super computer was 10.56 hours in which

approximately 40% of the time was spent on the coarser mesh sequencing levels.

Flow Conditions:

The flow conditions at which the high speed transport configuration with mission adaptive flaps was analyzed were M=0.22, Re_L=1.39x10^6/ft., and T=555°R. Solutions were computed for angles-of-attack of 0° through 18°. Since it was the original intent of this study to rely solely on the Baldwin-Lomax (B-L) turbulence model for the computations the solutions obtained with the B-L turbulence model are referred to as the baseline solutions. Due to some unfavorable B-L results with respect to surface pressure comparisons at the higher angles-of-attack, various transition locations for the Baldwin-Lomax model were tried. The Spalart-Allmaras (S-A) turbulence model was used for a limited number of calculations at higher angles-of-attack in an attempt to improve the results. A list of the calculations done are given in table 3.

Table 3:

Turbulence Model	α
Laminar	10°, 14°
Baldwin-Lomax (B-L)	0° - 18°
B-L & TR1	10°, 12°, 18°
B-L & TR2	12°
B-L & TR3	12°, 14°
Spalart-Allmaras (S-A)	12°, 14°, 16°
S-A & TR3	12°

Results and Discussions

Forces and Moments:

Predictions of the aerodynamic coefficients of lift, C_L, pitching moment, C_M, and drag, C_D, are compared with experiment in figures 6 through 9. The baseline predictions using the Baldwin-Lomax turbulence model are shown in figures 6a, 7a, 8a and 9a. The results obtained at moderately high angles-of-attack using the different flow transition locations and the Spalart-Allmaras turbulence models are compared with the baseline B-L model and experiment in figures 6b, 7b, 8b and 9b. The B-L C_L distribution compares well with experiment up to an angle-of-attack of 14°, and the nonlinear lift curve characteristics due to the vortical flow are accurately predicted. After α=14°, the computational C_L values are underpredicted. For the B-L model, the lift coefficient predictions did not improve at the high angles-of-attack (i.e. α=10.1°, 11.9°, 14.1°, 16.1°, 18.0°) with the different transition cases (i.e. B-L &TR1, TR2, TR3). Furthermore, the solutions obtained with the S-A turbulence model with and without transition deviated the most from the experimental values (see fig. 6b).

The computed baseline pitching moment, shown in figure 7a, is lower than experiment for all angles-of-attack; however, the general nonlinear trend is the same. In general, it is difficult to predict the correct magnitude of the pitching moment for a cranked-delta wing geometry with flaps because the location of flow separation and strength of the vortices greatly influence the center of pressure on the wing. And with respect to the Navier-Stokes calculations, the predicted state of separated and vortical flow is dependent on the grid resolution, the boundary layer transition model, and the turbulence model which, for the most part, all need to be improved. There are two locations in the B-L pitching moment curve where its apparent slope changes

similar to the experimental data. The first slope change, at α=8°, will be shown to correspond to the development of the hinge-line vortex and the second, at α=13°, will be shown to occur with the development of a strong flap vortex and a primary inboard vortex. The pitching moment coefficient computed using the B-L model plus the three transition cases and the S-A turbulence model do not vary significantly from the standard B-L results (see fig. 7b) except for the S-A with transition TR3 case at α=11.9°.

The predicted C_D and drag polar are plotted with experimental data in figures 8 and 9. The predicted B-L C_D curve is similar to experiment; however, the drag is underpredicted for most angles-of-attack except at α=12° (see fig. 8a). The minimum and maximum percent difference between the experimental and B-L C_D were 3.18% and 5.7% at α=0° and α=18°, respectively. The differences in terms of drag counts are 5.8 and 110.4 at α=0° and α=18°, respectively. No considerable improvement in the prediction of C_D is achieved with the B-L plus transition models or the S-A turbulence model at the higher angles-of-attack (see fig. 8b). The shape of the baseline B-L drag polar is consistent with experiment and compares well over the entire angle-of-attack range (see fig. 9a). The predicted drag polar data obtained with different transition and turbulence models are shown in figure 9b plotted with experiment and the baseline predictions. Again, the use of B-L with transition and S-A with and without transition did not improve the drag polar predictions.

Pressure Comparisons and Flow Physics:

In this section, the predicted surface pressures, surface flow and off-body total pressure contours and velocity vectors are all discussed simultaneously in such a manner as to try to better explain the predicted vortical flow phenomena associated with MA flaps on a cranked-delta wing.

The pressures strips on the surface of the wing are designated 1 through 9 where strips 1 through 5 are on the inboard MA flap perpendicular to the leading-edge. The pressure plots for these strips are normalized by the local projected flap chord. Experimental pressure data exist only for the upper surface of the flap. Strips 6 through 9 are butt-line strips (i.e. chordwise on the wing) and when plotted are normalized by the local wing chord. Experimental pressures exist on both the upper and lower surfaces of the inboard wing for strips 6 and 7. On the outboard wing section there are only upper surface experimental pressures for strips 8 and 9.

Overall, as was the case with the integrated force and moment results, there is good agreement between predicted and experimental C_P values for angles-of-attack from 0° to 8° (see figs. 10-13). For these angles-of-attack the baseline B-L turbulence model is used exclusively in the analysis of the flow field since a good correlation is obtained with this model. The computed C_P values on the upper surface of the flap compare quite well with experiment, which was expected since the flow on the upper surface of the flap should be mostly attached for the low angles-of-attack.

Figures 14 and 15 show the flow over the upper and lower surfaces of the wing in terms of surface limiting streamlines for α=4.0°, 6.0°, and 8.0°. The limiting streamlines were computed at the first grid point off the surface. A visual guide for interpreting these streamlines is shown below. A key used for labeling the different streamline features discussed in this paper is given in table 4.

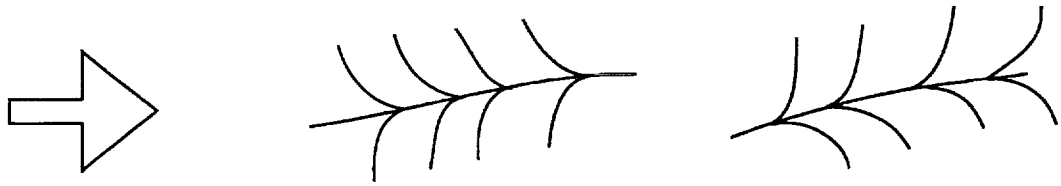

Table 4:

Flow feature	KEY
Hinge-Line Vortex	HLV
MA Flap Vortex	FV
MA Flap Secondary Vortex	FSV
Inboard Primary Vortex	IPV
Inboard Secondary Vortex	ISV
Leading Edge	LE
Separation Line	-SL
Reattachment Line	-RL

The lower surface limiting streamlines at α=4° show flow separation at the leading-edge and a flow reattachment line on the undersurface of the flap indicating the existence of a vortex (see fig. 15). This vortex can also be seen on the lower surface near the leading edge at the predicted pressure strips 2-5 where the C_P values are negative, which indicates a low pressure region (see fig. 11a). This low pressure region is caused by the acceleration of the induced cross flow between the core of the vortex and the surface. At α=6° the computed lower surface leading-edge vortex develops further downstream near the crank and does not appear in the C_P plots shown in figure 12a. On the upper surface at α=6° the surface flow is on the verge of separating, which is evident by the coalescing of the streamlines near the inboard MA flap hinge-line (see fig. 14b). At α=8° the predicted flow separates near the inboard MA flap hinge-line and rolls up into a counter-rotating vortex (i.e. rotating from outboard to inboard). The flow then reattaches inboard of the wing near the fuselage. Experimentally, the hinge-line vortex crosses pressure strip 7, which is

evident by the suction pressure near 0.5 x/c in the pressure plot (see fig. 13b). Computationally this vortex is seen as the second suction peak at strip 7, at 0.375 x/c. In figure 14c, the rotating flow of the vortex is seen on the surface as s-shaped surface limiting streamlines, which occur inboard of the separation line. The gradual smoothing of the s-shaped streamlines downstream indicates that the vortex becomes more elongated and dissipative as it approaches the trailing-edge of the wing. The shape and path of the hinge-line vortex can be further analyzed by studying the off-body normalized total pressure contours, P_t, at several model stations (MS) shown in figure 16. The total pressure loss is defined as the difference between free-stream total pressure, $P_{t\infty}$, and P_t in the vortex core. The total pressure loss decreases in the core as the flow propagates downstream, which is consistent with the decreasing strength of the vortex. It is not known whether the vortex or its location is captured correctly because of the limited number of experimental pressure taps located inboard of the hinge-line.

Though, by in large, the C_P comparisons for the butt-line strips 6 through 9 correlate well for angles-of-attack from 0° to 8° except for the existence several discrepancies (see figs. 10b, 11b, 12b and 13b). These are discussed next. On the lower surface of the wing for strip 6 near 35% chord there is an experimental suction pressure peak which is not predicted computationally. The actual cause of the lower pressure region was never determined; however, it may have been due to an open cavity in the lower wing surface. Likewise, for strip 7 on the upper surface at 80% chord, another experimental suction pressure region (not predicted numerically) occurs which may have been caused by a discontinuity on the surface at a trailing-edge flap hinge-line (the flap was set at 0°). The pressures on the upper surface of the outboard wing (strips 8 and 9) compare remarkably well. This is due to the well behaved attached flow which can be seen in figure 14.

Three different flow analyses are done at an angle-of-attack of 10.1° (fig. 17): (1) a completely

laminar case, (2) a completely turbulent case using the B-L turbulence model (i.e. baseline case), and (3) a transition case (TR1) with the B-L turbulence model. In this study the baseline B-L turbulence model analysis is initially done and comparisons of predicted surface C_P values with experiment are poor. The biggest discrepancy is seen on the upper surface at 20% of the local flap chord (i.e. .20 s/c_{local}). The experiment indicates a strong flap vortex which is not captured by the baseline computations. Both experimental and computational suction pressures on the flap decrease downstream toward the wing crank. The reduction of suction pressure downstream are related to both the dissipation of the vortex and the relative location of the vortex core away from the surface. The baseline computations with the B-L model do capture an inboard primary vortex and a weaker MA flap vortex. The MA flap vortex is between 30% and 40% of the local flap chord and is apparent as small suction peaks in the surface pressures for strips 3, 4 and 5 (see fig. 17a). The existence of this vortex also appears in the computed surface limiting streamlines (see fig. 18b) and the off-body normalized P_t contours at three model stations on the MA flap (see fig. 19). The flap vortex is elongated and close to the surface. There is no reattachment line associated with the flap vortex because the flow is within the recirculating flow of a larger inboard primary vortex. The flow separation line of the inboard primary vortex occurs at the leading-edge instead of at the hinge-line. Similar to the $\alpha=8°$ case, the experimental C_P values on the butt-line strip 7 show some evidence of the inboard primary vortex crossing the strip at 0.6 x/c (see fig. 17b). The inboard primary vortex can be seen in terms of surface limiting streamlines and in the off-body P_t contours (see figs. 18b and 19). In the surface limiting streamlines, separation and reattachment lines exist between the flap vortex and the primary vortex which suggests that a secondary vortex has formed. This secondary vortex develops because of adverse pressure gradient outboard of the primary vortex. The secondary vortex is elongated and is located near

the surface (partially in the boundary layer) and could be considered a recirculating flow.

The flow analysis is repeated for α=10.1° with no turbulence model to establish if the flow on sections of the flap behaves similar to laminar flow. In this case the laminar calculation captures the strength (magnitude of the suction pressures) and the location of the flap vortex (see fig. 17a). The flap vortex flow can be seen in figure 18a in terms of surface limiting lines. A small leading-edge secondary vortex develops outboard of the flap vortex. This secondary vortex is not seen in the experimental pressure data due to the limited number of pressure taps on the flap. The surface pressure coefficients are similar to experiment for strips 1 through 7 (see fig. 17). However, the pressure coefficients for the outboard strips 8 and 9 differ considerably from experiment. On the outboard wing, the predicted flow separates near the hinge-line and at approximately 67% of the tip chord, and for both separations vortical flow exists as evidenced by the two pressure suction peaks at strip 9. As shown in figure 18, these two vortices are also seen in the limiting streamlines. The inboard primary vortex reattachment line is in the same approximate location as in the baseline analysis. And similarly, the secondary vortex separation and reattachment lines lie between the flap vortex and the inboard primary vortex. Also, there is flow separation occurring at the trailing edge in the proximity of the inboard vortex separation line.

The good C_P comparisons on the MA flap for the fully laminar case led to a third analysis in which a transition location is defined along with the B-L turbulence model. The transition case TR1 as described in the Transition Methods section of the paper is used. The laminar region includes most of the upper surface of the inboard MA flap. The new predicted C_P values for all the strips are closer to experiment than the completely turbulent flow case or the laminar case (see fig. 17). The C_P comparisons indicate that the flow probably transitioned on the flap during the experiment at α=10.1°, and it may be fortuitous that the semi-arbitrary laminar region chosen

produces such good results. The surface streamlines show a more complex surface flow when compared to the laminar and turbulent cases (fig. 18c). A flap vortex along with its secondary vortex exist similar to the laminar case. However, the flow associated with the flap vortex reattaches midway on the flap, separates again at the hinge-line, and then rolls up into a hinge-line vortex rotating in the same direction as the inboard primary vortex. The hinge-line vortex does not develop until about a third of the distance from the apex to the crank. Again, there is a secondary vortex (or recirculating region) associated with the inboard primary vortex noted by the separation line inboard of the hinge-line. The multiple vortices can be seen in the off-body normalized P_t contours (see fig. 20) and the cross-flow velocity vectors (see fig. 21). Note, the flap vortex exists at the three model stations MS=3.8, 5.0 and 5.9, which is not the case for the baseline analysis (see fig. 19). Also, the flow is well behaved on the outboard wing section similar to the fully turbulent case.

At α= 11.9° generating a solution with good correlation to experimental surface pressure measurements proves to be more elusive. Results are originally obtained with computations using the baseline B-L turbulence model and with B-L plus transition cases TR1, TR2 and TR3 (see fig. 22). The laminar region for case TR1 includes most of the upper surface of the inboard MA flap and for case TR2 it extends from the leading edge to approximately the mid-chord of the flap. The laminar region of case TR3 includes 1.5 inches from the inboard and outboard leading-edges. The experimental surface C_P values indicate a possible vortex along the leading edge of the MA flap. The width of the surface influenced by the suspected vortex spans the entire local flap chords at strip locations 1, 2 and 3 and approximately half of the local flap chords at locations 4 and 5. It is important to remember that the actual length of the local flap chord increases from the apex to the crank. In general, at this angle-of-attack the B-L model with and without transition cases does

not predict the C_P trends or values correctly on the MA flap. Although, the B-L model without transition matches the experimental trends at strip 4, the comparisons for the butt-line strips 6, 7 and 8 are only fair and for strip 9 they are poor. The predicted off-body normalized P_t contours at several model stations show the flap vortex as well as the inboard vortex for the baseline calculation (see fig. 23). Figure 24 shows a close-up view of the flap vortex at several model stations in terms of cross-flow velocity vectors.

A comparison of the surface flows for the four computations using the B-L model with and without transition are shown in figure 25. There are two common flow features between them; namely, the flap vortex and the inboard primary vortex. The differences between these two flow features relate to the strength and locations of the vortices and the extent of secondary vortices that are paired with them. The strength and locations of the flap vortices can be determined from the surface lines and from pressure strips 1-7 in figure 22. The baseline B-L solution has the weakest flap vortex based on surface suction pressure. The influence of the secondary vortices (or recirculating flows) associated with the inboard primary vortex and the flap vortex are greater for the baseline B-L solution. The inboard secondary separation and reattachment lines begin at the apex and extend all the way to the trailing edge of the wing (see fig. 25a). The reattachment line of the inboard secondary vortex is slightly inboard of the hinge-line. For the transition case, TR1 multiple vortices develop beginning at the apex; one forms into inboard primary vortex and the other develops into a smaller vortex with its separation line on the upper surface of the MA flap. The smaller vortex is engulfed by the inboard vortex downstream of the apex and at approximately the same location that the MA flap vortex develops. Secondary vortex separation and reattachment lines are located in between the flap vortex and the inboard primary vortex. This secondary vortex begins approximately one half the distance between the apex and the crank. For

the transition cases, TR2 and TR3, there are multiple vortices emanating from the leading-edge; one forms into the inboard vortex and the other forms into the MA flap vortex. Secondary vortices do not develop from the inboard primary vortices; this differs from the baseline B-L case and the B-L plus transition, TR1 case.

Since the different flow transition locations result in numerous variations in flow physics at α=11.9°, it is believed that a better method of predicting or simulating transitional flow in highly three dimensional flows is needed along with better turbulence models. Predicting transition is beyond the scope of this investigation; however, implementing a second turbulence model is done to try to improve the results further. The Spalart-Allmaras (S-A) turbulence model is used for calculations at angles-of-attack of 11.9°, 14.1°, and 16.1°. The baseline B-L model, along with transition cases TR2 and TR3, are also computed at α=14.1°. At α=11.9° the S-A model with transition TR3 is used to determine transition effects on surface pressures.

The surface C_P values computed using the S-A turbulence model are shown in figure 26 for the angle-of-attack case of 11.9°. The B-L results and flow transition case (TR3) for the S-A model are also shown for comparison purposes. In general, the C_P values obtained with the S-A model agree better with the experimental data trends. For the most part, the suction pressures are under predicted on the upper surface of the MA flap for strips 1, 2 and 3. The C_P values on the butt-line strips 6 through 9 compare well with experiment and are considerably better than the B-L and S-A with transition TR3 results. The C_P values obtained with the S-A turbulence model with transition (TR3) deviate considerably from experiment for all strips. The above results, along with the B-L model plus transition results, suggest that the experimental flow is mostly turbulent (at α=11.9°) and that the flow does not transition from laminar to turbulent at the trip location of 1.5 inches from the leading-edge. Computed surface limiting streamlines obtained

with the B-L and S-A turbulence models are shown in figure 27. There are several dissimilarities between the S-A and B-L surface limiting lines (fig. 27a,b). For instance, the surface streamlines from the S-A solution show no secondary vortex associated with the inboard primary vortex while the streamlines of the B-L solution show a definite secondary vortex which begins at the wing apex. Also, a secondary vortex does not develop outboard of the flap vortex in the S-A solution. The flow on the outboard wing is predominantly in the streamwise direction for the S-A solution while the B-L outboard surface flow is mostly spanwise. This spanwise flow is influenced by the inboard MA flap vortex, which enlarges as it propagates toward the outboard wing section. Furthermore, a secondary vortex evolves from the outboard vortex, which is evident by the secondary separation line. Some of these differences can also be seen from the off-body total pressure contours at selected model stations (see figs. 23 and 28). Note, the inboard vortex core is further off the surface for the S-A solution than for the B-L solution. Further analysis of the flow on the inboard flap can be obtained from the cross-flow velocity vectors at the three model stations, which correspond to the off-body P_t contours (see figs. 24 and 29). The B-L cross-flow velocity vectors show two vortices above the MA flap rotating in the same direction at MS=3.8 and 5.0 which are not seen by the surface streamlines. At model station MS=5.9 the two vortices evolve into a single elongated vortex. The crossflow velocity vectors of the S-A results show only a single small vortex near the leading edge.

The B-L and S-A computational results for angles-of-attack of 14.1° and 16.1° are shown in figures 30, 31 (pressure plots) and 32, 33 (surface flow) and 34, 35 (off-body total pressures) and 36, and 37 (cross-flow velocity vectors). The off-body P_t contours and velocity vectors are plotted for the S-A turbulence model only since this model produced the better results and because the B-L flow physics are similar to that of the α=11.9° case. The results are briefly stated below to give

the reader a sense of the flow variations due to turbulence models and transition locations. Overall, the S-A model C_P values match the trends of the experimental values better for both α=14.1° and 16.1°. The C_P values on the MA flap are underpredicted. The B-L turbulence model results at α=14.1° are mixed. The C_P values obtained with the B-L model are poor for strips 1-3 but, for strips 4 and 5 they agree relatively well with experiment. The C_P values obtained with B-L model with transition case TR3 are similar to experiment at strip 5. At α=14.1° the C_P values on the outboard wing at butt-line strip 8 for the B-L transition cases TR2 and TR3 compare better than the S-A C_P values. However, at α=16.1° the S-A C_P values match experiment better for all strips except 8 and 9 where both turbulence models yield poor comparisons. The variations in surface limiting streamlines of the B-L and S-A computations are shown in figures 32 and 33. A note of interest is that there is no secondary vortical flow at α=14.1° for the S-A turbulence results even though there is a secondary vortex which develops from the inboard primary vortex at α=11.9° and 16.1°. The most significant differences between the B-L (plus TR2, TR3) and the S-A surface limiting streamlines occur on the outboard wing section. There is considerably more vortical flow occurring in the B-L solution, and the S-A turbulence model appears to be more dissipative with respect to vortical flow. Further details of the vortical flows can be seen in the off-body total pressure contours (see figs. 34, 35) and the cross-flow velocity vectors on the MA flap at several model stations (see figs. 36, 37).

Conclusions

Navier-Stokes calculations are an invaluable resource for analyzing the flow physics of the mission adaptive flap system on a high speed research configuration. The analyses show the complicated vortical flow physics that is associated with high-lift devices on a crank-delta wing configuration at high angles of attack. Overall aerodynamic forces and moments are predicted well. The flow predictions are deficient in the areas of the MA flap and the outboard wing section for the angles-of-attack above 10.1°. At the high angles-of-attack the varying agreement in the predicted C_P values between the B-L and S-A turbulence models (with and without transition) for local areas highlight the inadequacies of the models and transition methods used. The Baldwin-Lomax turbulence model works well for the low angles-of-attack where the flow is attached on the MA flap and the outboard wing. With the development of vortical flow on the MA flap, the model loses its effectiveness; however, applying transition case TR1 to the baseline at α=10.1° produced improved correlation. Hence, knowing or predicting the transition locations can play a critical role in obtaining better results. At the higher angles-of attack the Spalart-Allmaras turbulence model correlates better with experiment with respect to surface pressures, but tended to be more dissipative in the area of the MA flap vortical flow. Therefore, this model underpredicted the suction pressure on the flap surface below the vortex and consequently underpredicted lift.

This study did not address the effects of grid topology and local grid distribution using the different turbulence models and transition scenarios. However, it was not the intent of this study to be all encompassing but to be more of an application problem in which a variety of results are obtained on a single grid.

Research was supported by the National Aeronautics and Space Administration under Contract No. NAS1-19672.

References

1. Campbell, Bryan A.; Kemmerly, Guy T.; Kjerstad, Kevin J.; and Lessard, Victor R.: ***Subsonic Investigation of Leading-Edge Flaps Designed for Vortex- and Attached-Flow on a High-Speed Civil Transport Configuration***, NASA/TM-1999-209701, 1999.

2. Carlson, Harry W. and Darden, Christine M.: ***Validation of a pair of computer codes for estimation and optimization of subsonic performance of simple hinged-flap systems for thin swept wings***, NASA TP-2828, 1988.

3. Carlson, Harry W.; Darden, Christine M.; and Mann, Michael J.: ***Validation of a Computer Code for Analysis of Subsonic Aerodynamic Performance of Wings With Flaps in Combination With a Canard or Horizontal Tail and Application to Optimization,*** NASA TP-2961, January 1990.

4. Carlson, Harry W. and Walkley, Kenneth B.: ***An Aerodynamic Analysis Computer Program and Design Notes for Low Speed Wing Flap Systems,*** NASA Contractor Report 3675, March 1983.

5. Thomas, J.L. and Newsome, R.: ***Navier-Stokes Computations of Lee-Side Flows over Delta Wings***, AIAA-86-1049, 1986.

6. Taylor, S.L.; Kjelgaard, S.O.; Weston, R.P.; Thomas, J.L.; and Sellers, W.L. III: ***Experimental and Computational Study of the Subsonic Flow About a 75 Deg. Swept Delta Wing***, AIAA-87-2425, August 1987.

7. Vatsa, V.N.; Thomas, J.L.; and Wedan, B.W.: ***Navier-Stokes Computations of Prolate Spheroids at Angle of Attack***, AIAA-87-2627-CP, 1987.

8. Thomas, J.L.; Taylor, S.L.; and Anderson, W.K.: ***Navier-Stokes Computations of Vortical Flows Over Low Aspect Ratio Wings***, AIAA-87-0207, 1987.

9. Fujii, K. and Schiff, L.B.: ***Numerical Simulation Of Vortical Flows Over A Strake-Delta Wing***, AIAA-87-1229, June 1987.

10. Anderson, W.K. and Thomas, J.L.: ***Multigrid Acceleration of the Flux Split Euler Equations***, AIAA-86-0274, 1986.

11. Baldwin, B.S. and Lomax, H.: ***Thin Layer Approximation and Algebraic Model for Separated Turbulent Flows***, AIAA-78-257, 1978.

12. Rumsey, C.L. and Vatsa, V.N.: ***A Comparison of the Predictive Capabilities of Several Turbulence Models Using Upwind and Central-Difference Computer Codes***, AIAA-93-0192, January 1993.

13. Degani, D. and Schiff, L.B.: ***Computation of Supersonic Viscous Flows Around Pointed Bodies at Large Incidence***, AIAA-83-0034, January 1983.

15. Spalart, P.R. and Allmaras, S.R.: ***A One-Equation Turbulence Model for Aerodynamic Flows***, AIAA-92-0439, January 1992.

16. Biedron, R.T. and Thomas, J.L.: ***A Generalized Patched-grid Algorithm With Application to F-18 Forebody With Actuated Control Strake***, AIAA-91-3291.

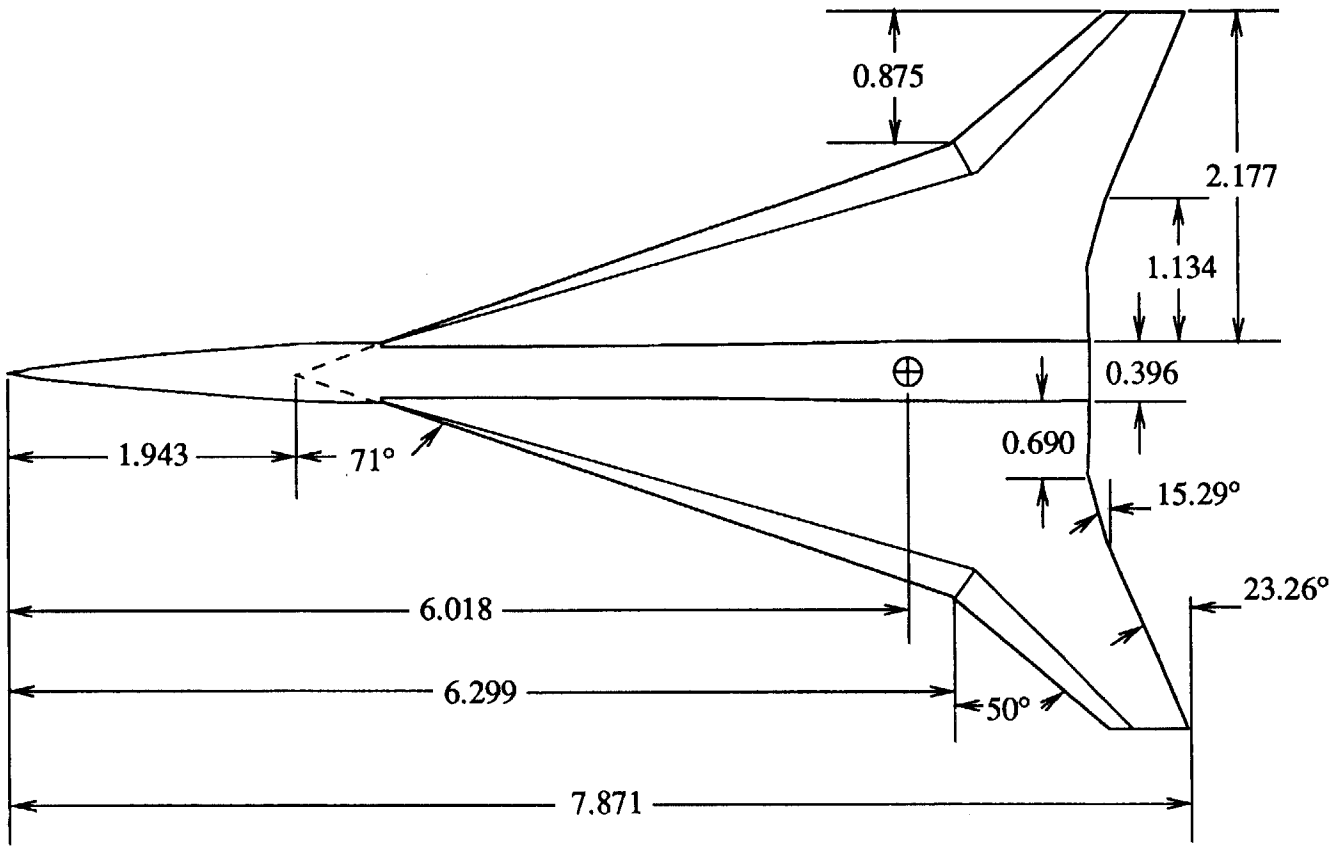

Figure 1. Planform view of the generic high speed transport configuration.
All linear dimensions are in feet.

MA Strip	X_{LE}-Loc., ft.	Y_{LE}-Loc., ft.
1	3.50	0.54
2	4.08	0.74
3	4.67	0.94
4	5.25	1.13
5	5.88	1.35

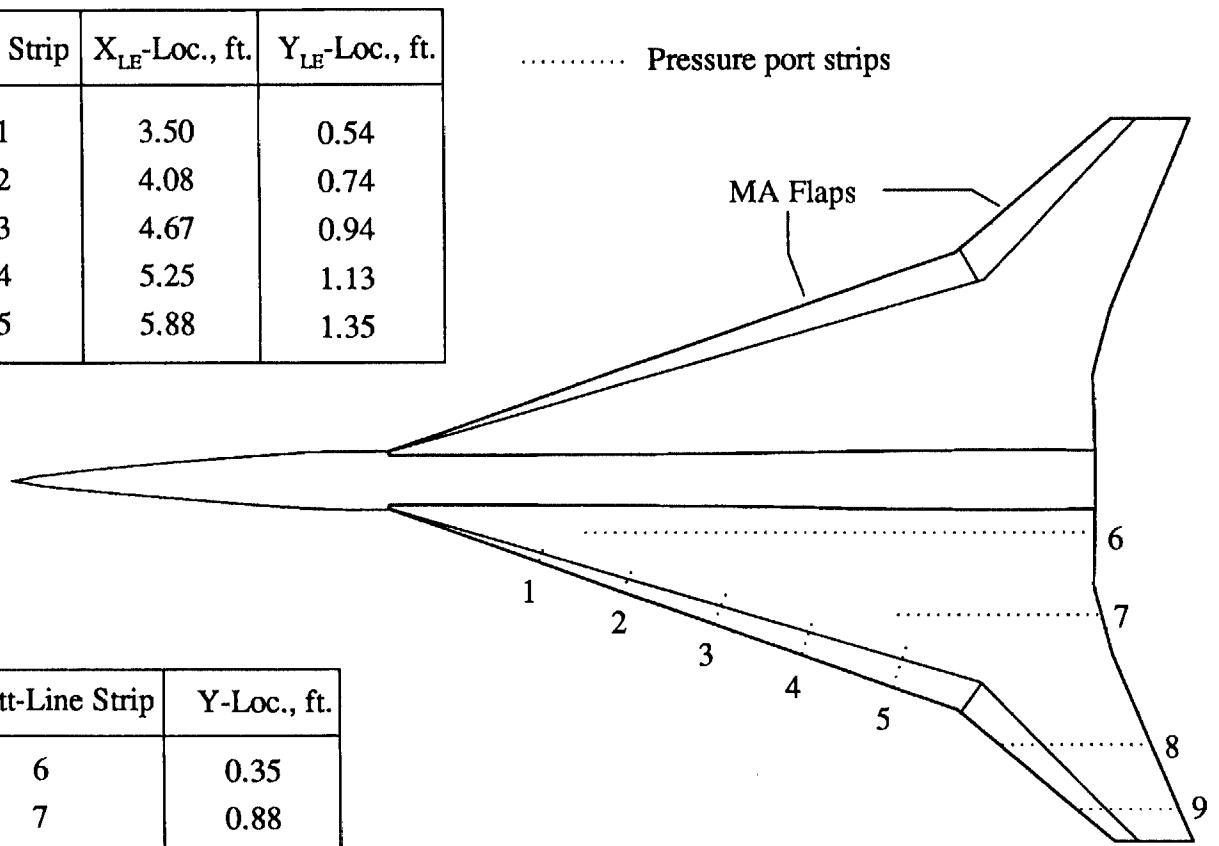

Butt-Line Strip	Y-Loc., ft.
6	0.35
7	0.88
8	1.73
9	2.17

Figure 2. Pressure port strip locations on the model.

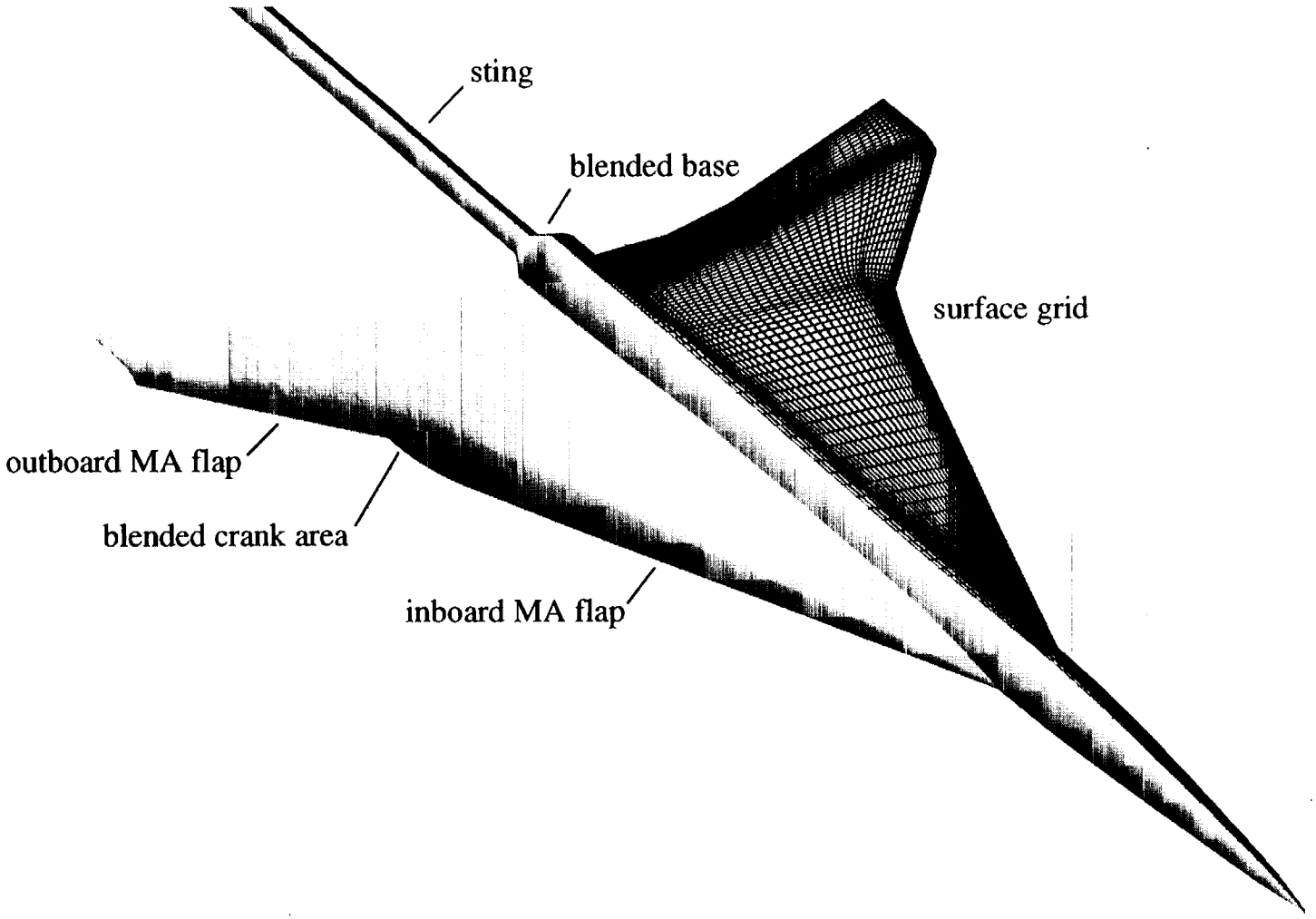

Figure 3. Perspective view of the surface and surface grid.

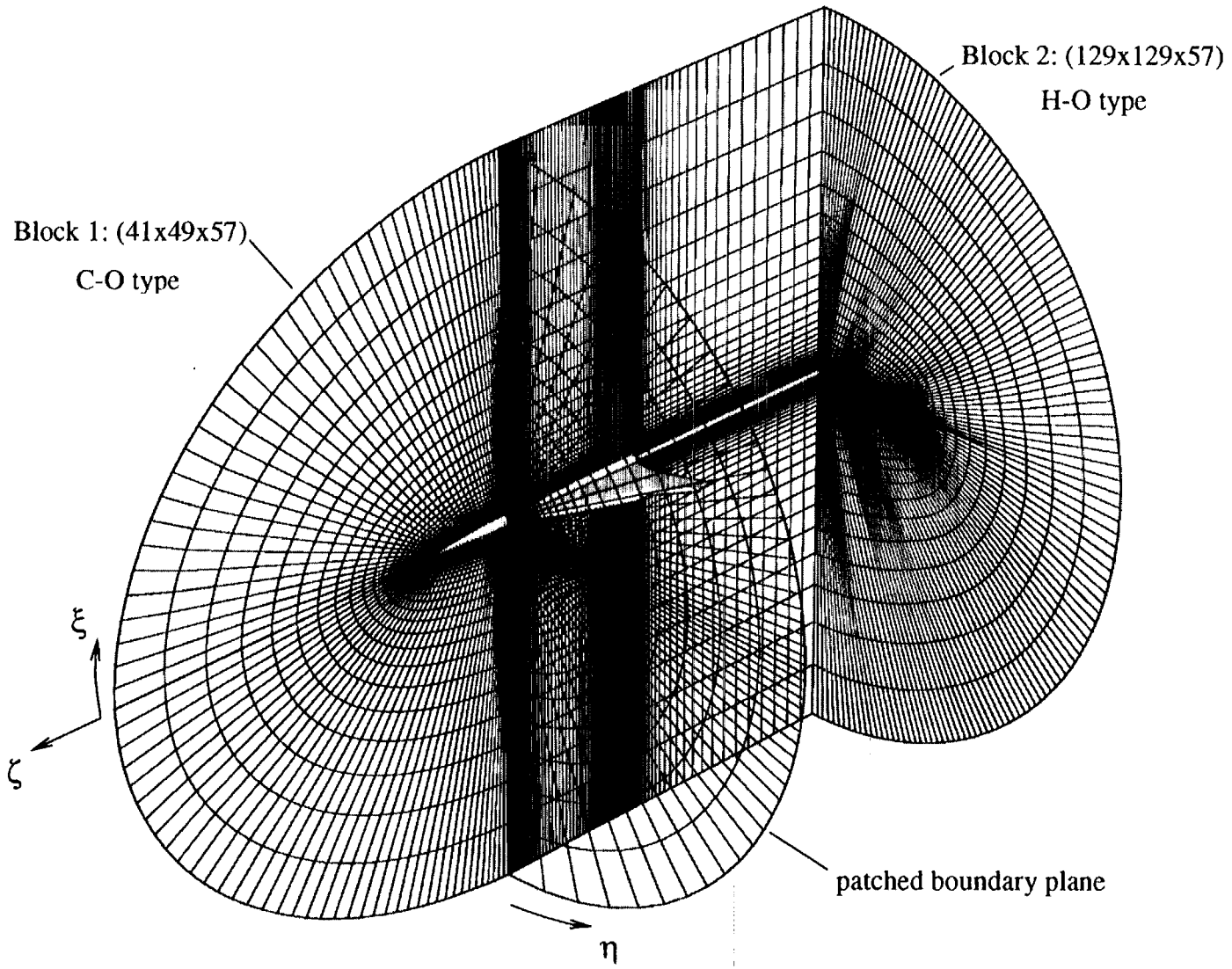

Figure 4. Perspective view of the multi-block volume grid.

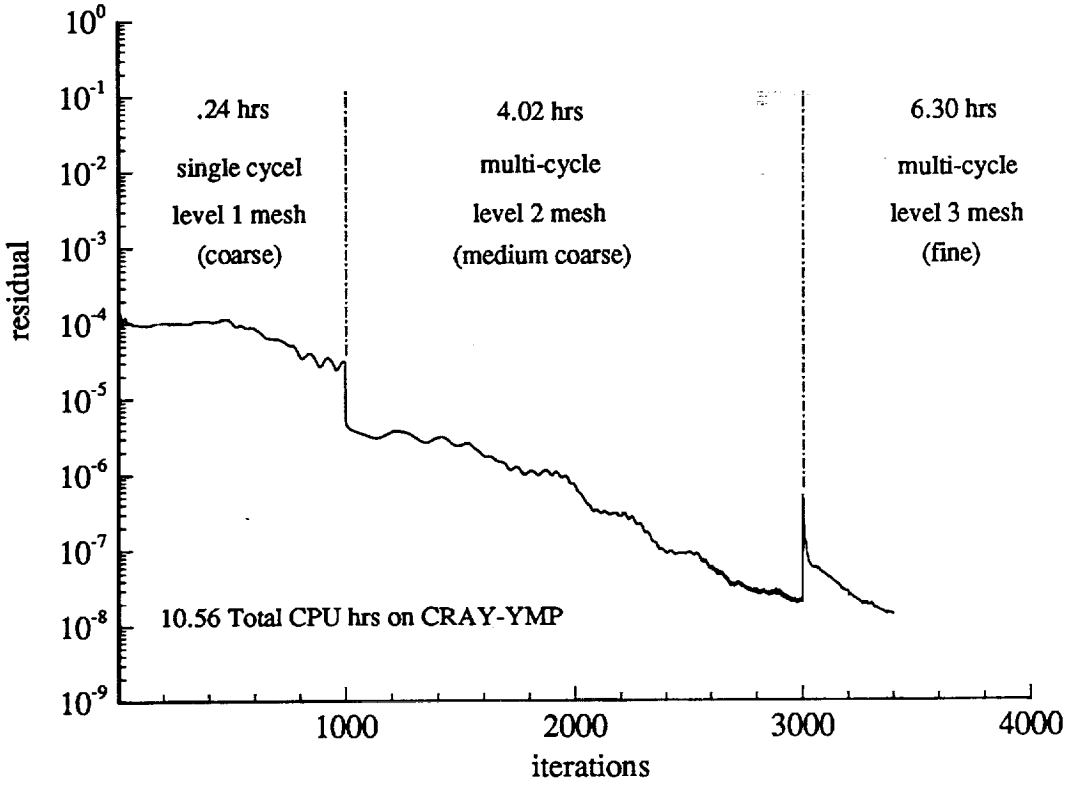

(a) Residual history

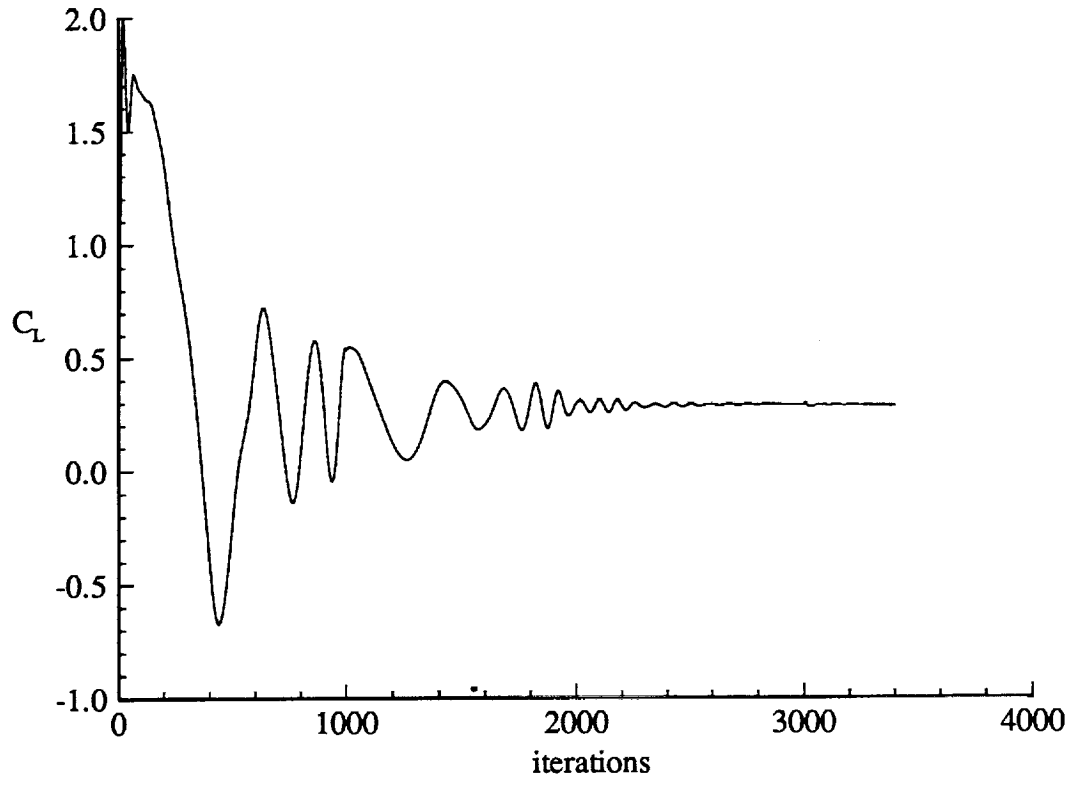

(b) Lift coefficient history

Figure 5. Convergence history for the Baldwin-Lomax turbulence solution at α=8°.

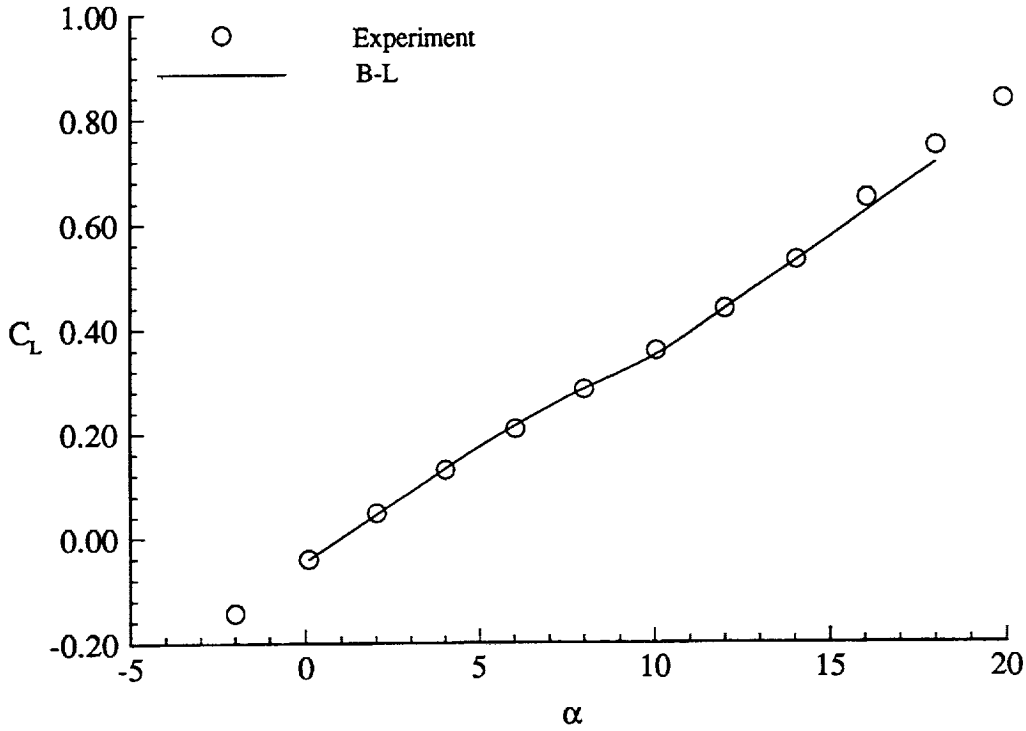

(a) Baseline Baldwin-Lomax turbulence model results.

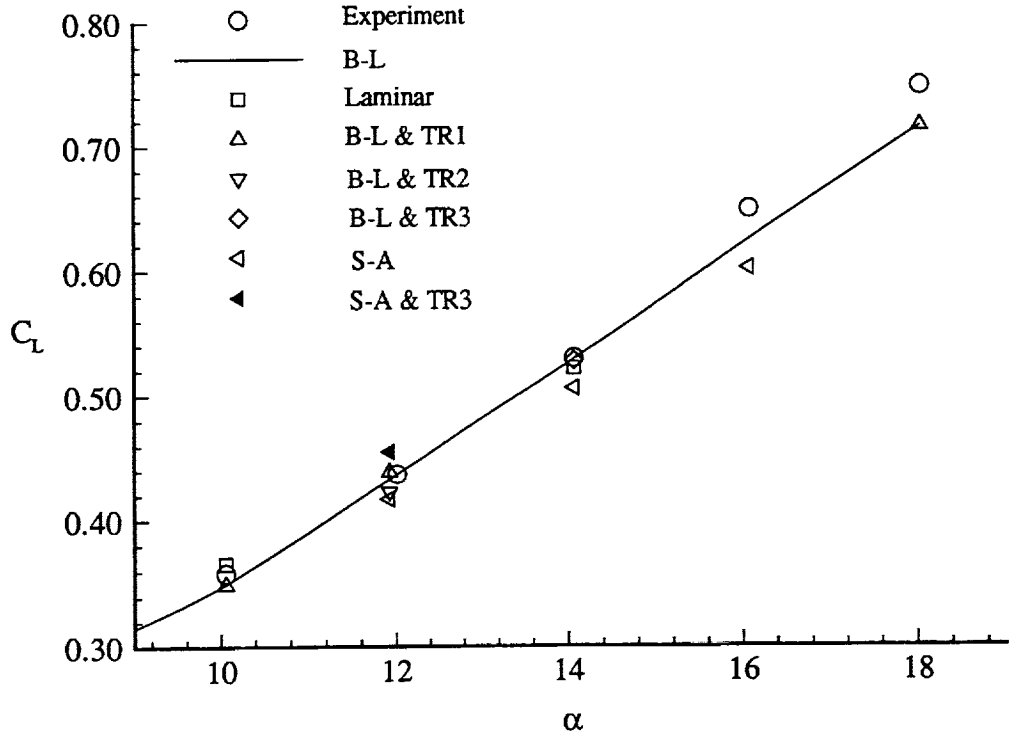

(b) Transition and turbulence models comparisons.

Figure 6. Experimental and predicted lift coefficent data.

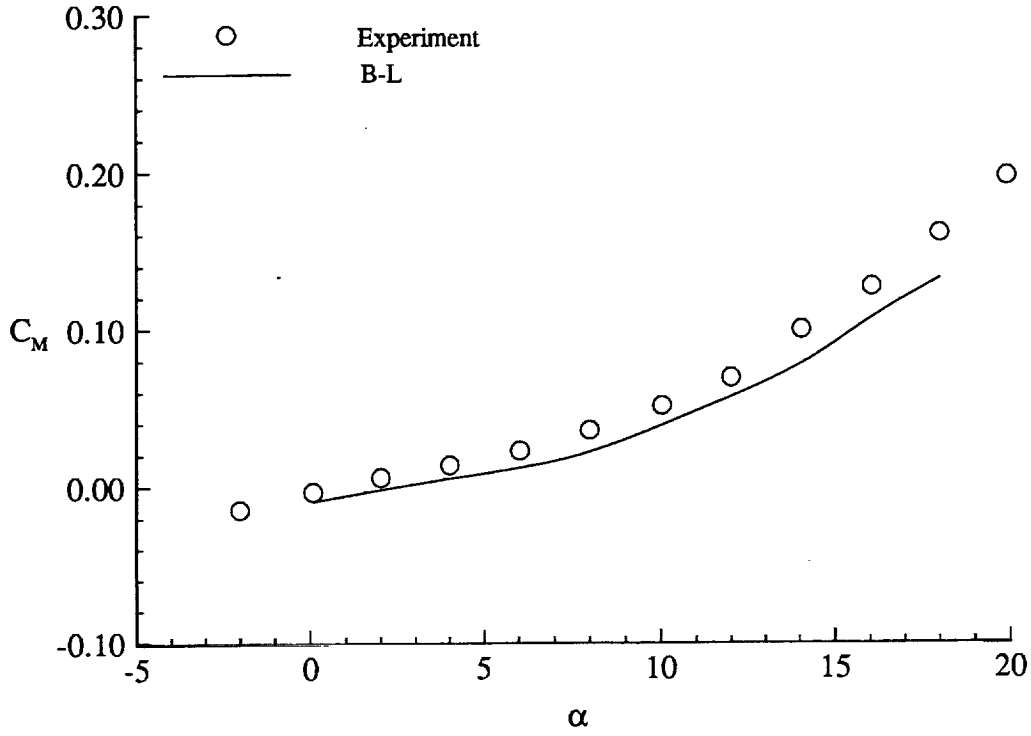

(a) Baseline Baldwin-Lomax turbulence model results.

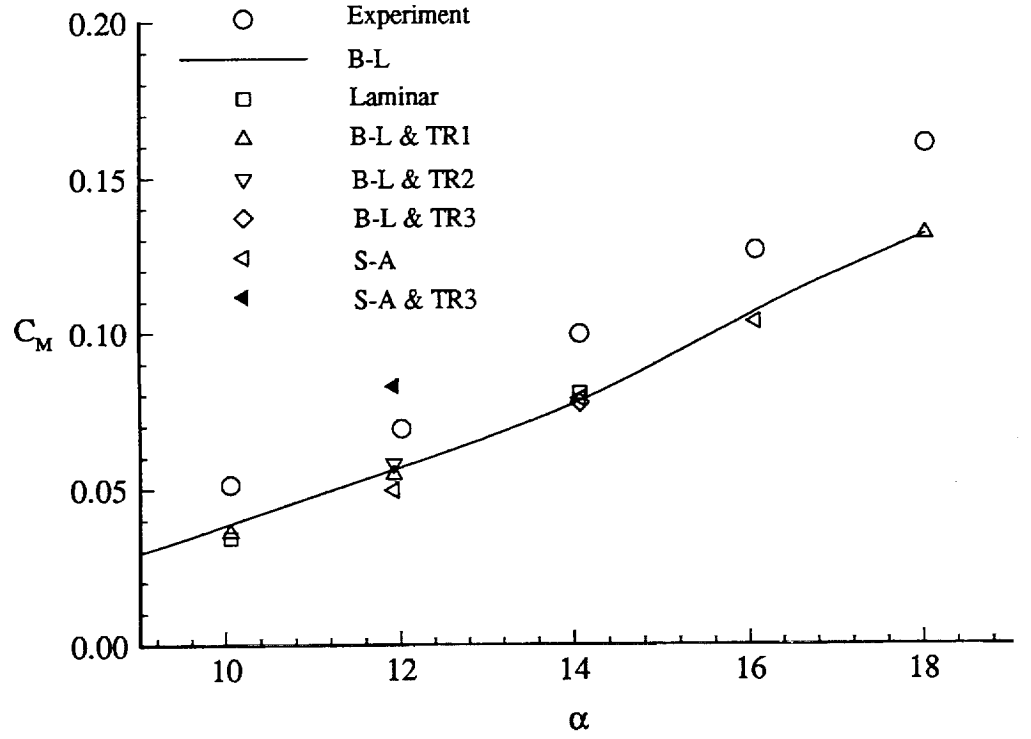

(b) Transition and turbulence models comparisons.

Figure 7. Predicted and experimental pitching moment coefficent data.

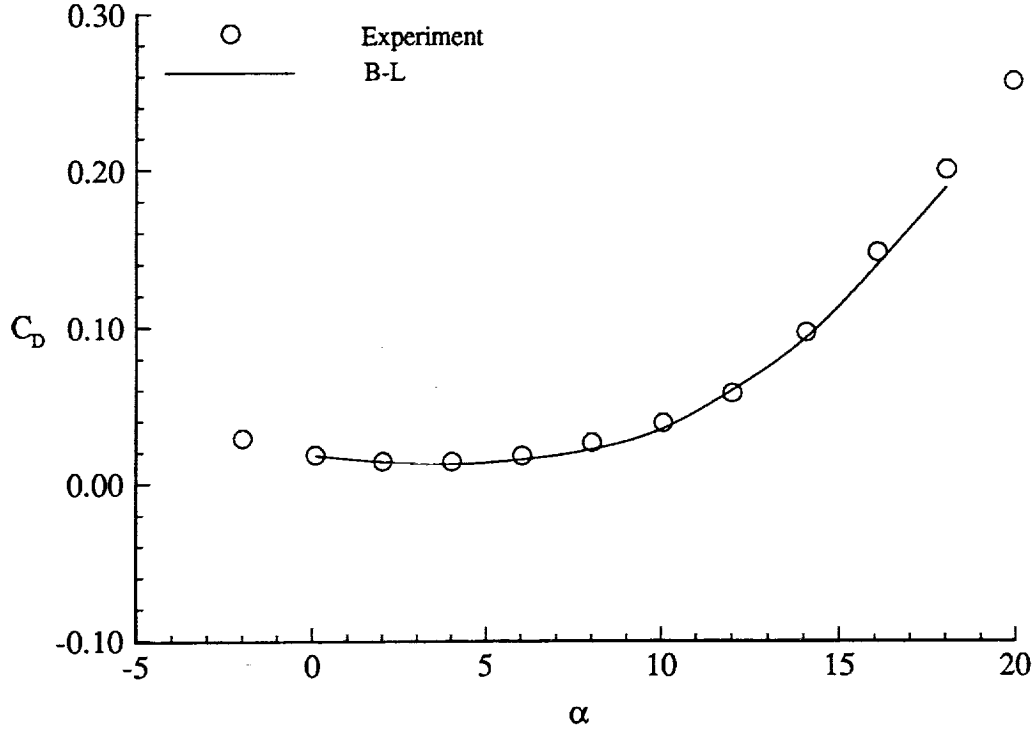

(a) Baseline Baldwin-Lomax turbulence model results.

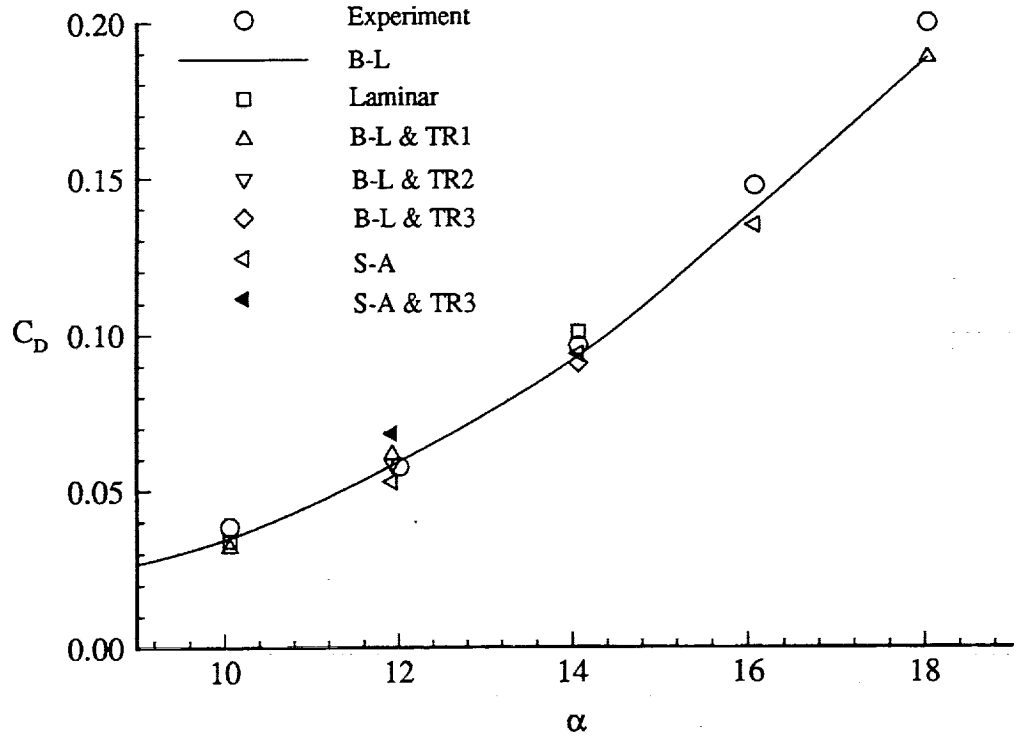

(b) Transition and turbulence models comparisons.

Figure 8. Predicted and experimental drag coefficent data.

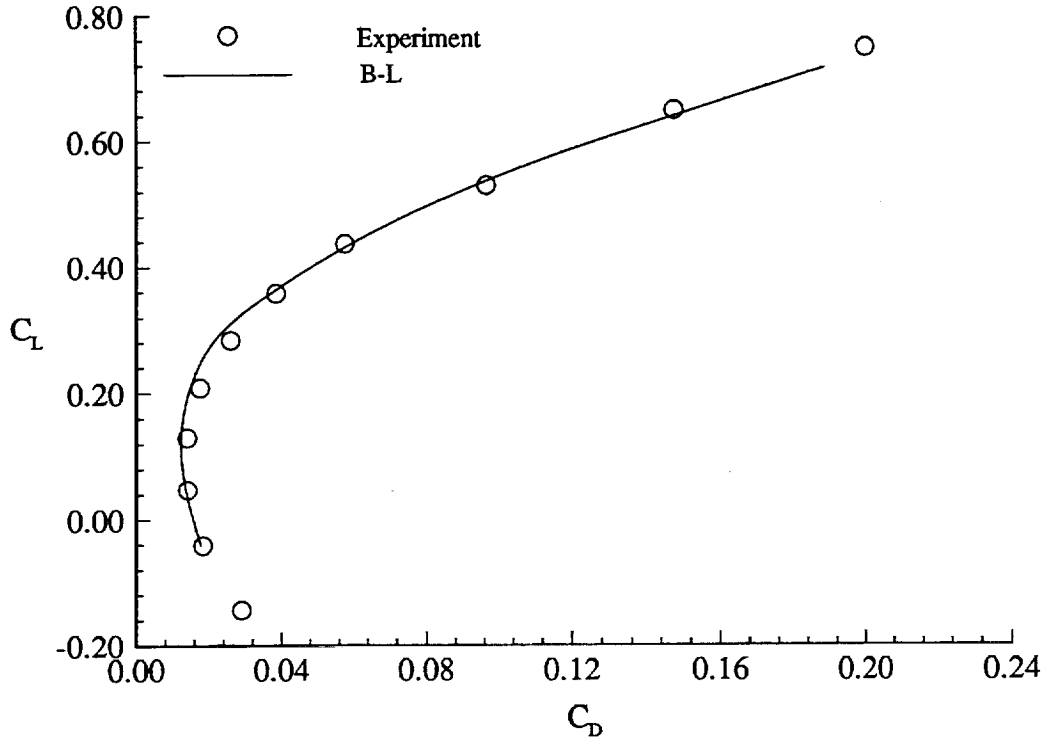

(a) Baseline Baldwin-Lomax turbulence model results.

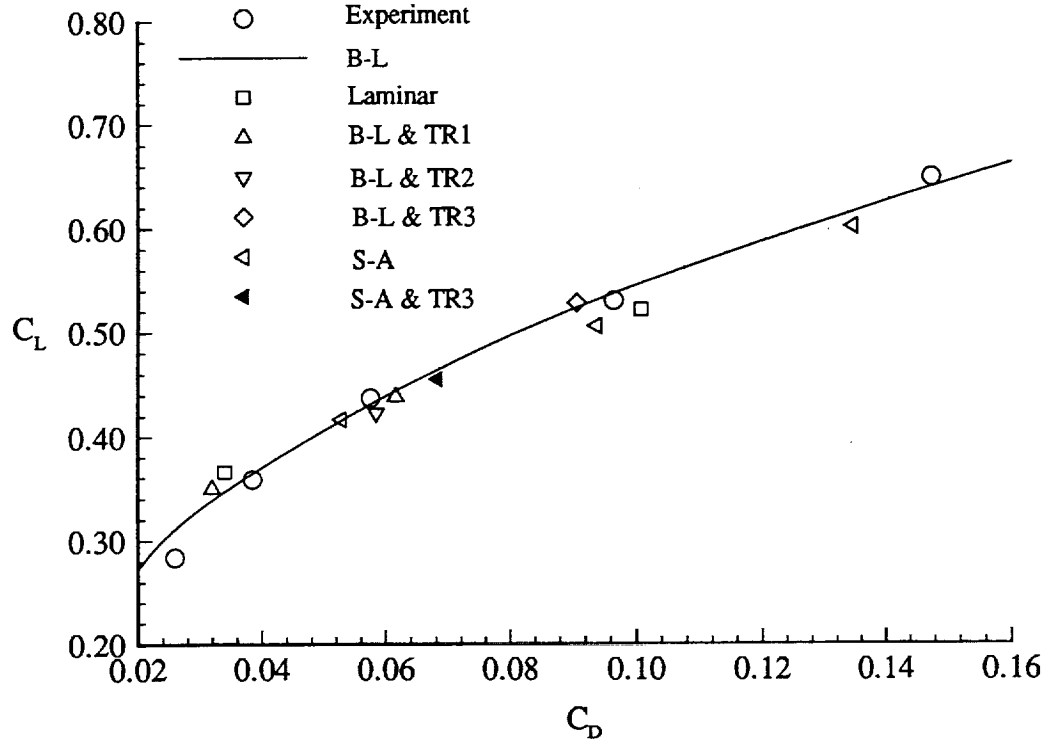

(b) Transition and turbulence models comparisons.

Figure 9. Predicted and experimental drag polar data.

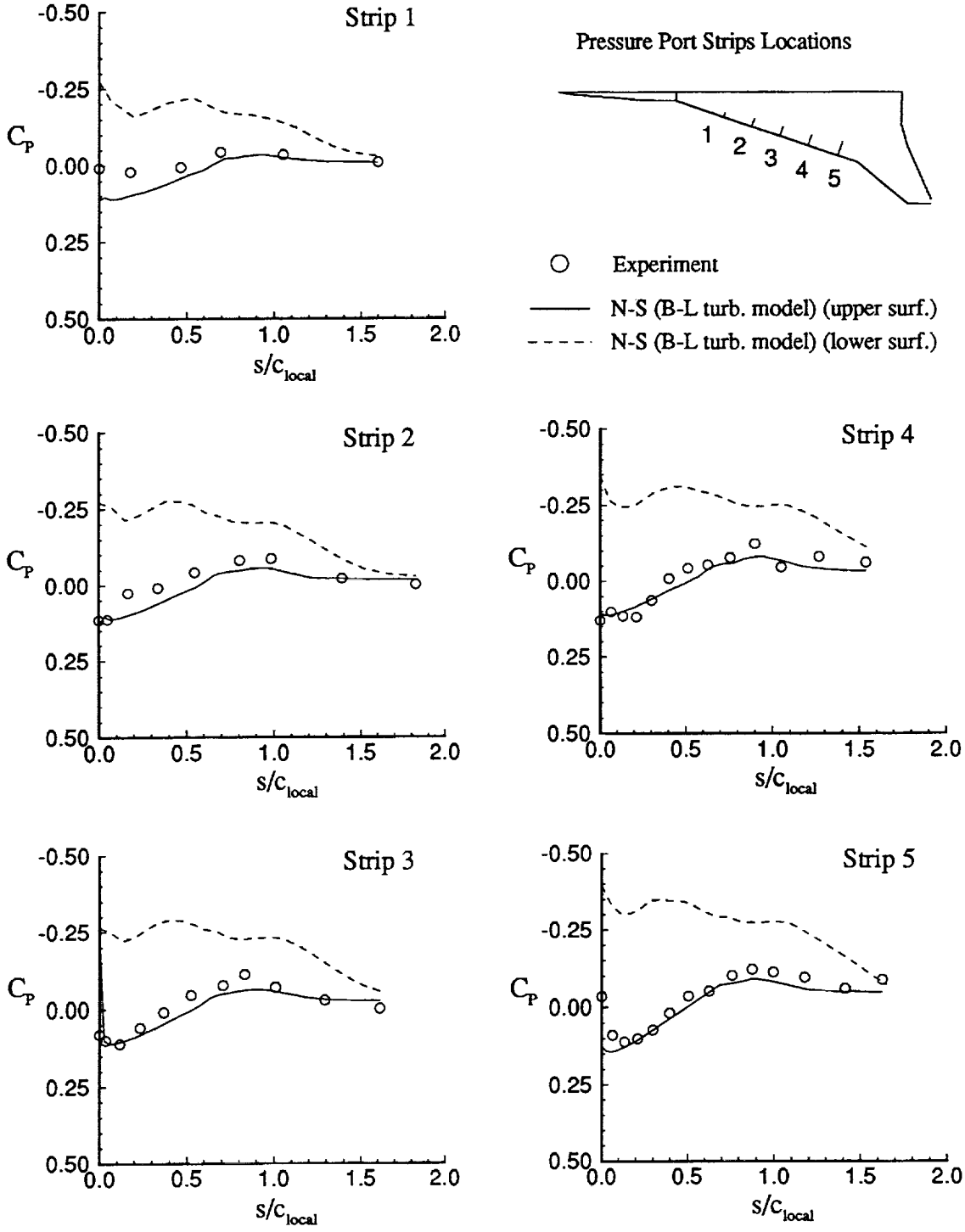

(a) Pressures on the inboard MA flap.

Figure 10. Comparisons of predicted and experimental pressure coefficents for the flow conditions of M=0.22, Re_L=1.39x10^6/ft. and α=0.0°.

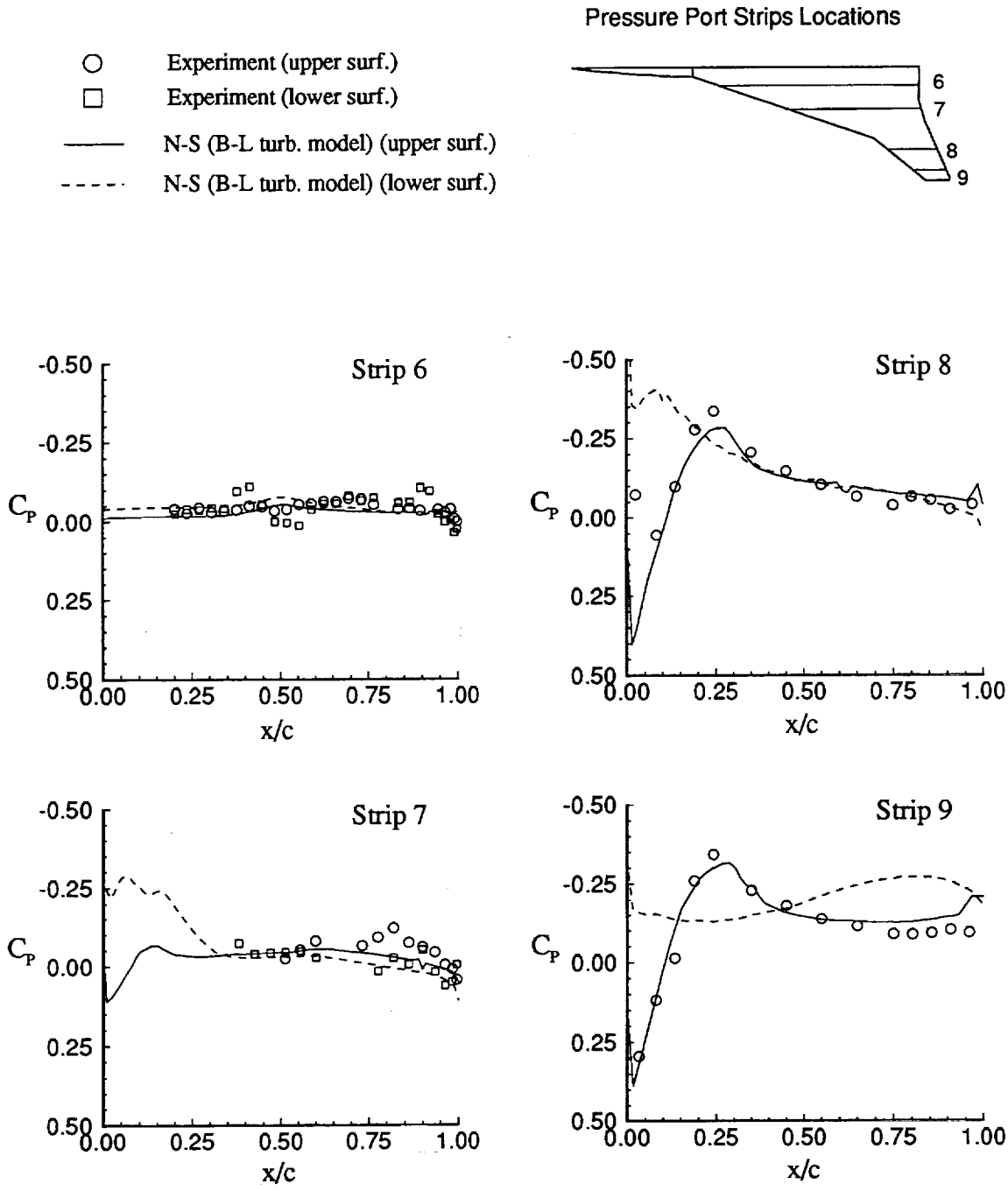

(b) Butt-line pressures on the inboard and outboard wing sections.

Figure 10. Concluded.

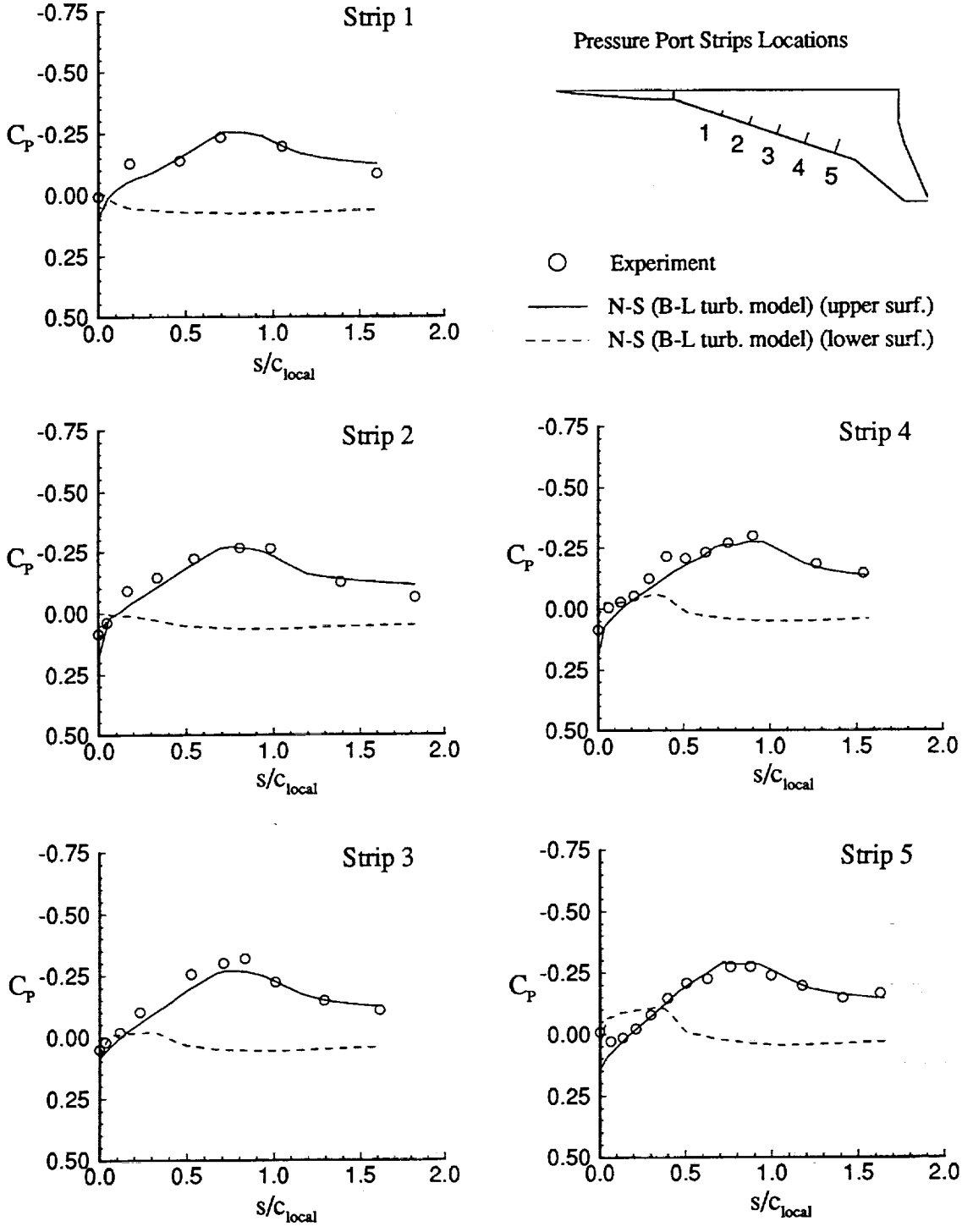

(a) Pressures on the inboard MA flap.

Figure 11. Comparisons of predicted and experimental pressure coefficents for the flow conditions of M=0.22, Re_L=1.39x10^6/ft. and α=4.0°.

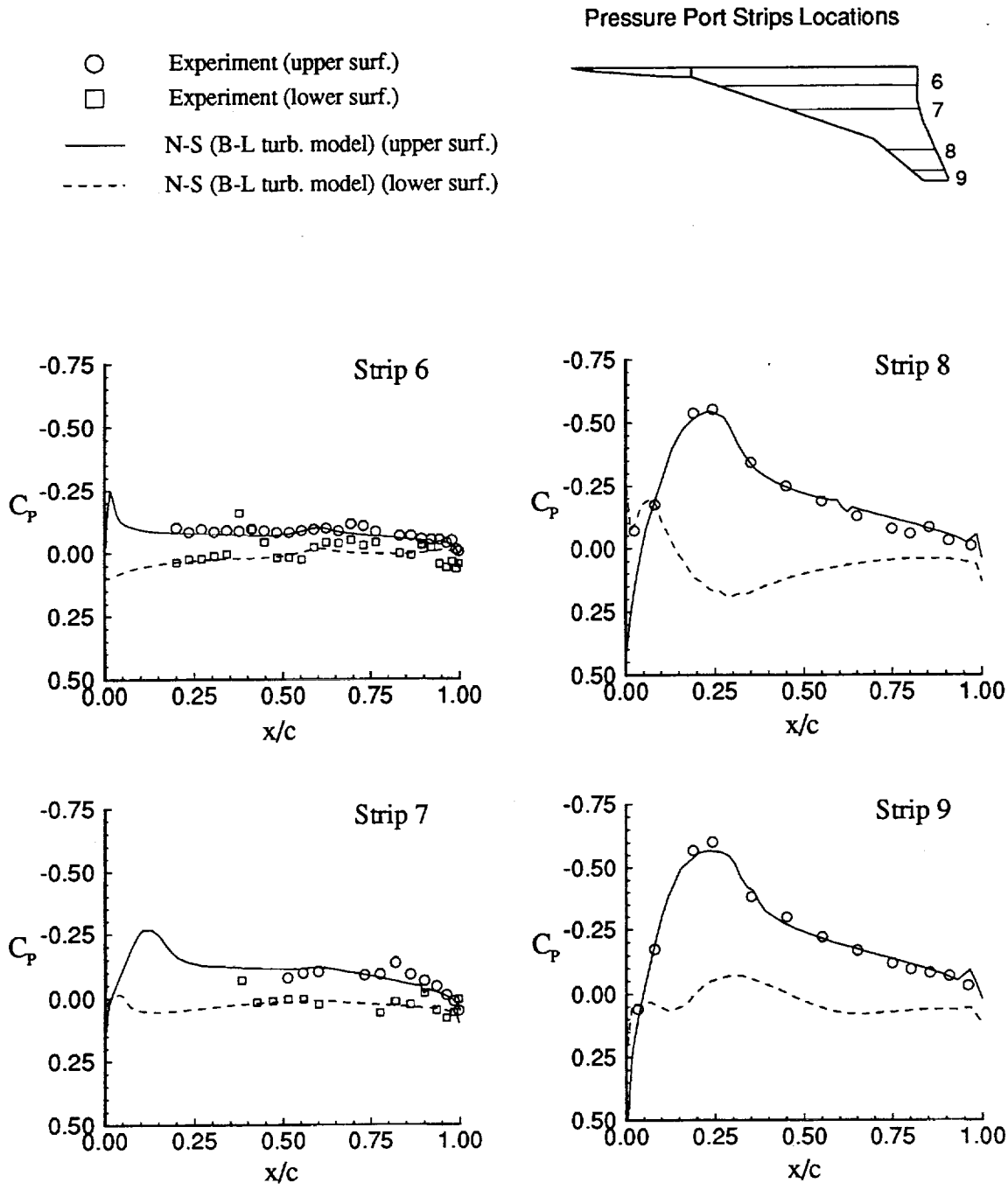

(b) Butt-line pressures on the inboard and outboard wing sections.

Figure 11. Concluded.

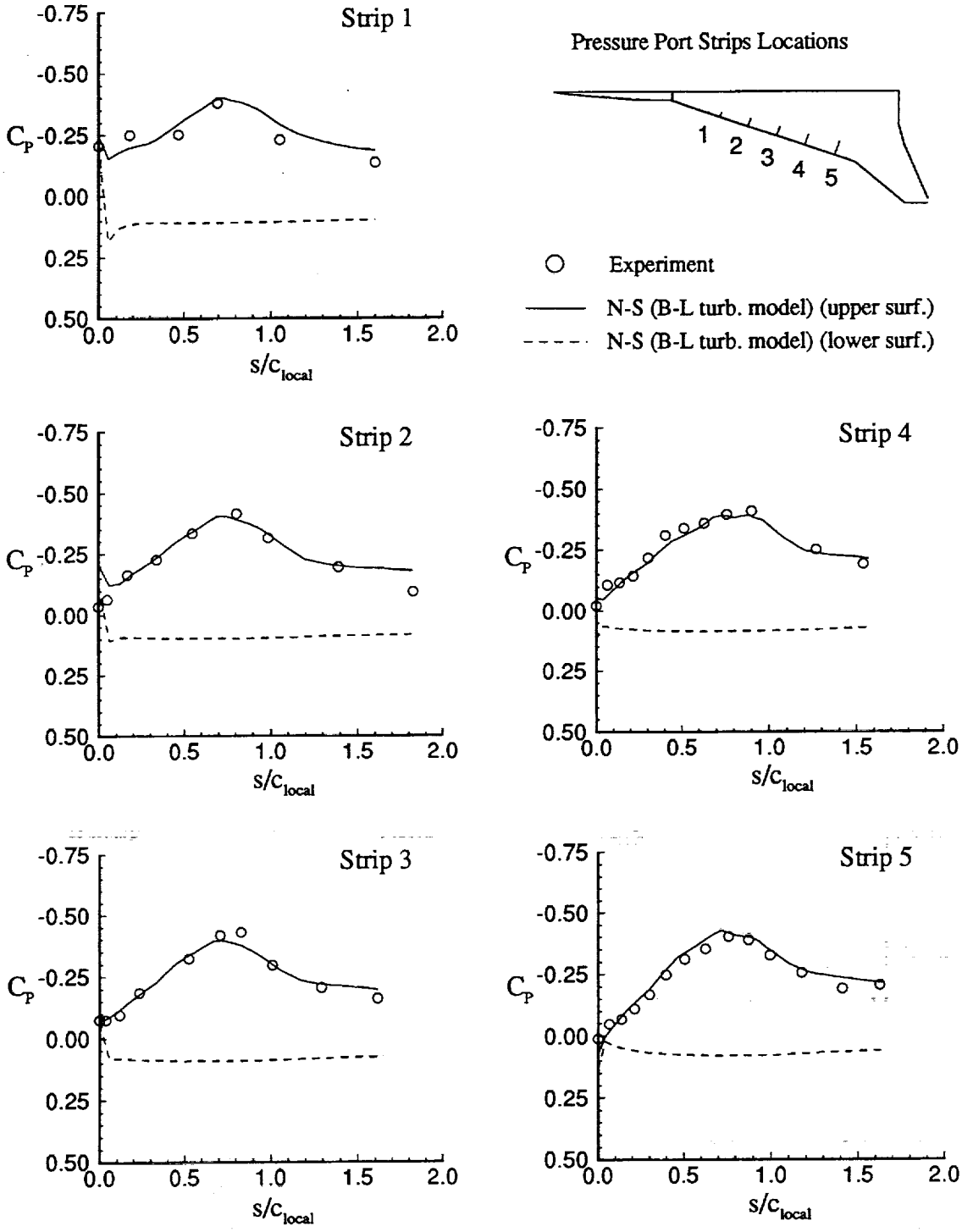

(a) Pressures on the inboard MA flap.

Figure 12. Comparisons of predicted and experimental pressure coefficents for the flow conditions of M=0.22, Re_L=1.39x10^6/ft. and α=6.0°.

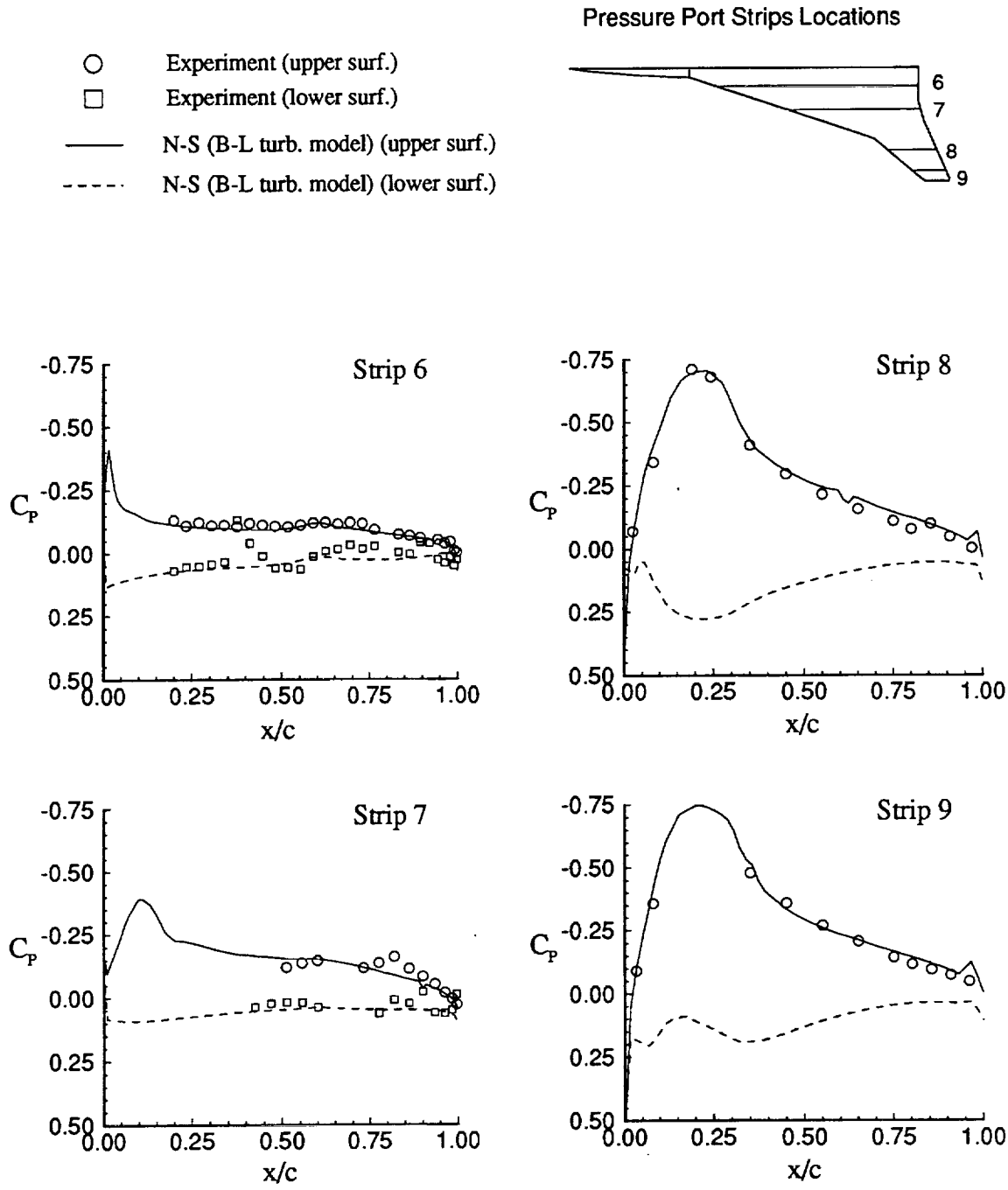

(b) Butt-line pressures on the inboard and outboard wing sections.

Figure 12. Concluded.

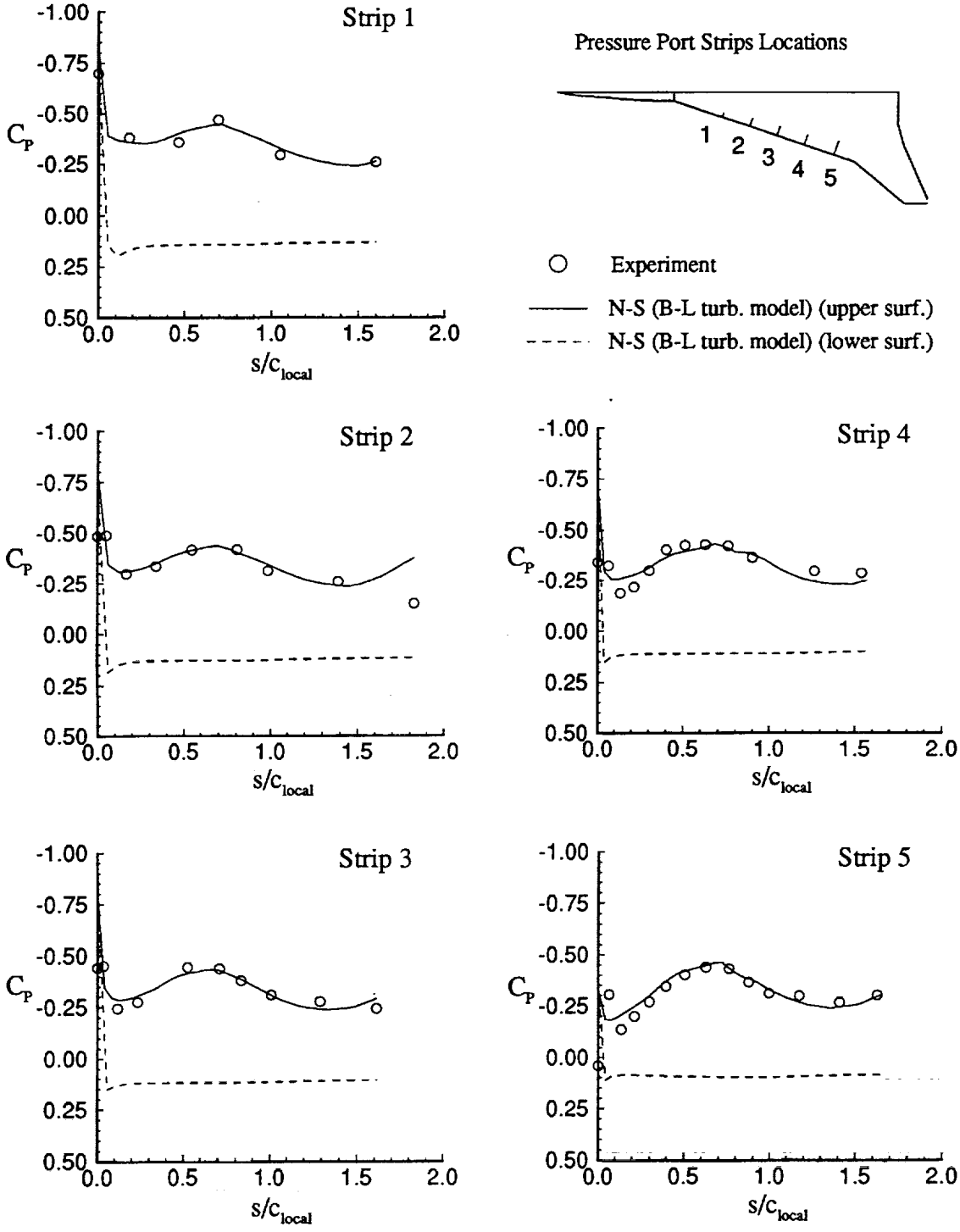

(a) Pressures on the inboard MA flap.

Figure 13. Comparisons of predicted and experimental pressure coefficents for the flow conditions of M=0.22, Re_L=1.39x10^6/ft. and α=8.0°.

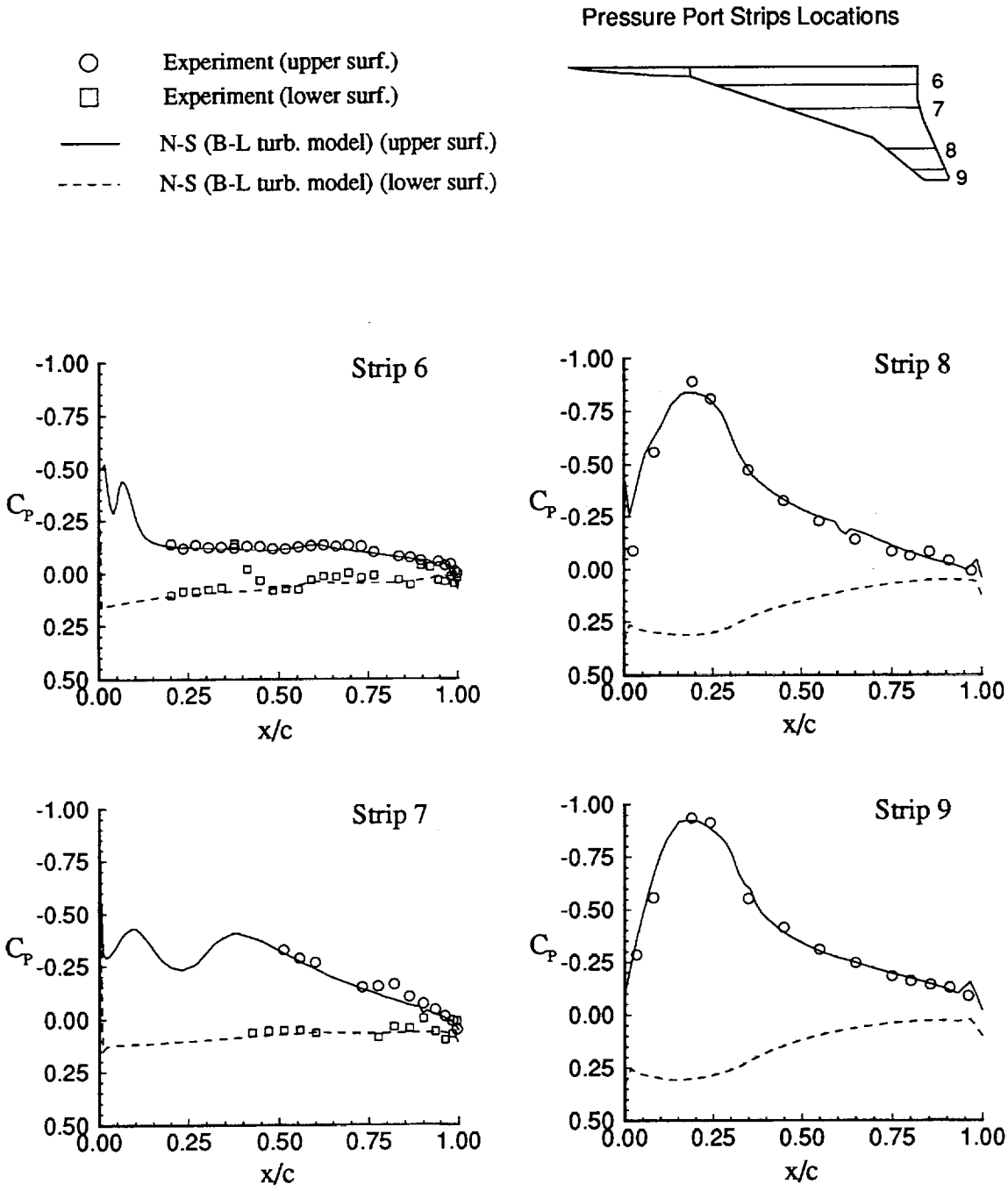

(b) Butt-line pressures on the inboard and outboard wing sections.

Figure 13. Concluded.

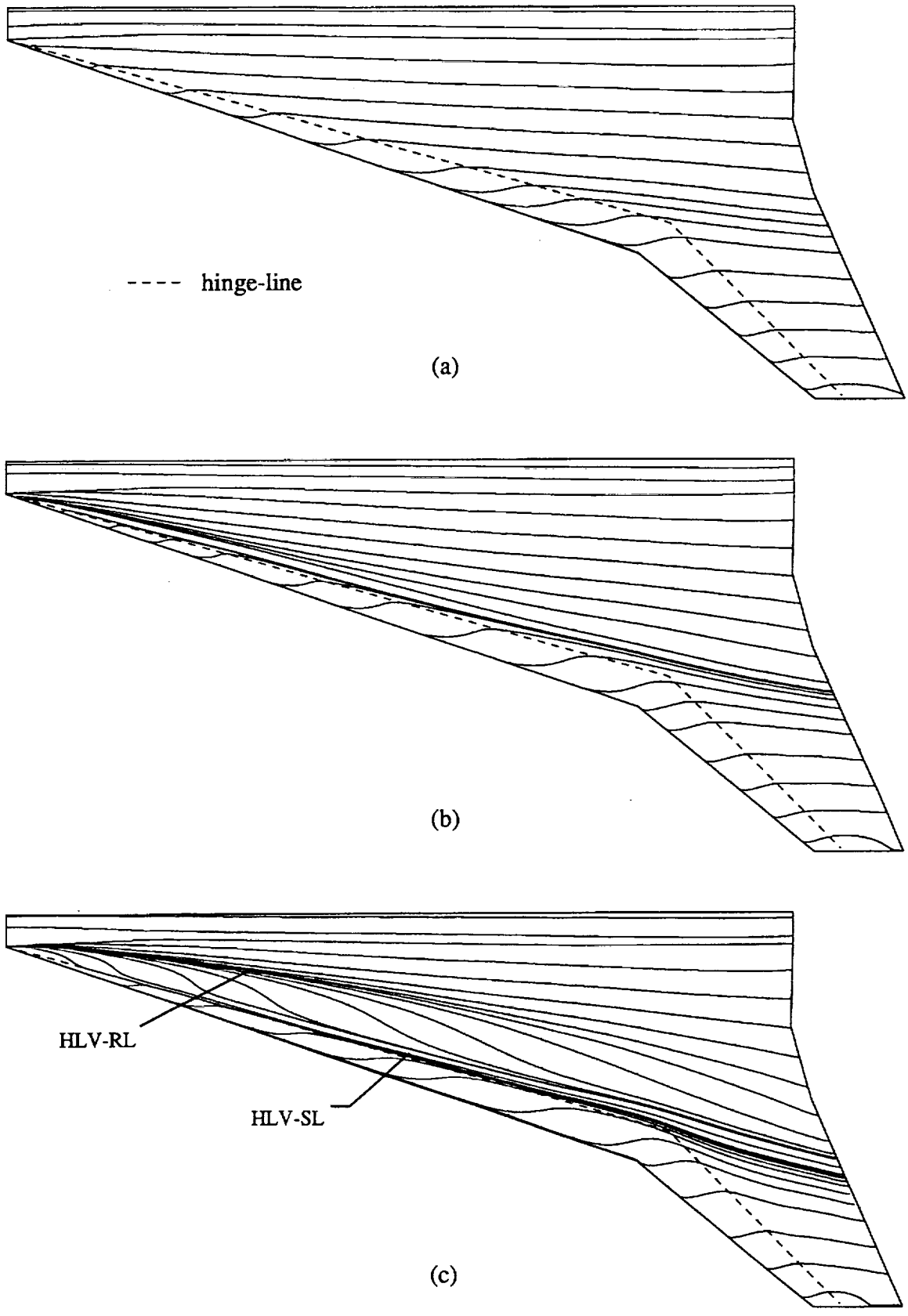

Figure 14. Computed upper surface limiting streamlines for (a) α=4.0°, (b) α=6.0°, (c) α=8.0°. Results are obtained using the Baldwin-Lomax turbulence model.

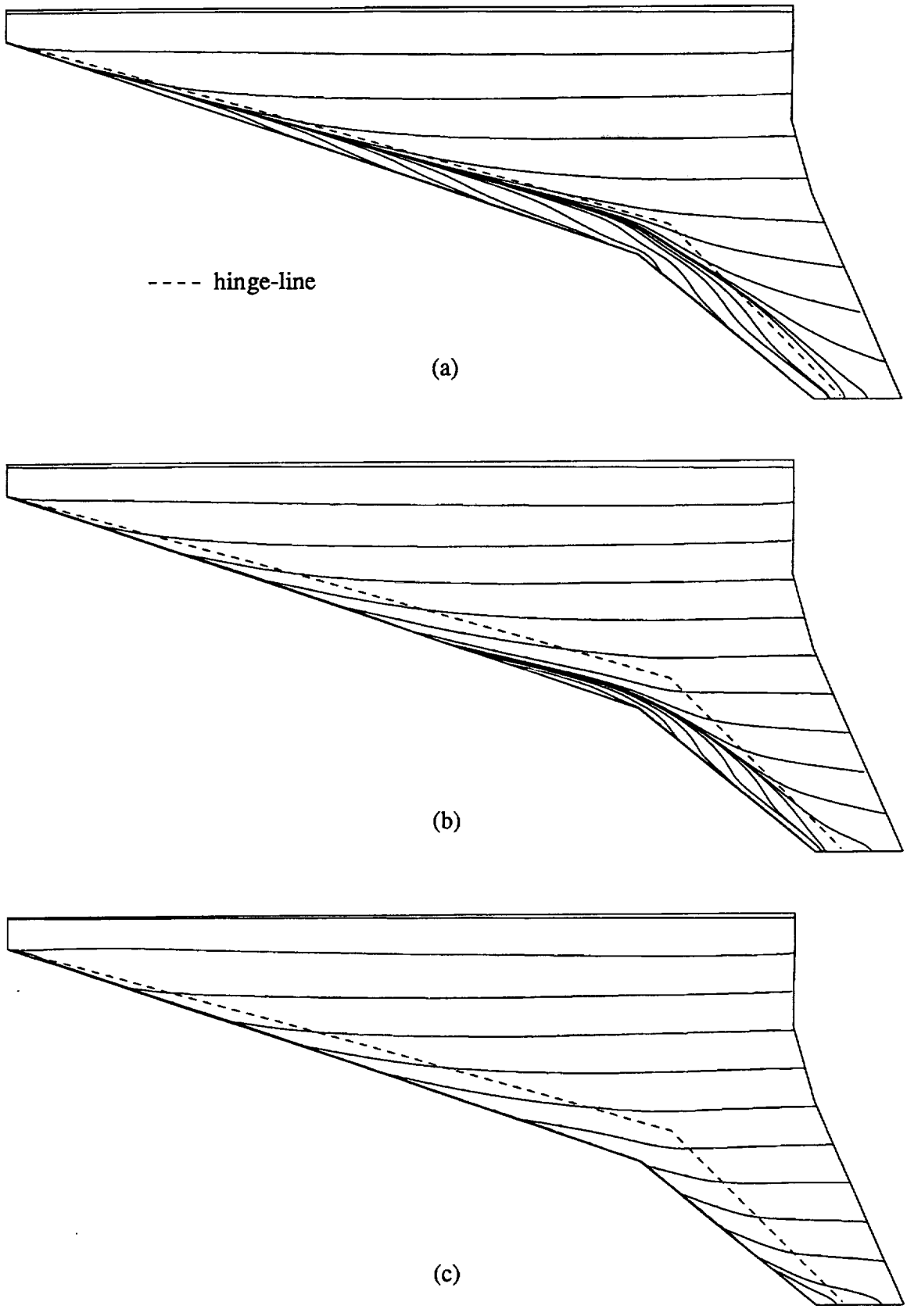

Figure 15. Computed lower surface limiting streamlines for (a) α=4.0°, (b) α=6.0°, (c) α=8.0°. Results are obtained using the Baldwin-Lomax turbulence model.

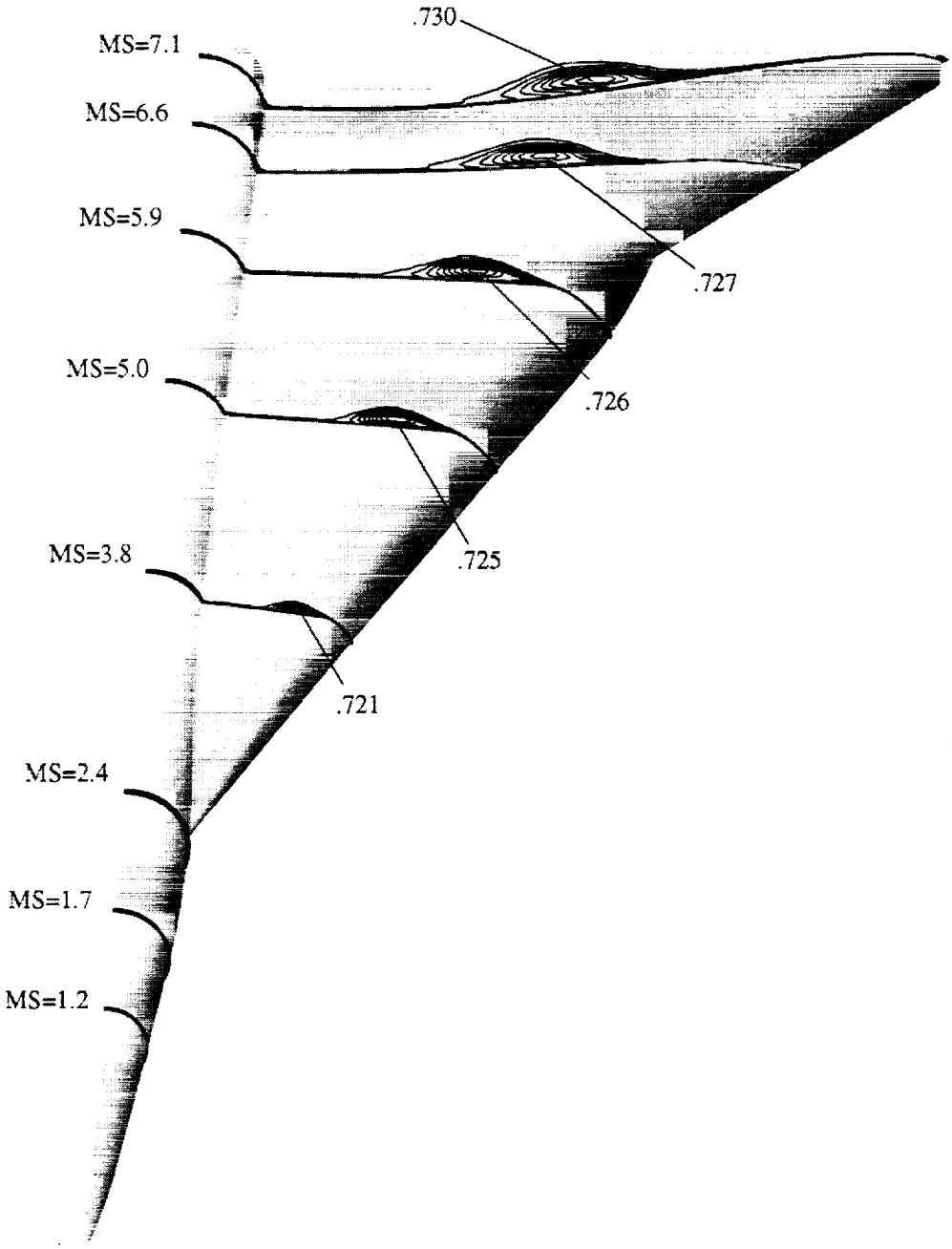

Figure 16. Predicted off-body normalized total pressure contours for α=8.0°. Solution obtained with Baldwin-Lomax turbulence model.

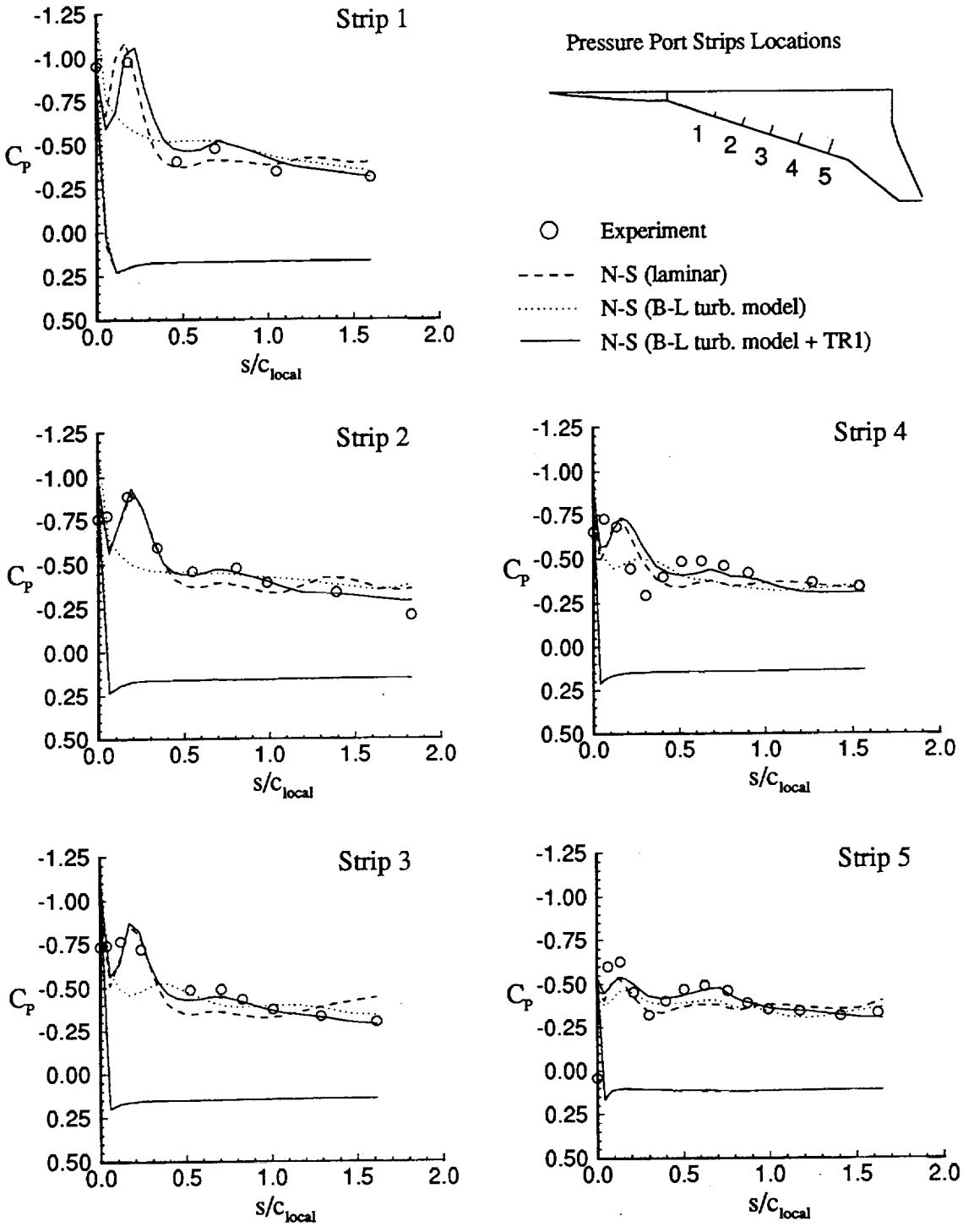

(a) Pressures on the inboard MA flap.

Figure 17. Comparisons of predicted and experimental pressure coefficents for the flow conditions of M=0.22, Re_L=1.39x10^6/ft. and α=10.1°.

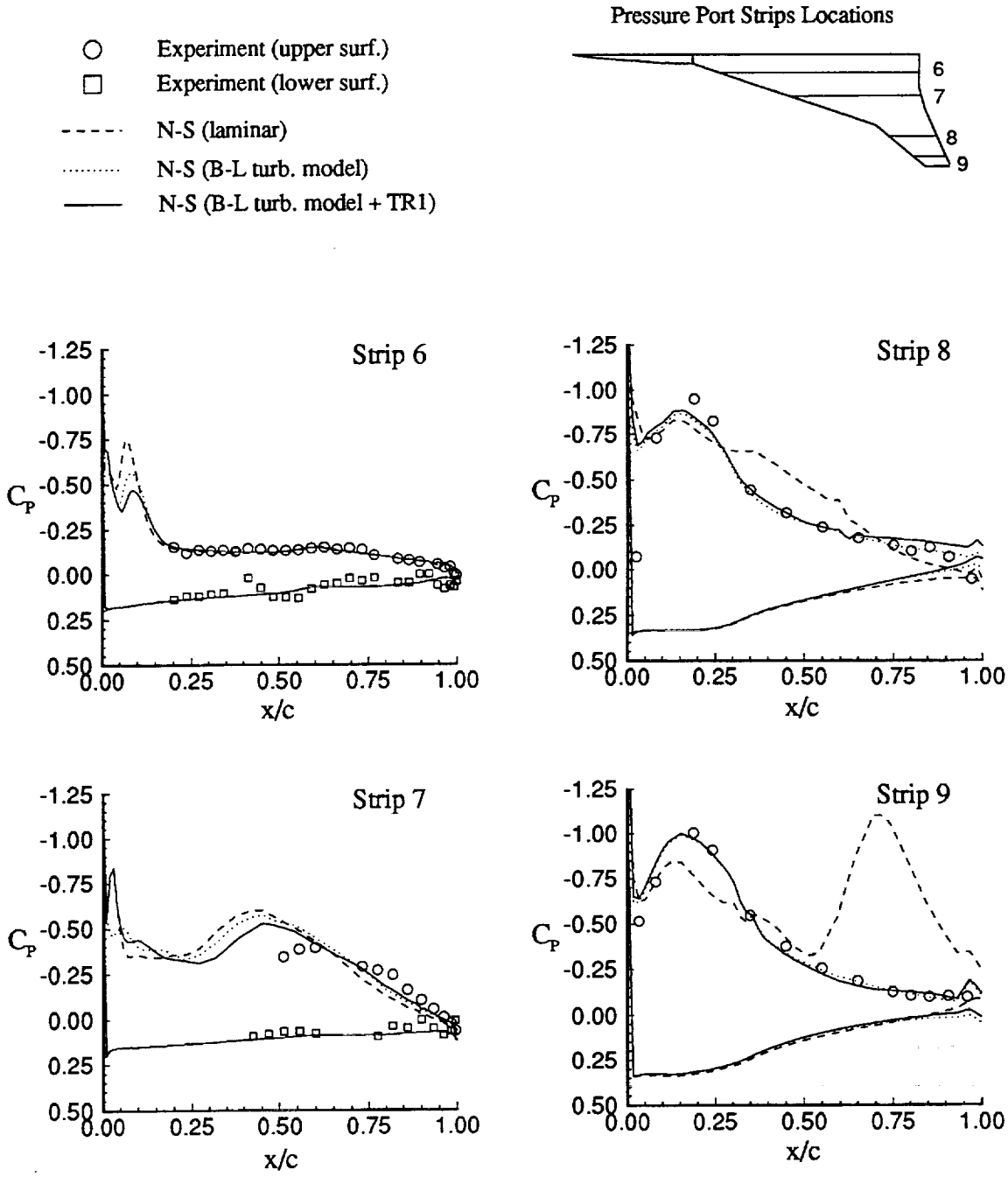

(b) Butt-line pressures on the inboard and outboard wing sections.

Figure 17. Concluded.

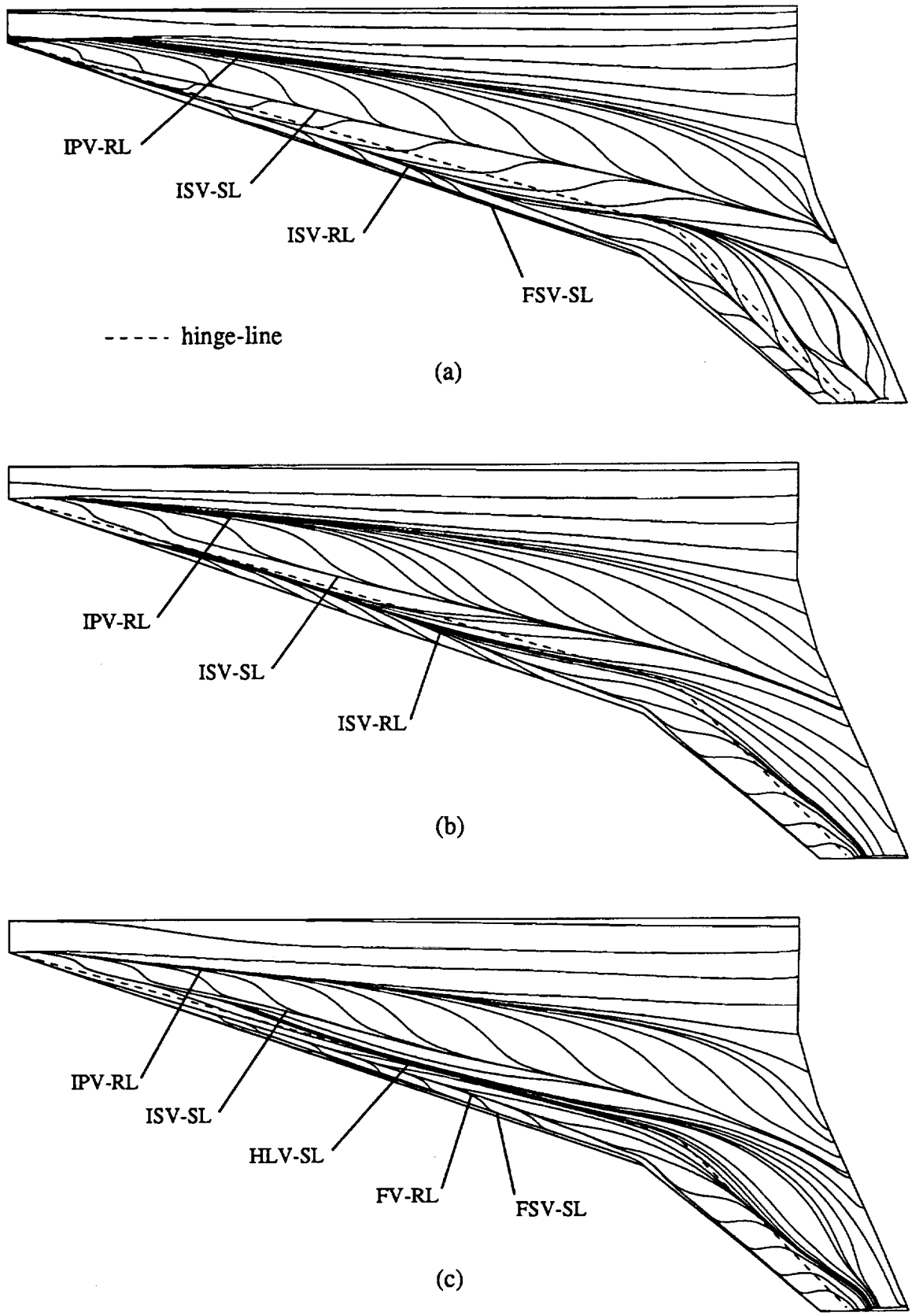

Figure 18. Computed upper surface limiting streamlines for α=10.1° with varying usage of Baldwin-Lomax turbulence model: (a) entirely laminar, (b) entirely turbulent, (c) transition case TR1.

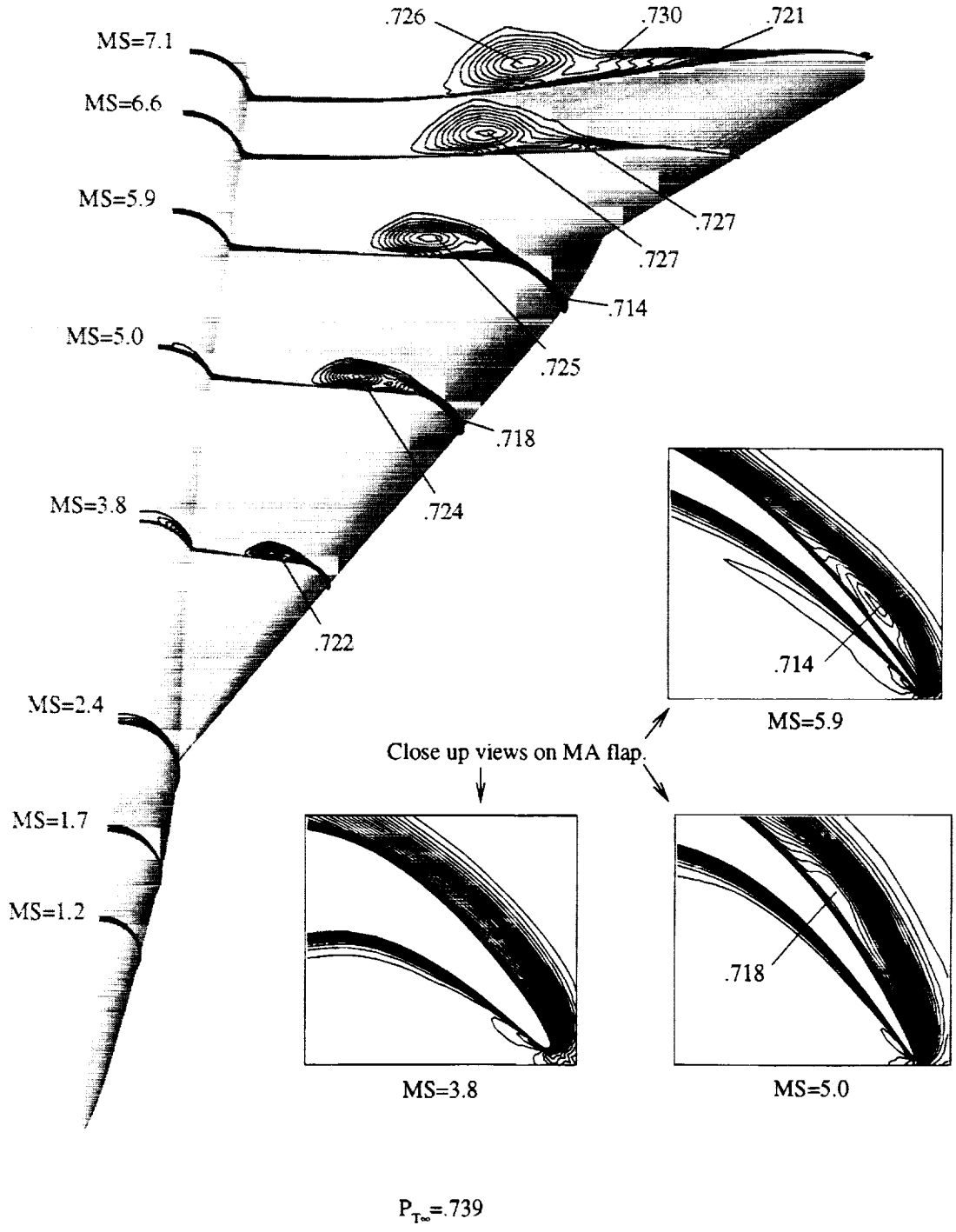

Figure 19. Predicted off-body normalized total pressure contours for α=10.1°. Solution obtained with Baldwin-Lomax turbulence model.

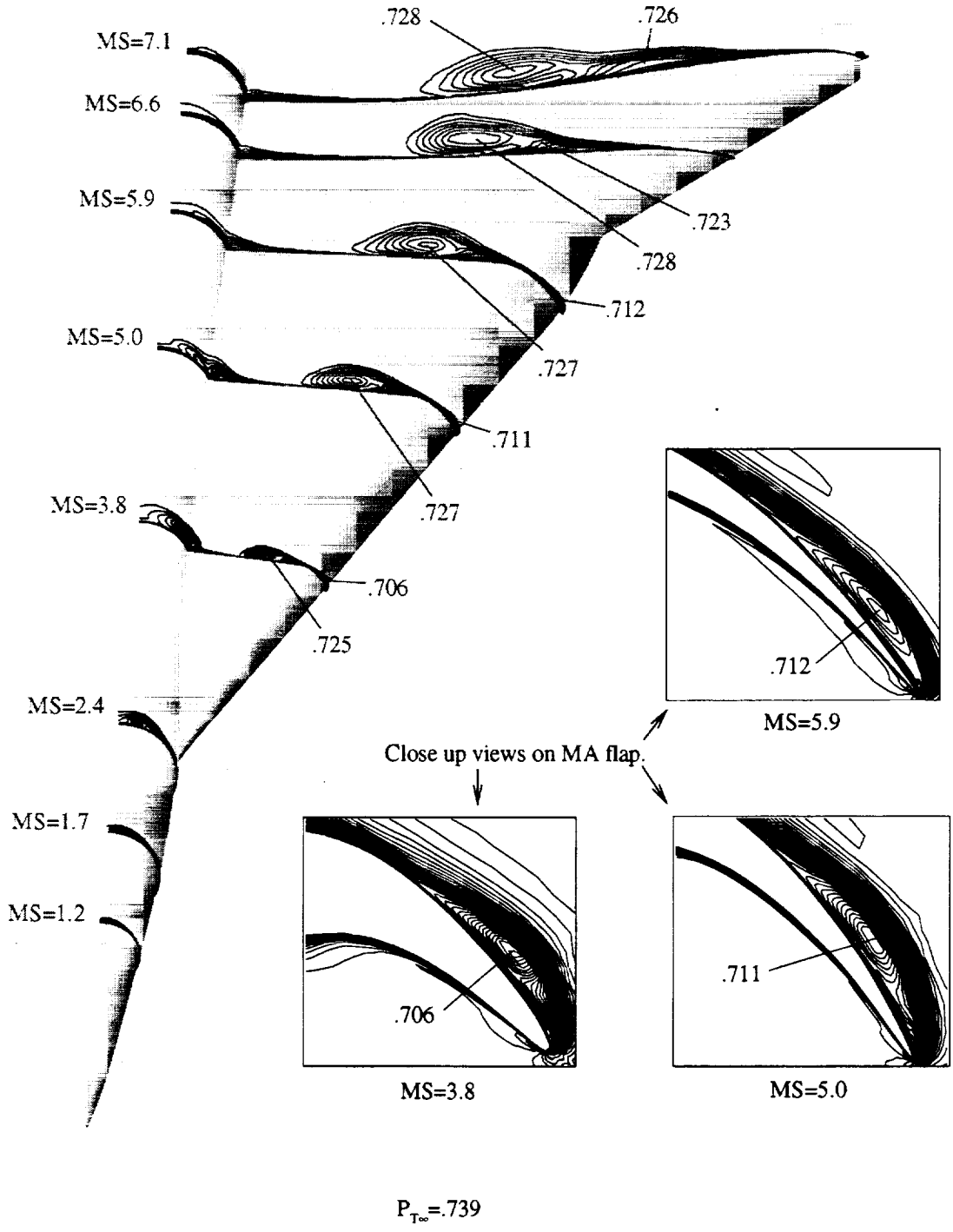

Figure 20. Predicted off-body normalized total pressure contours for α=10.1°. Solution obtained with Baldwin-Lomax turbulence model plus transition method TR1.

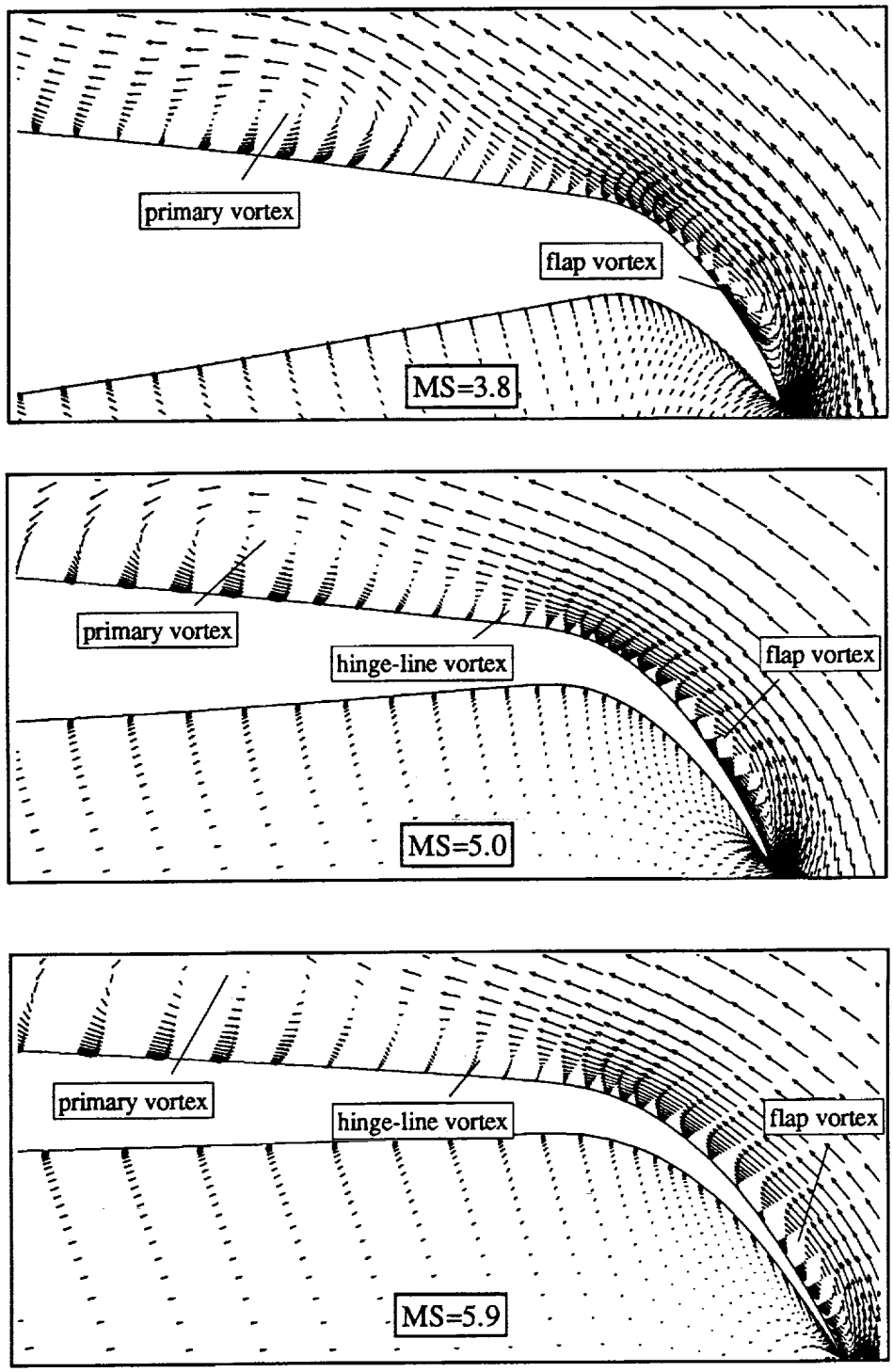

Figure 21. Cross-flow velocity vectors on the MA Flap at three model stations for α=10.1°. Solution obtained with Baldwin-Lomax turbulence model plus transition TR1.

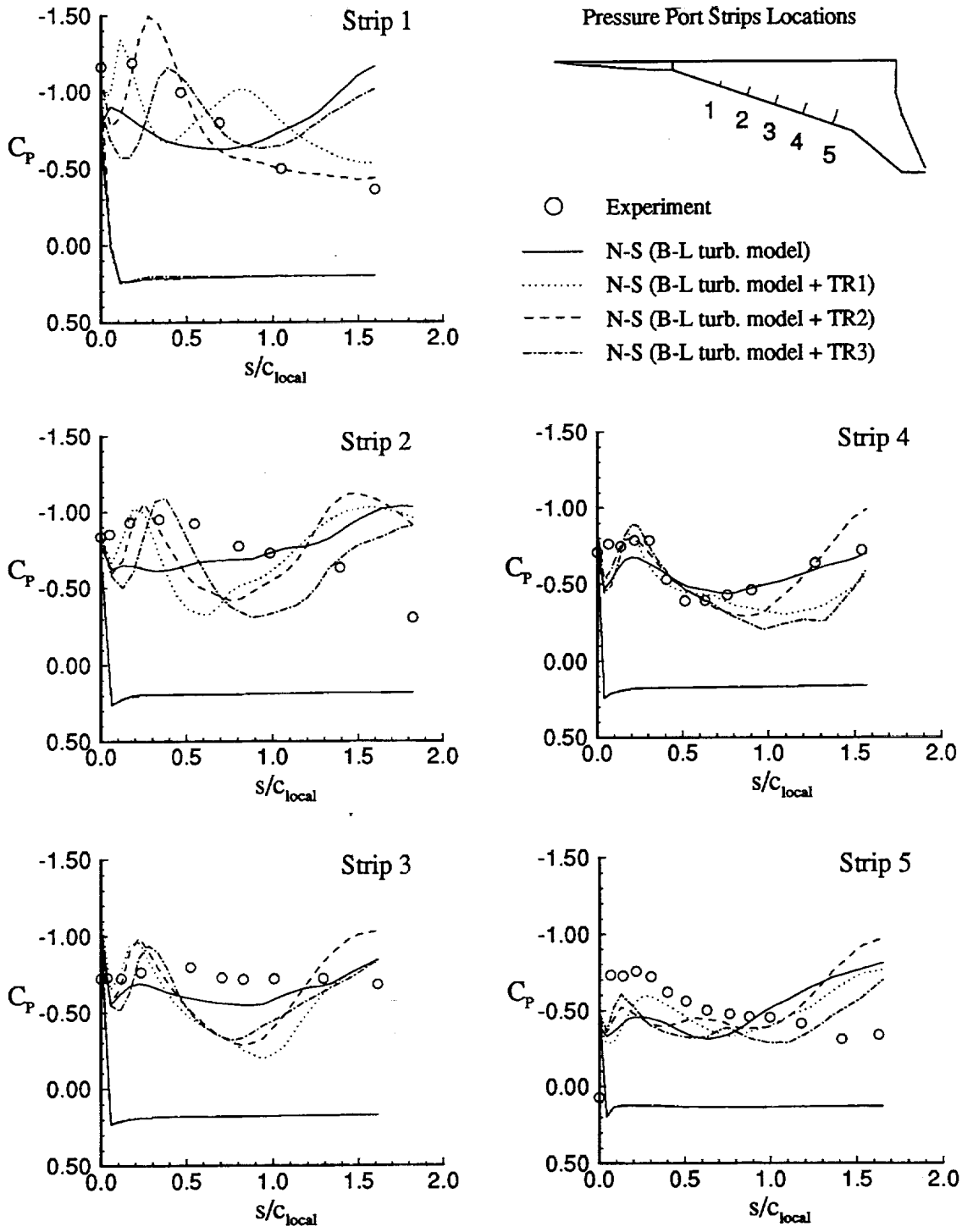

(a) Pressures on the inboard MA flap.

Figure 22. Comparisons of predicted and experimental pressure coefficents for the flow conditions of M=0.22, Re_L=1.39x10^6/ft. and α=11.9°. Results are obtained using B-L turbulence model with and without transition.

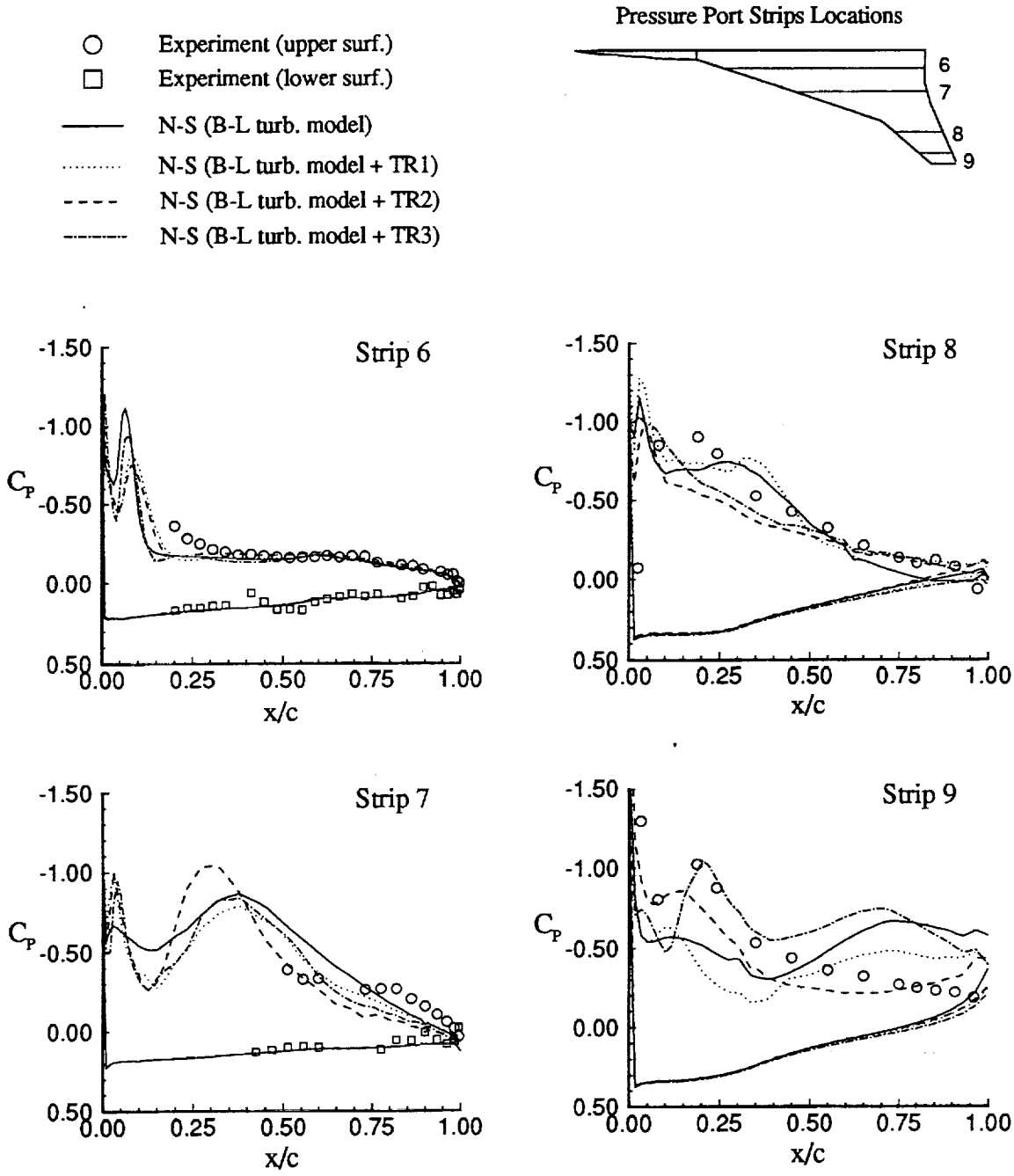

(b) Butt-line pressures on the inboard and outboard wing sections.

Figure 22. Concluded.

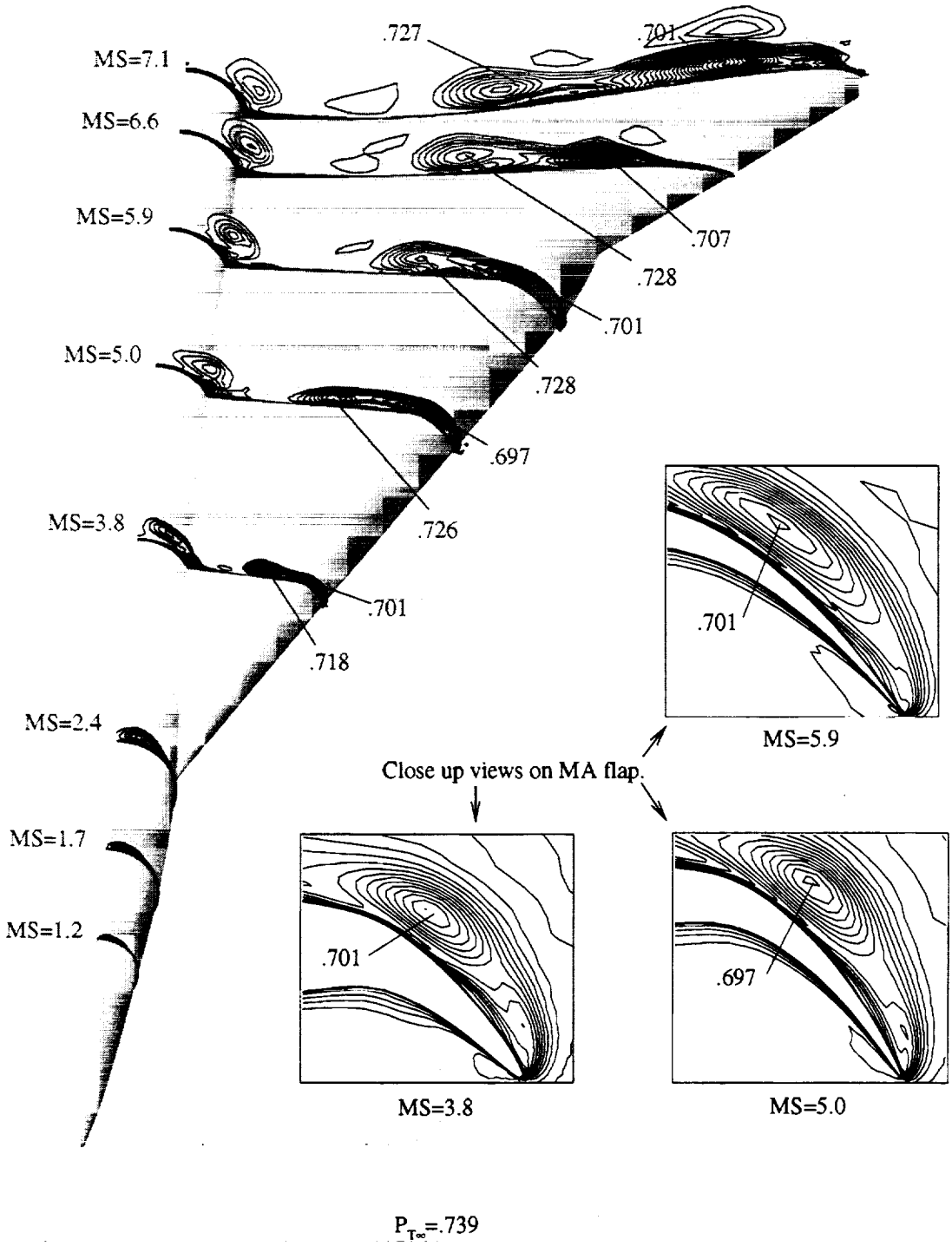

Figure 23. Predicted off-body normalized total pressure contours for α=11.9°. Solution obtained with Baldwin-Lomax turbulence model.

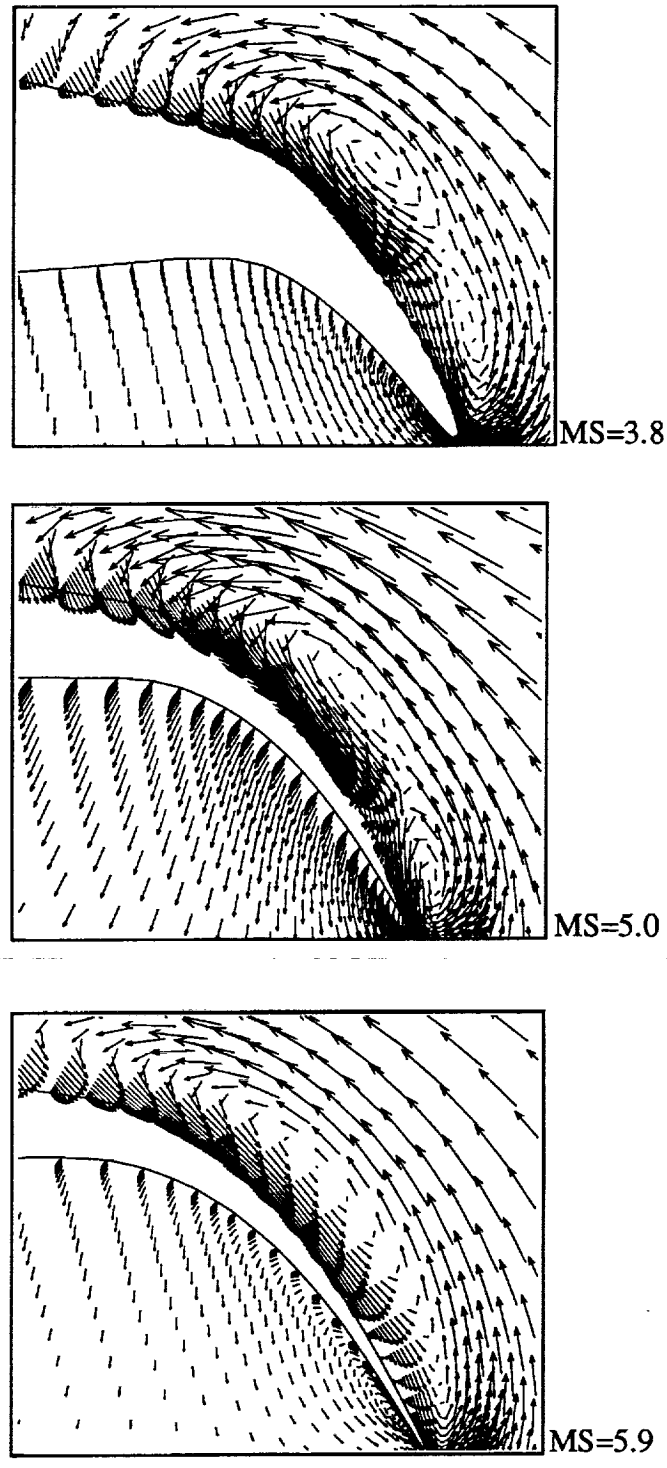

Figure 24. Cross-flow velocity vectors on the MA Flap at three model stations for α=11.9°. Solution obtained with Baldwin-Lomax turbulence model.

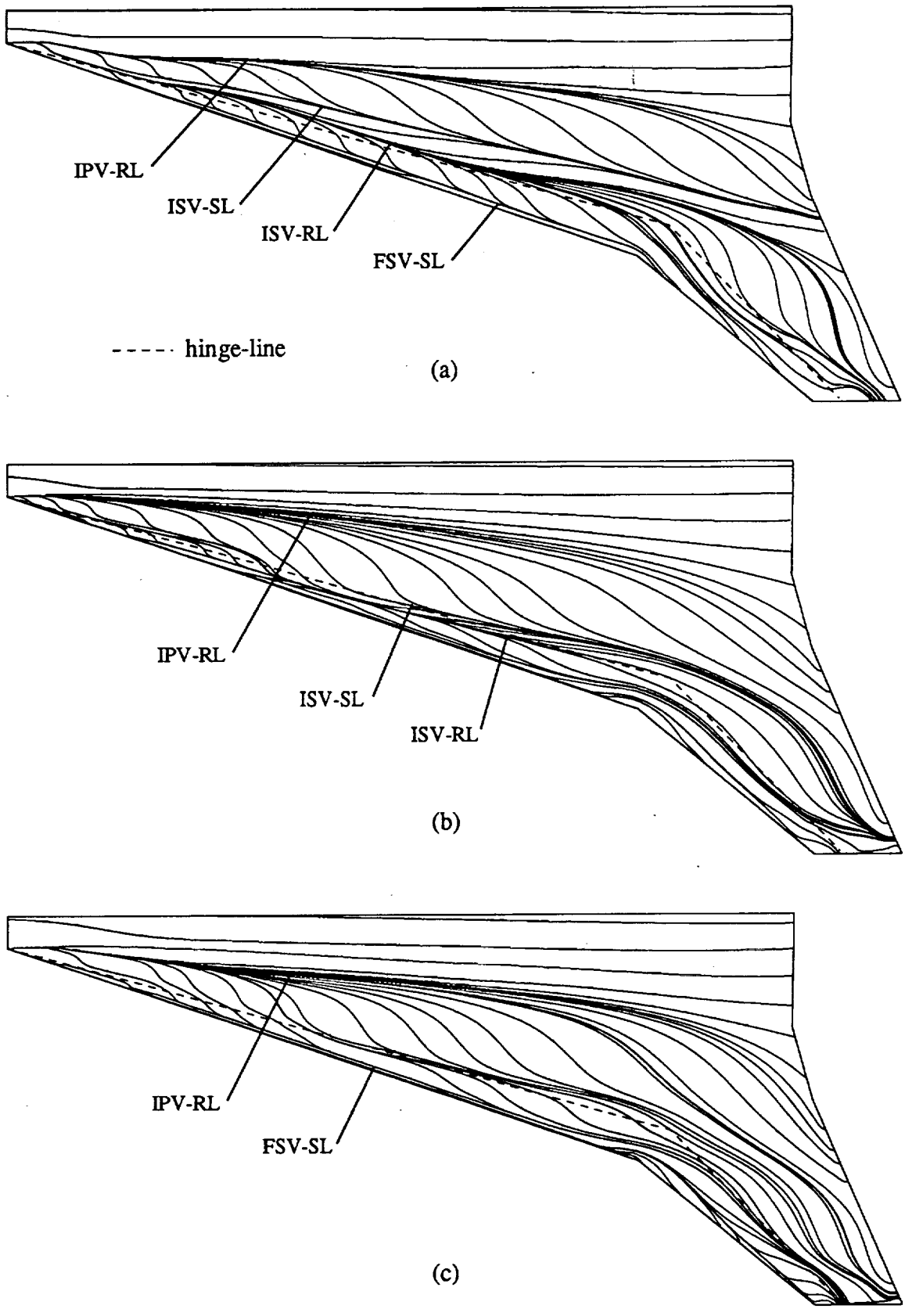

Figure 25. Computed upper surface limiting streamlines for α=11.9° using different transition locations: (a) no transition, (b) transition TR1, (c) transition TR2, (d) transition TR3. Baldwin-Lomax turbulence model was used.

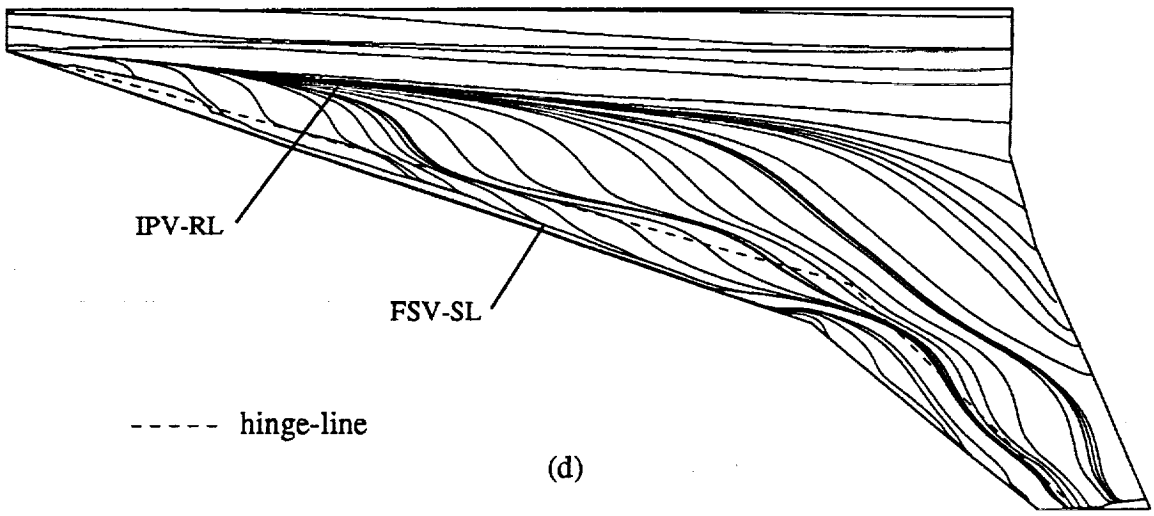

Figure 25. Concluded.

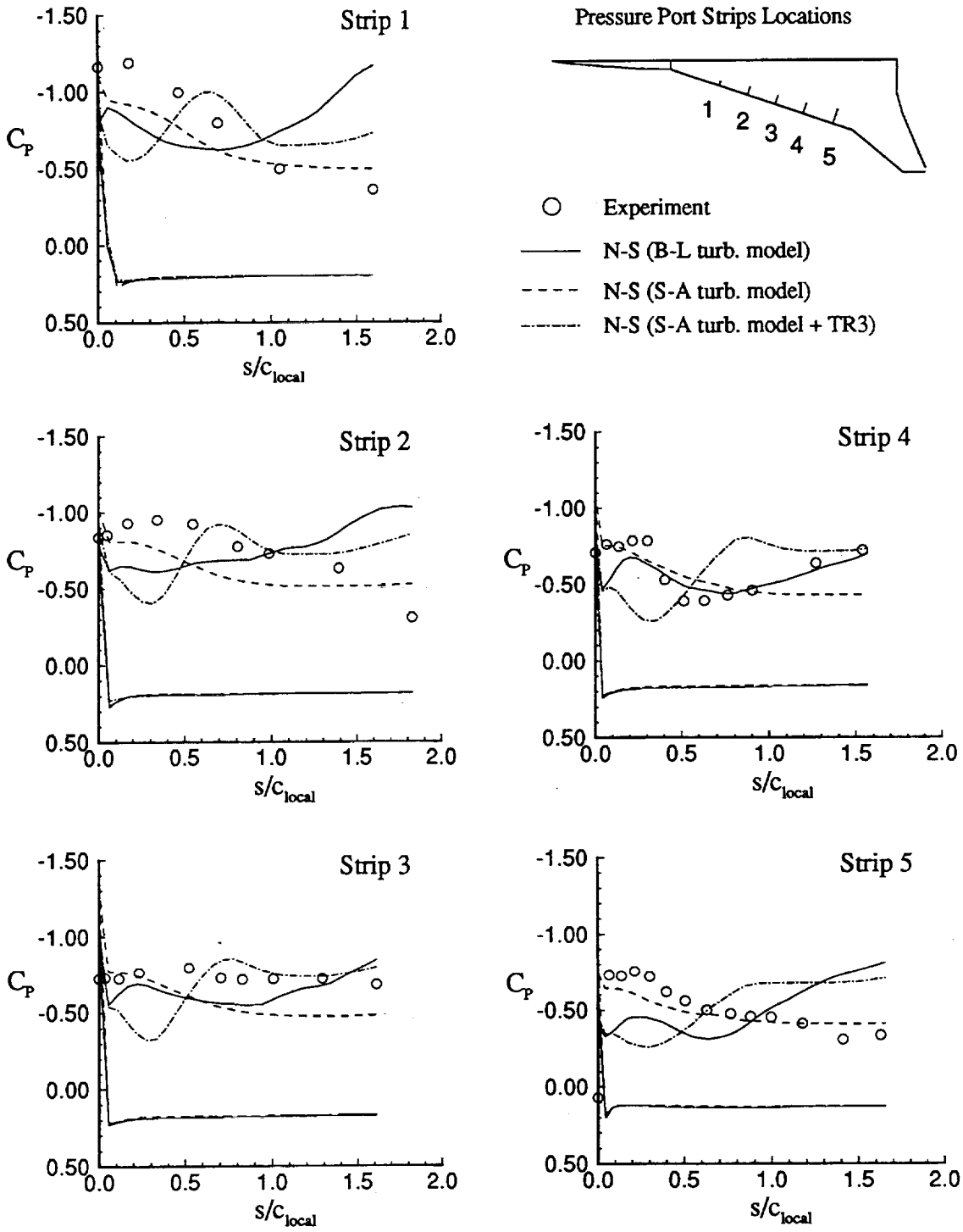

(a) Pressures on the inboard MA flap.

Figure 26. Comparison of predicted and experimental pressure coefficents for the flow conditions of M=0.22, Re_L=1.39x10^6/ft. and α=11.9°. Results are obtained using B-L and S-A turbulence models.

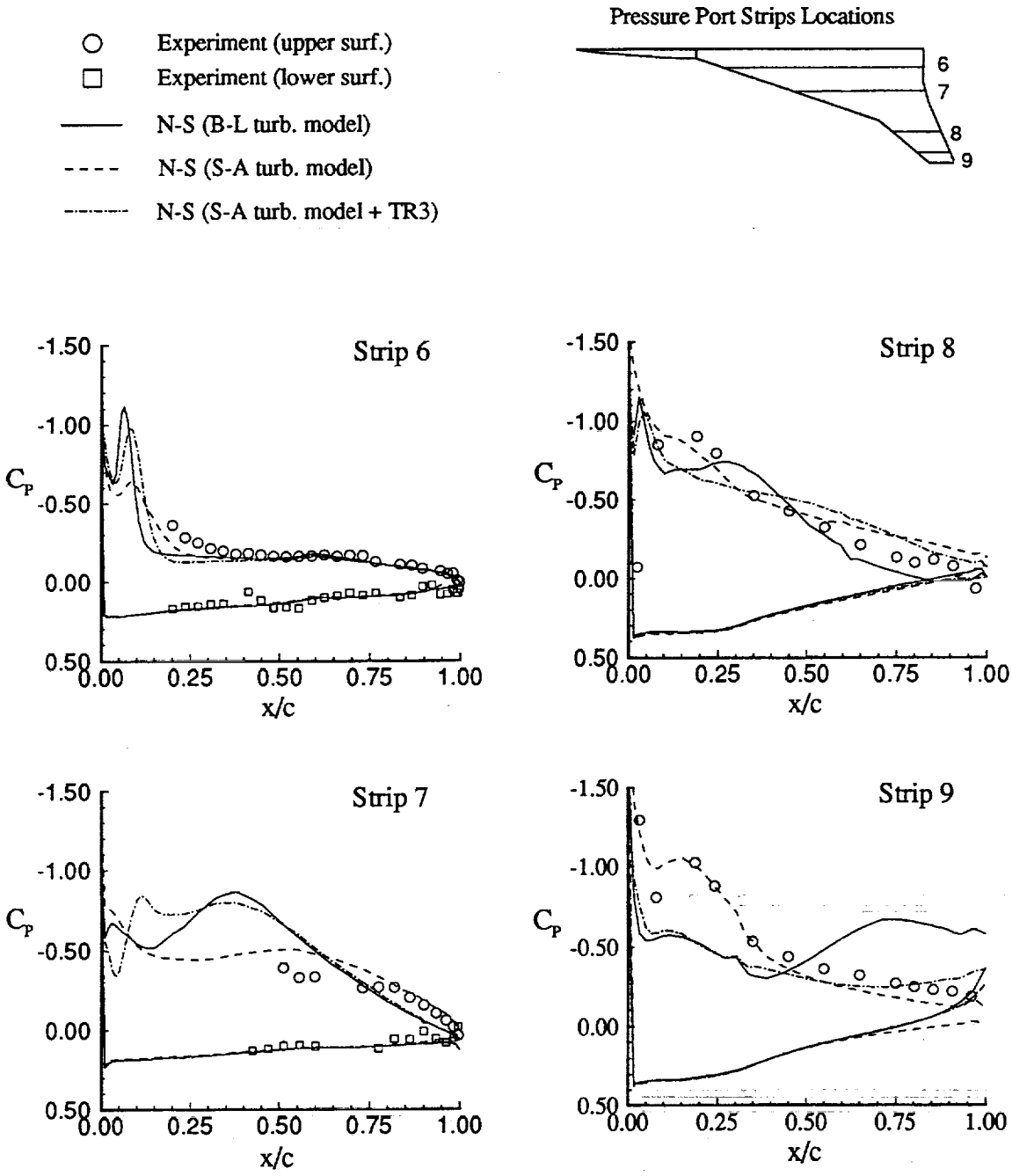

(b) Butt-line pressures on the inboard and outboard wing sections.

Figure 26. Concluded.

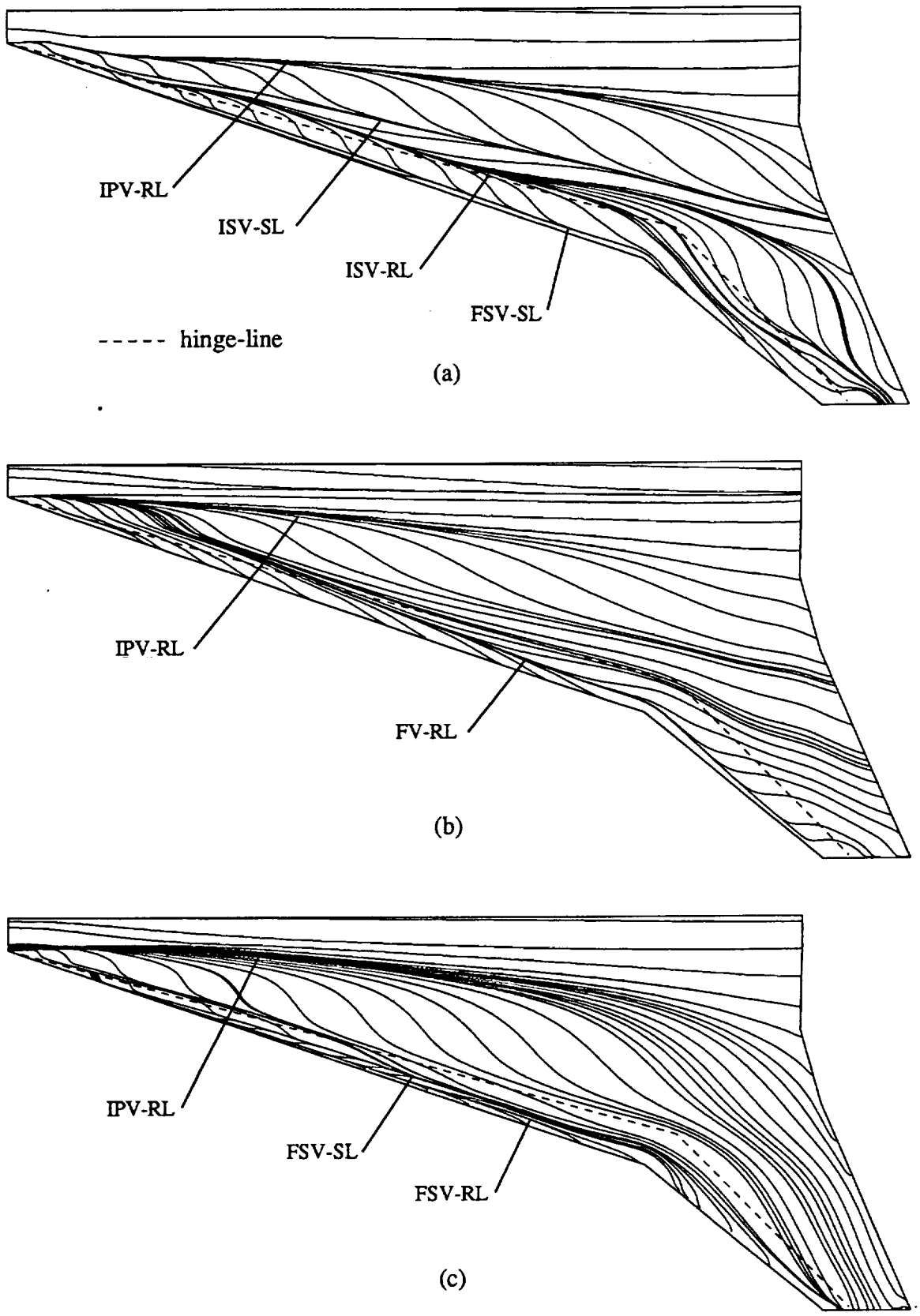

Figure 27. Computed upper surface limiting streamlines for α=11.9° using different turbulence models: (a) Baldwin-Lomax, (b) Spalart-Allmaras, (c) Spalart-Allmaras with transition TR3.

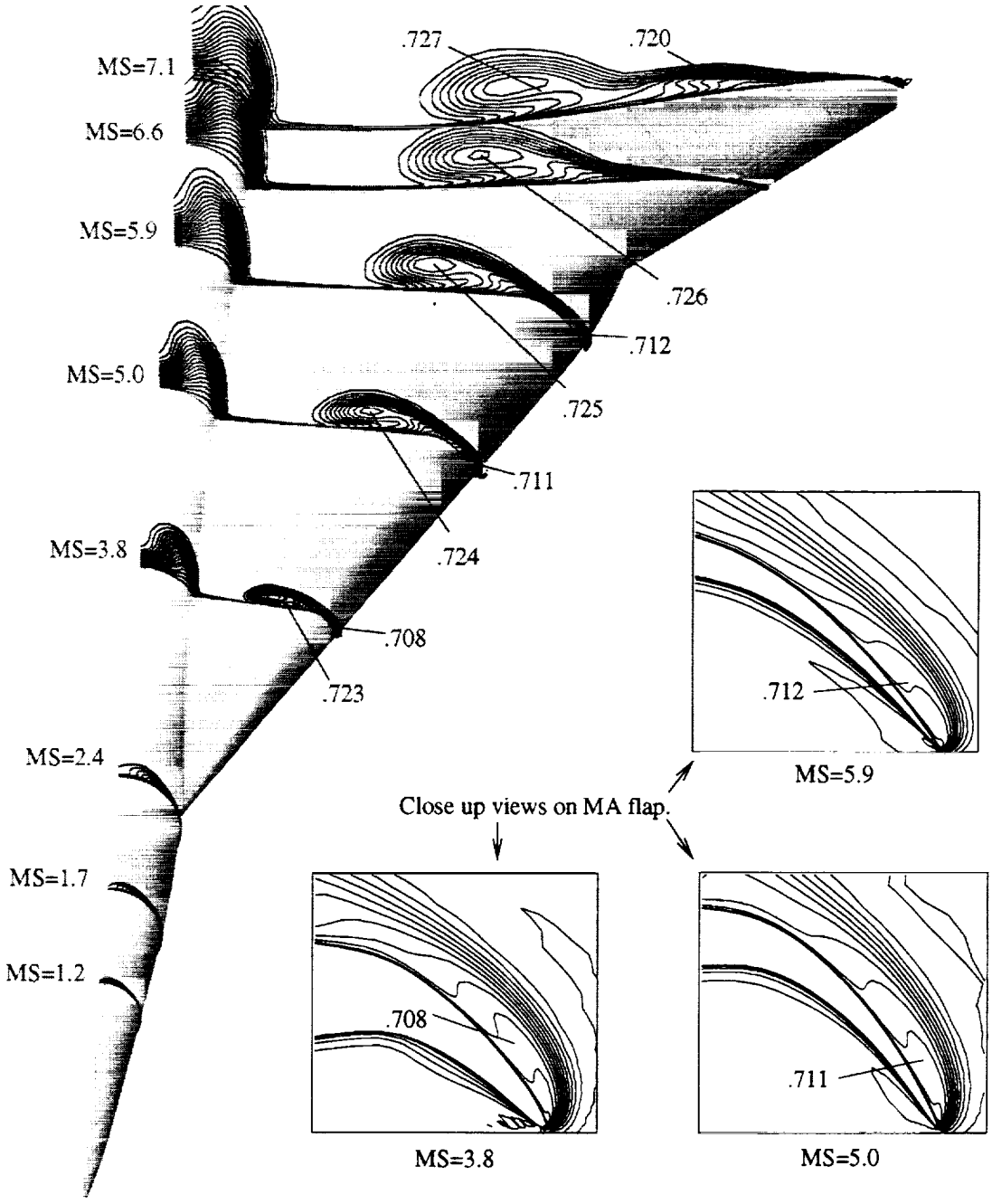

Figure 28. Predicted off-body normalized total pressure contours for α=11.9°. Solution obtained with Spalart-Allmaras turbulence model.

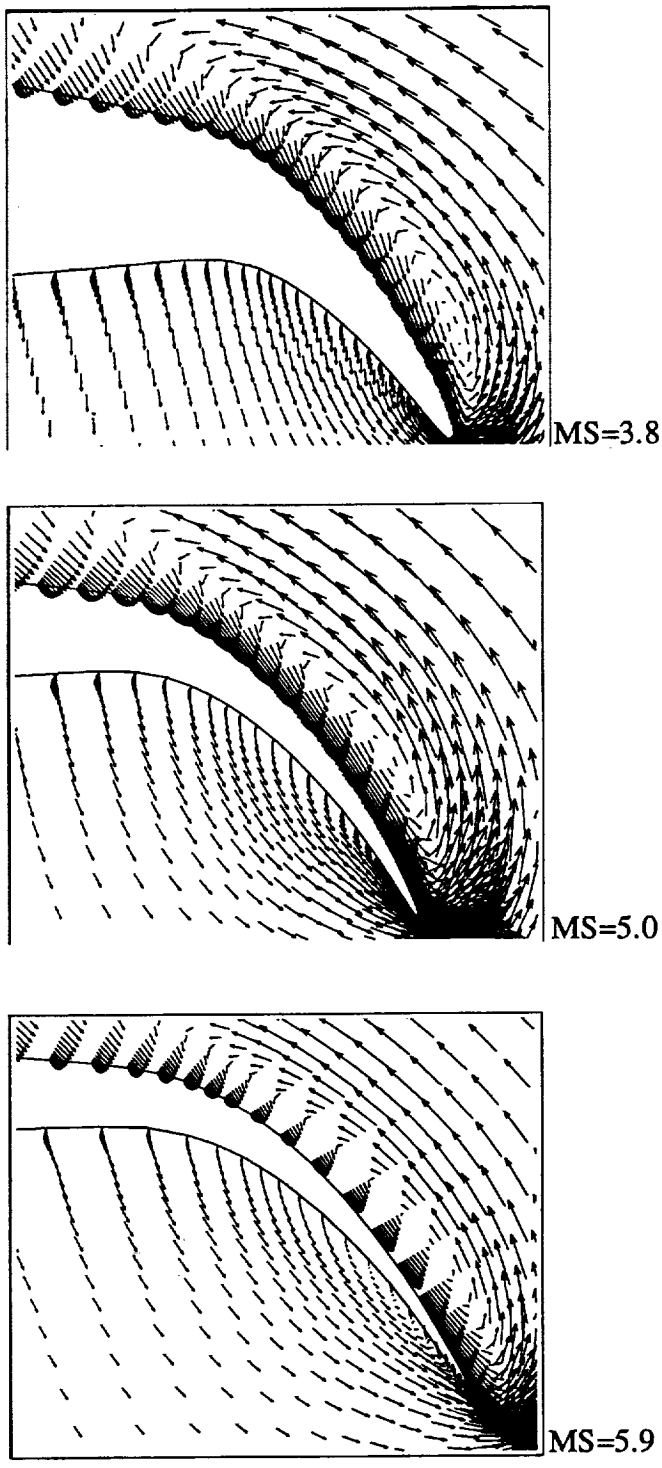

Figure 29. Cross-flow velocity vectors on the MA Flap at three model stations for α=11.9°. Solution obtained with Spalart-Allmaras turbulence model.

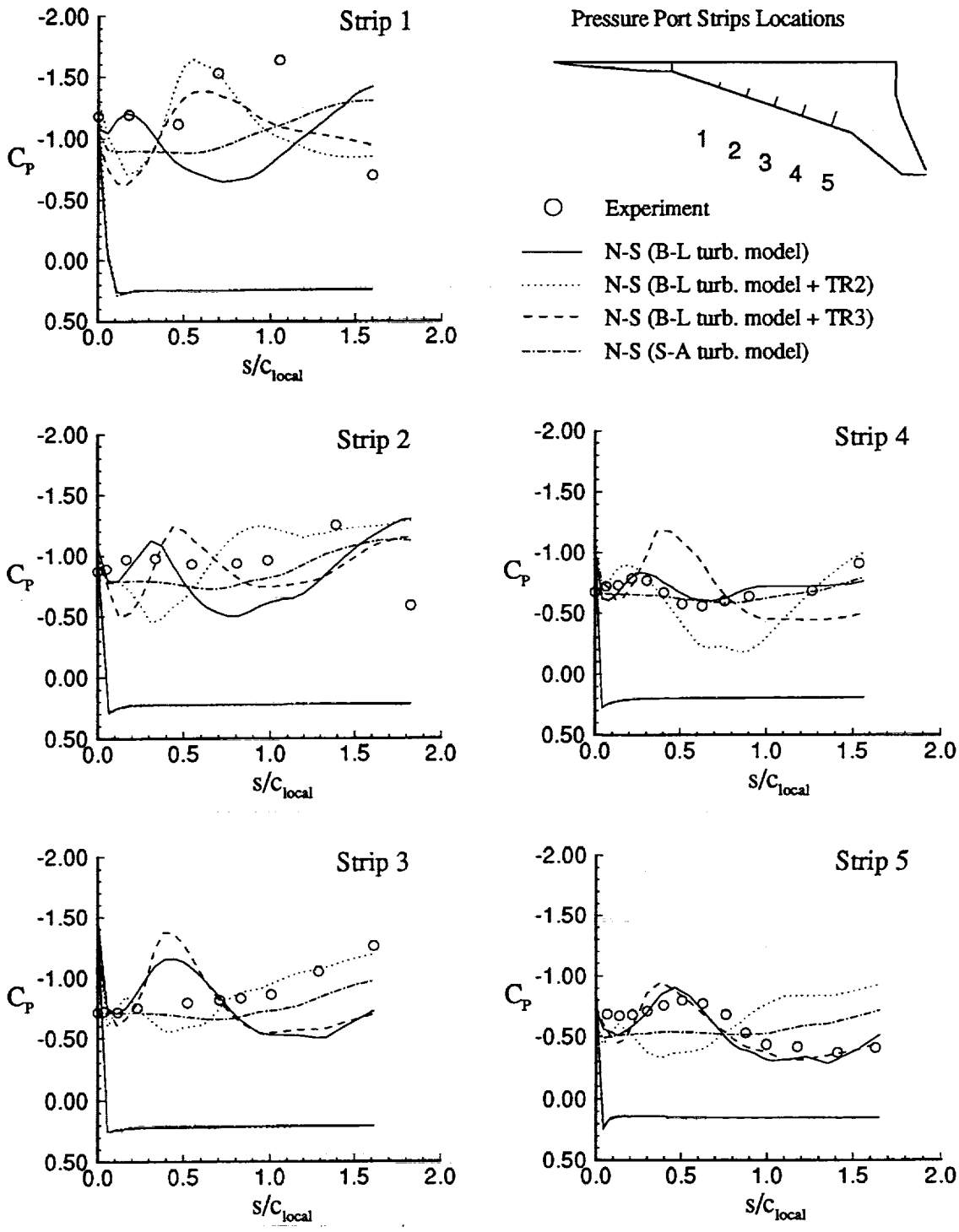

(a) Pressures on the inboard MA flap.

Figure 30. Comparisons of predicted and experimental pressure coefficents for the flow conditions of M=0.22, Re_L=1.39x10^6/ft. and α=14.1°. Results are obtained using B-L with and without transition and S-A turbulence models.

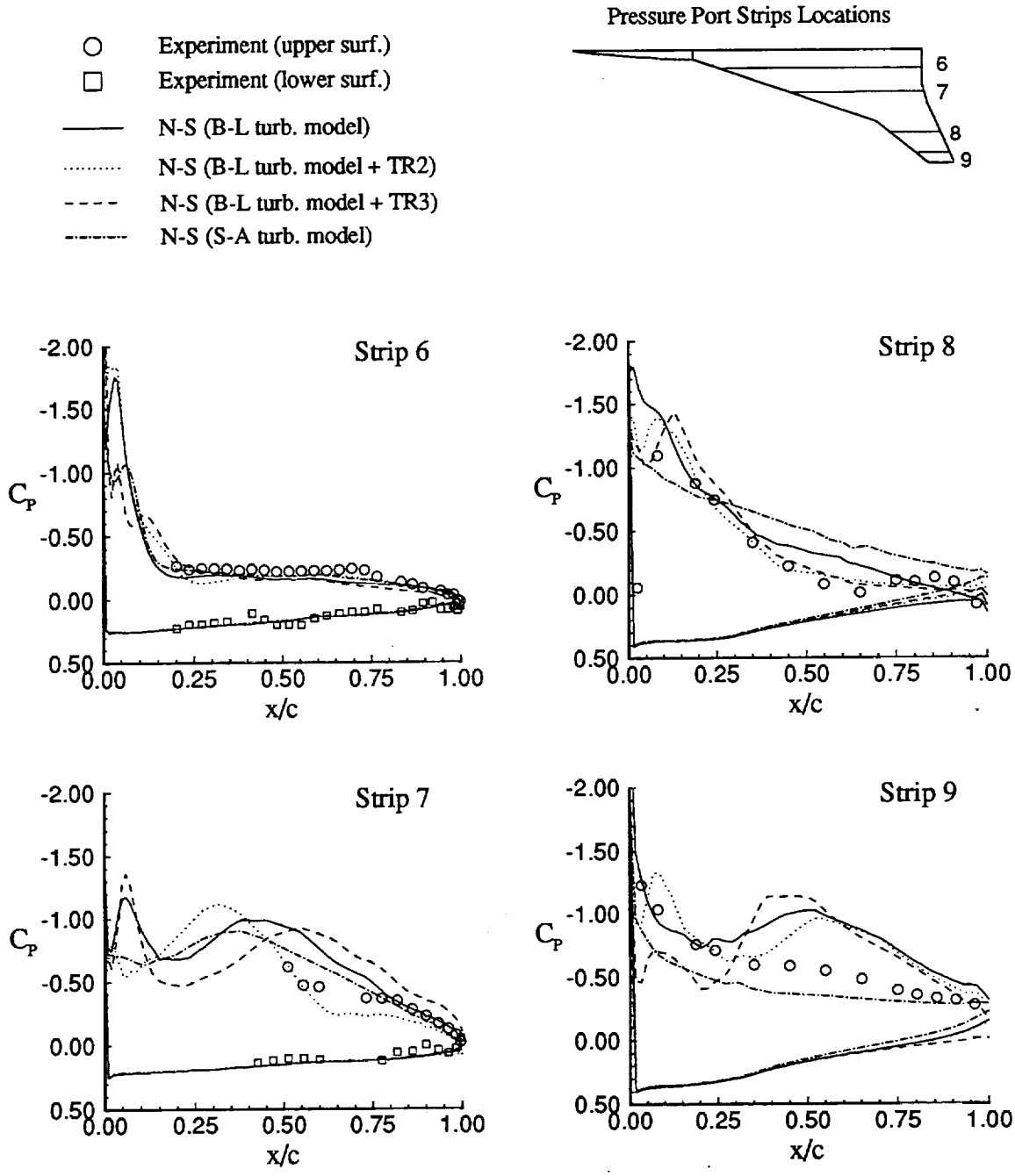

(b) Butt-line pressures on the inboard and outboard wing sections.

Figure 30. Concluded.

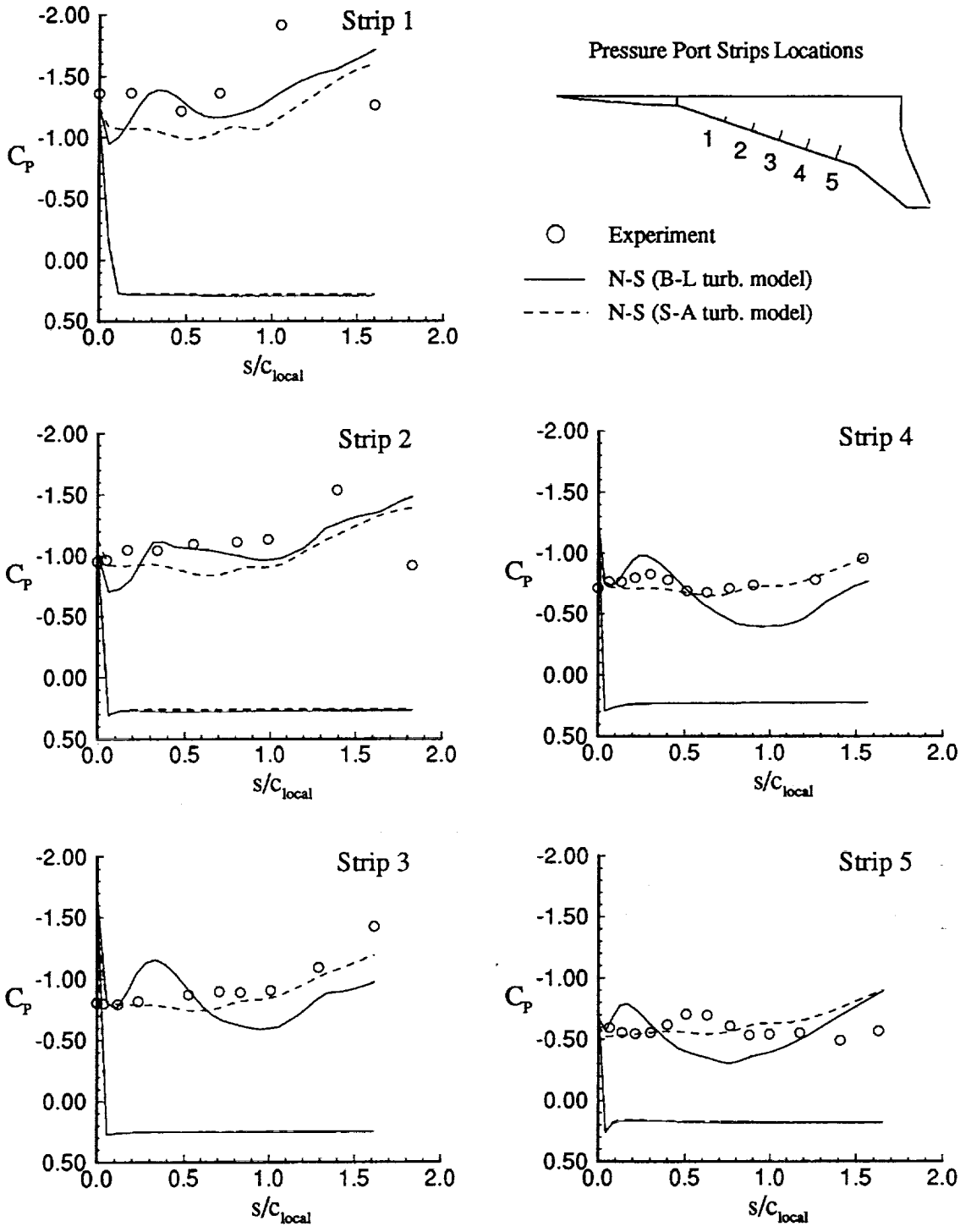

(a) Pressures on the inboard MA flap.

Figure 31. Comparisons of predicted and experimental pressure coefficents for the flow conditions of M=0.22, Re_L 1.39x10^6/ft. and α=16.1°. Results are obatined using B-L and S-A turbulence models.

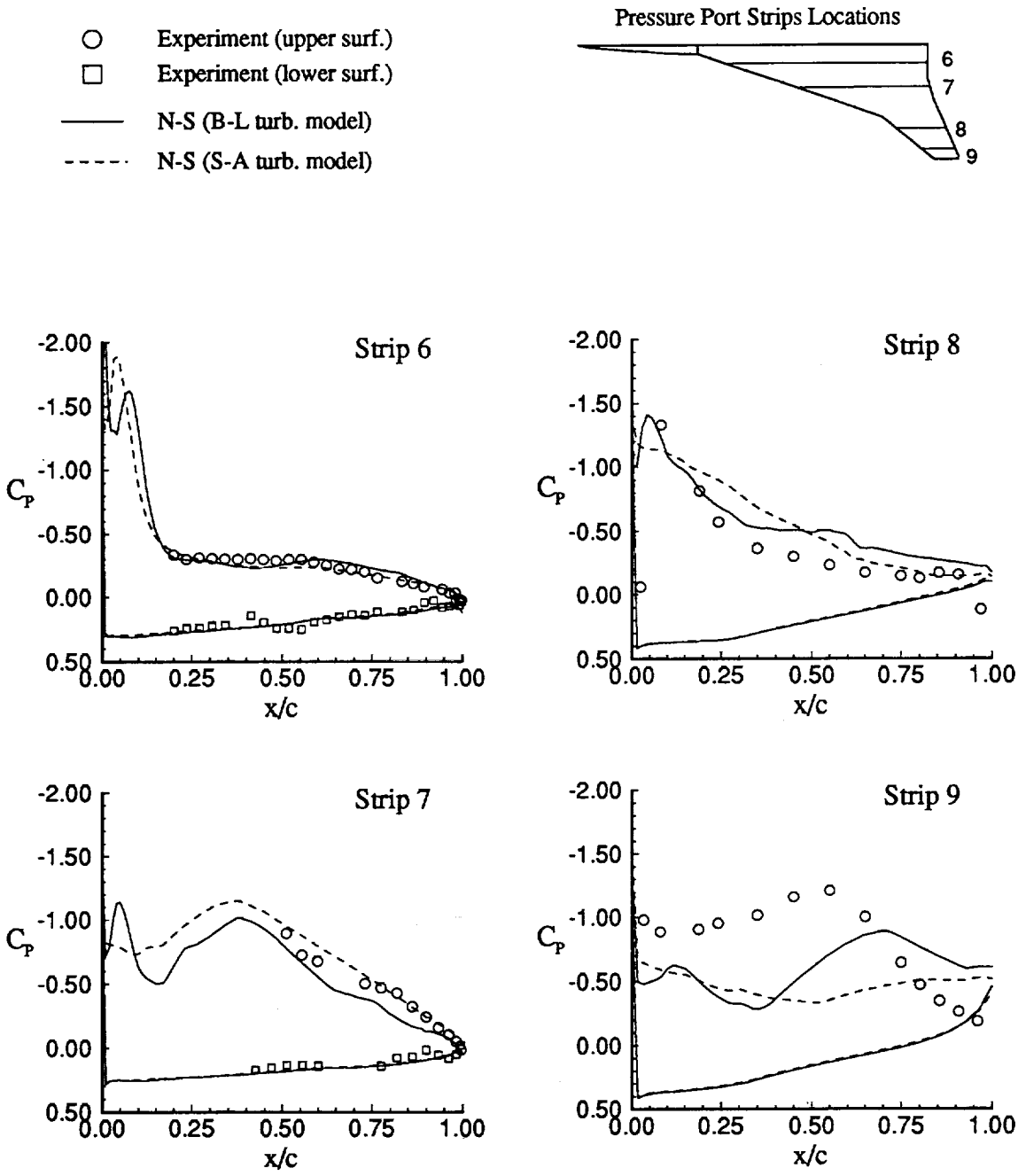

(b) Butt-line pressures on the inboard and outboard wing sections.

Figure 31. Concluded.

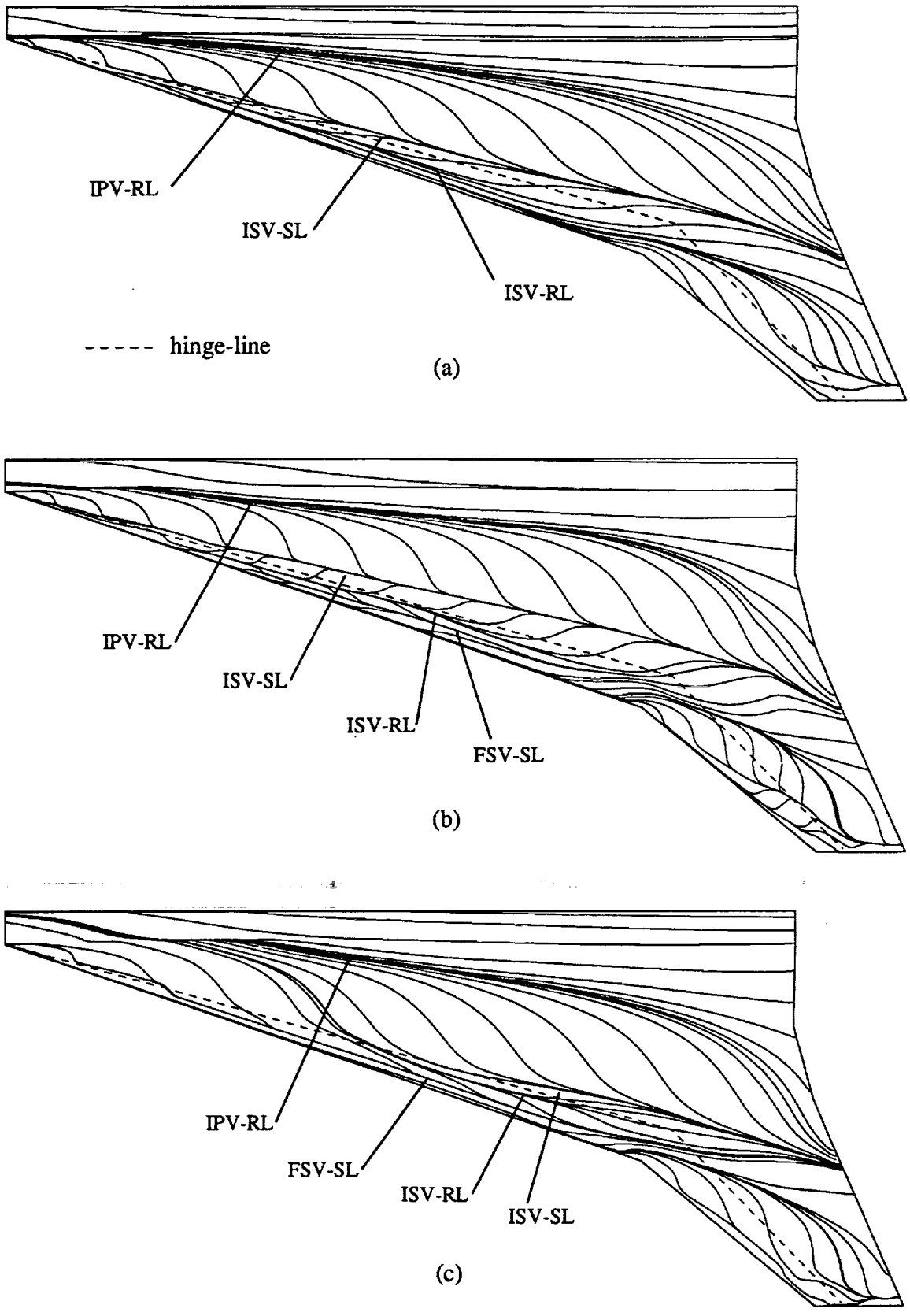

Figure 32. Computed upper surface limiting streamlines for α=14.1° using different turbulence models: (a) Baldwin-Lomax, (b) Baldwin-Lomax with TR2, (c) Baldwin-Lomax with TR3, (d) Spalart-Allmaras.

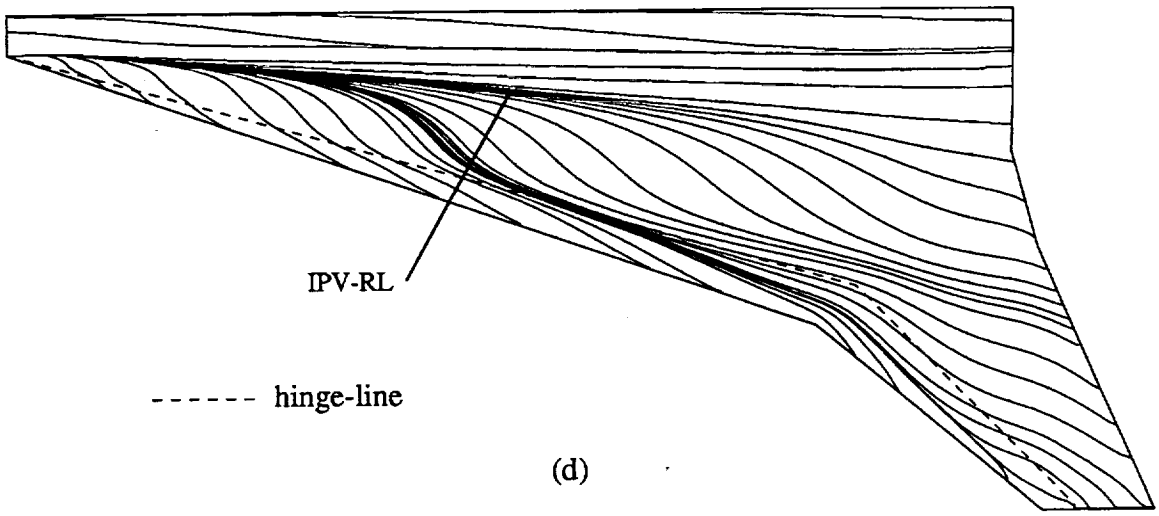

Figure 32. Concluded.

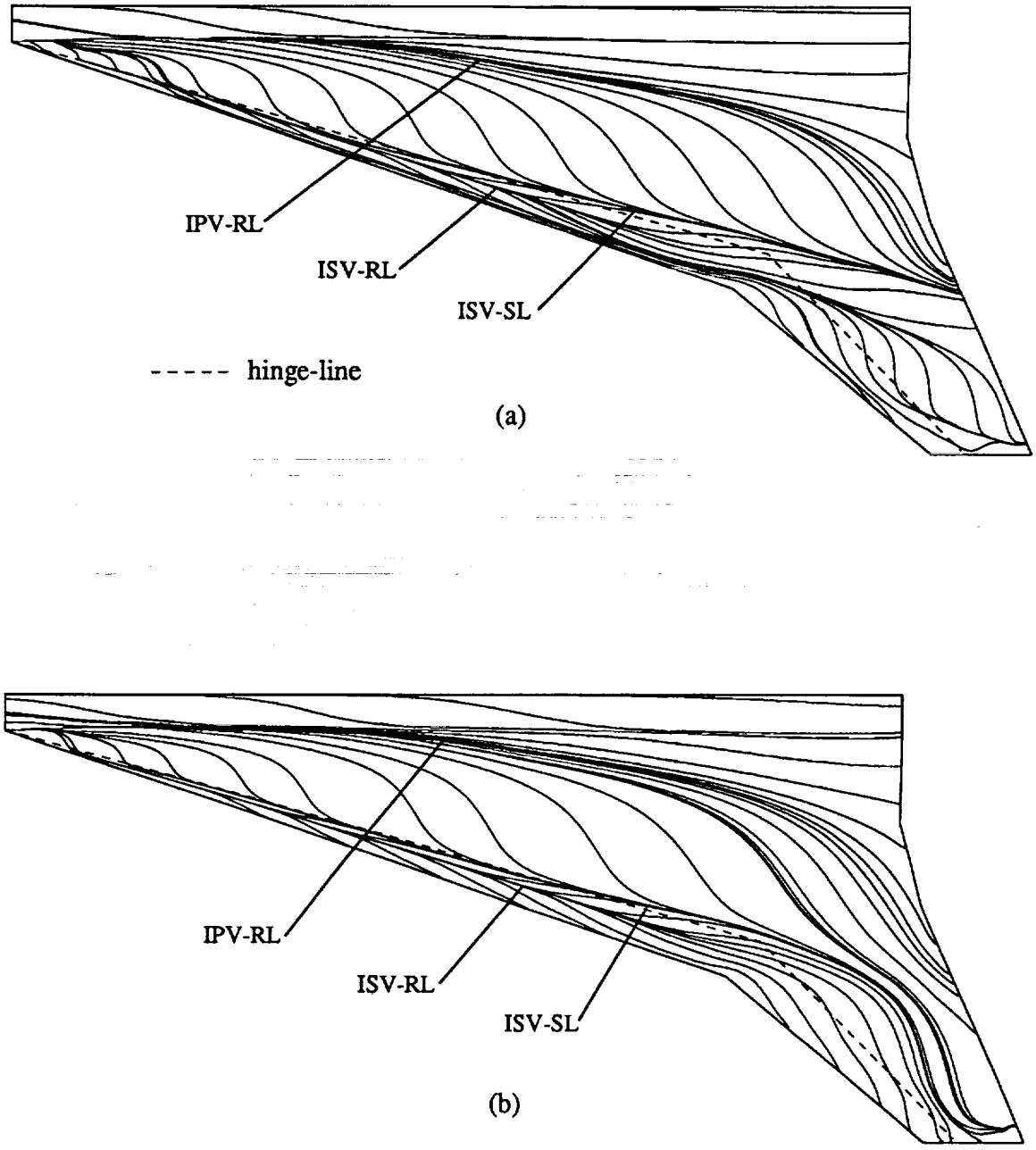

Figure 33. Computed upper surface limiting streamlines for α=16.1° using different turbulence models: (a) Baldwin-Lomax, (b) Spalart-Allmaras.

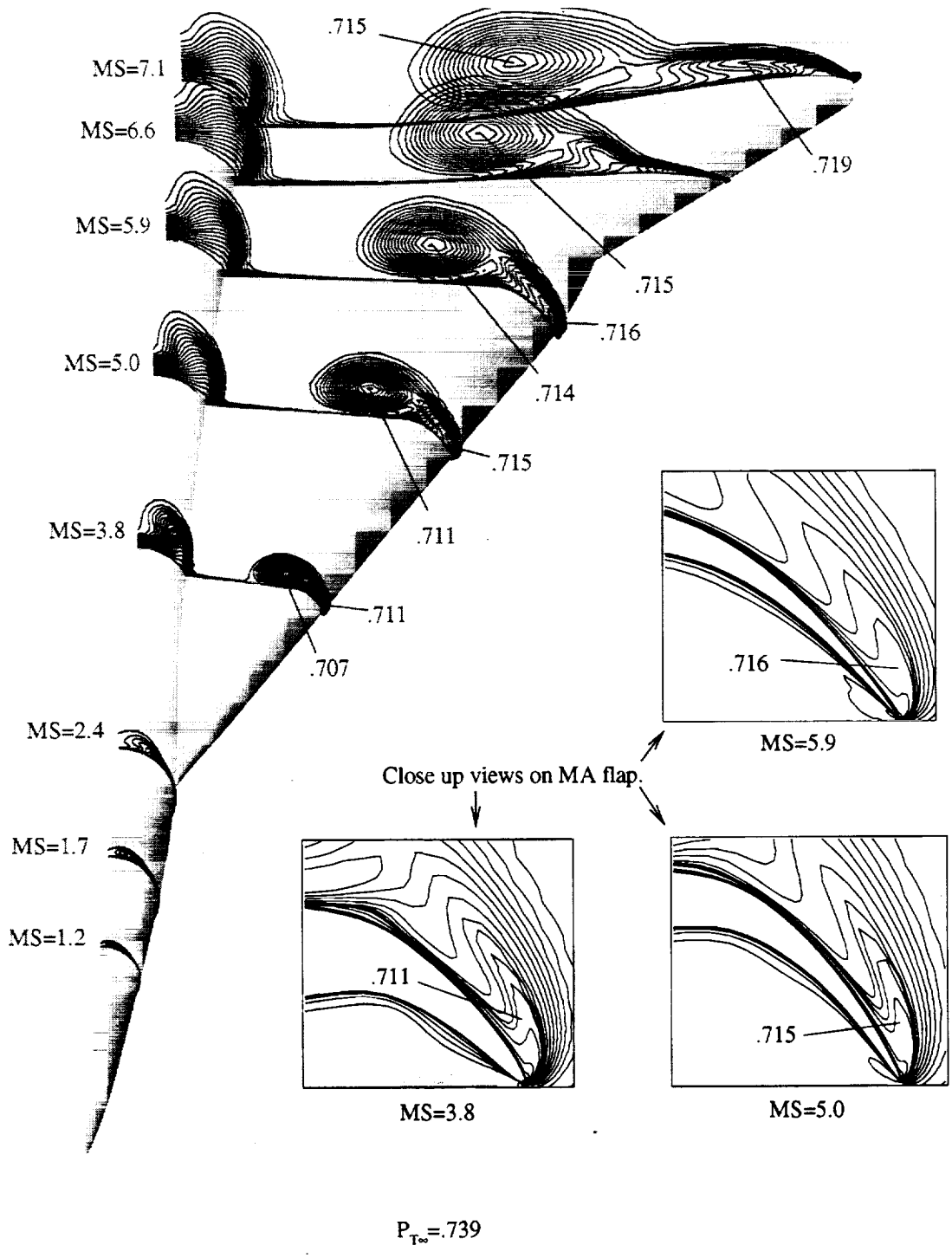

Figure 34. Predicted off-body normalized total pressure contours for α=14.1°. Solution obtained with Spalart-Allmaras turbulence model.

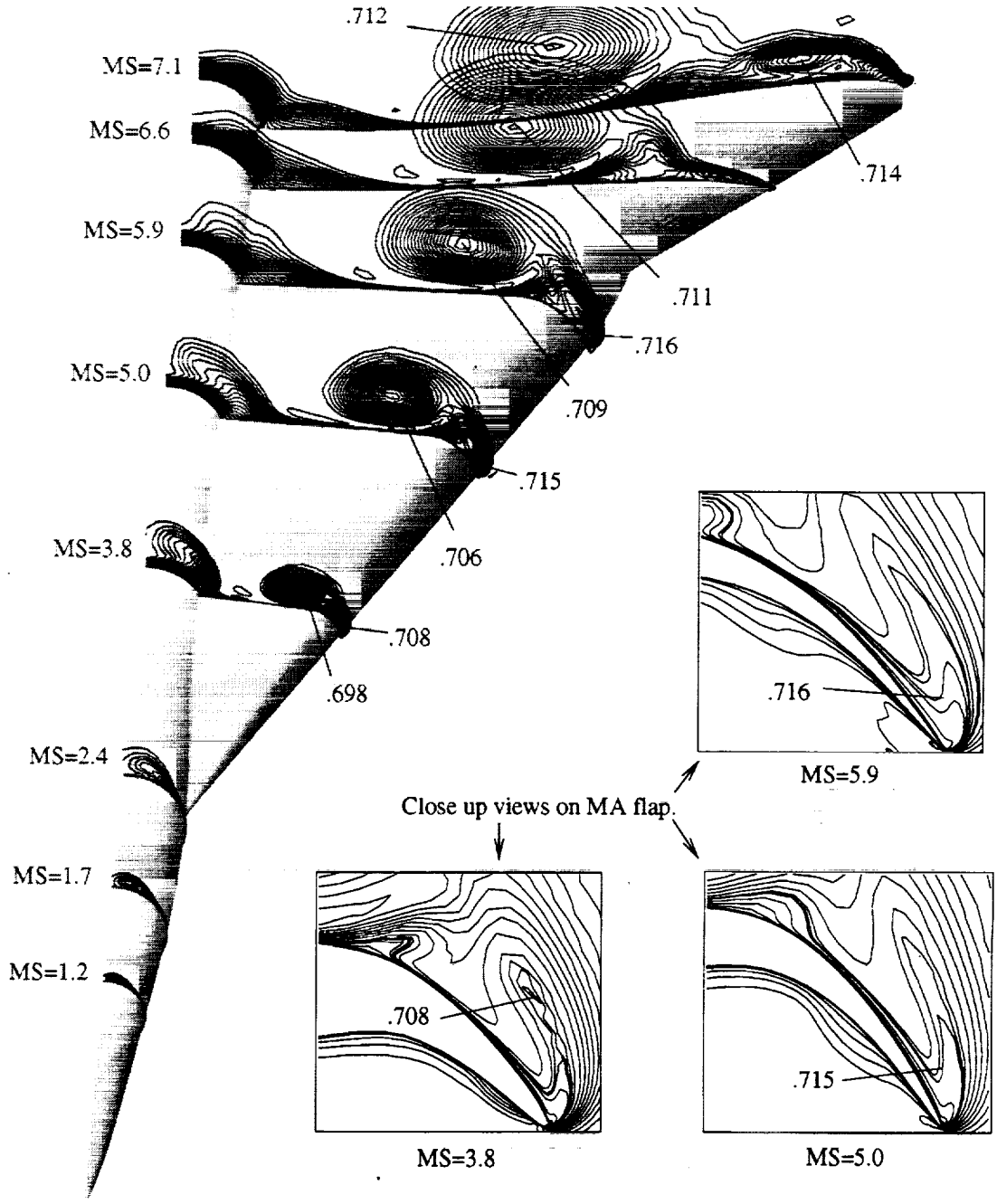

Figure 35. Predicted off-body normalized total pressure contours for α=16.1°. Solution obtained with Spalart-Allmaras turbulence model.

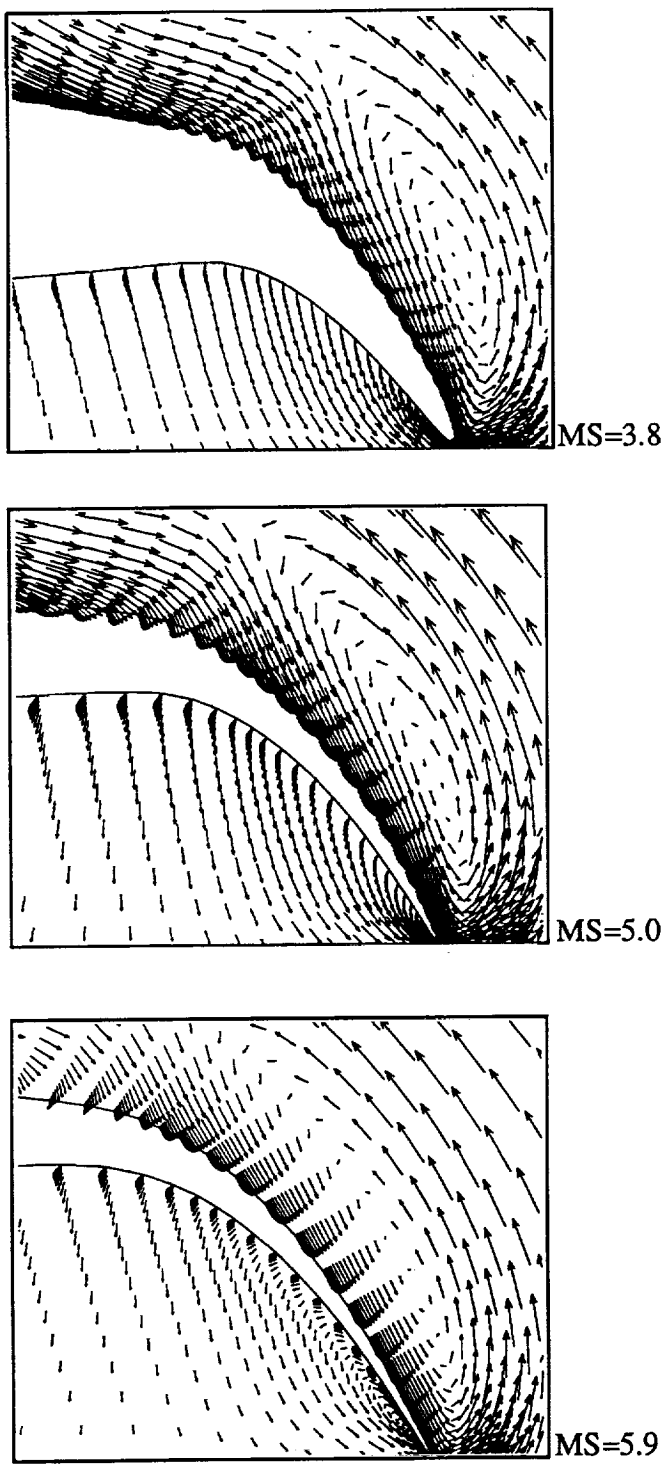

Figure 36. Cross-flow velocity vectors on the MA Flap at three model stations for α=14.1°. Solution obtained with Spalart-Allmaras turbulence model.

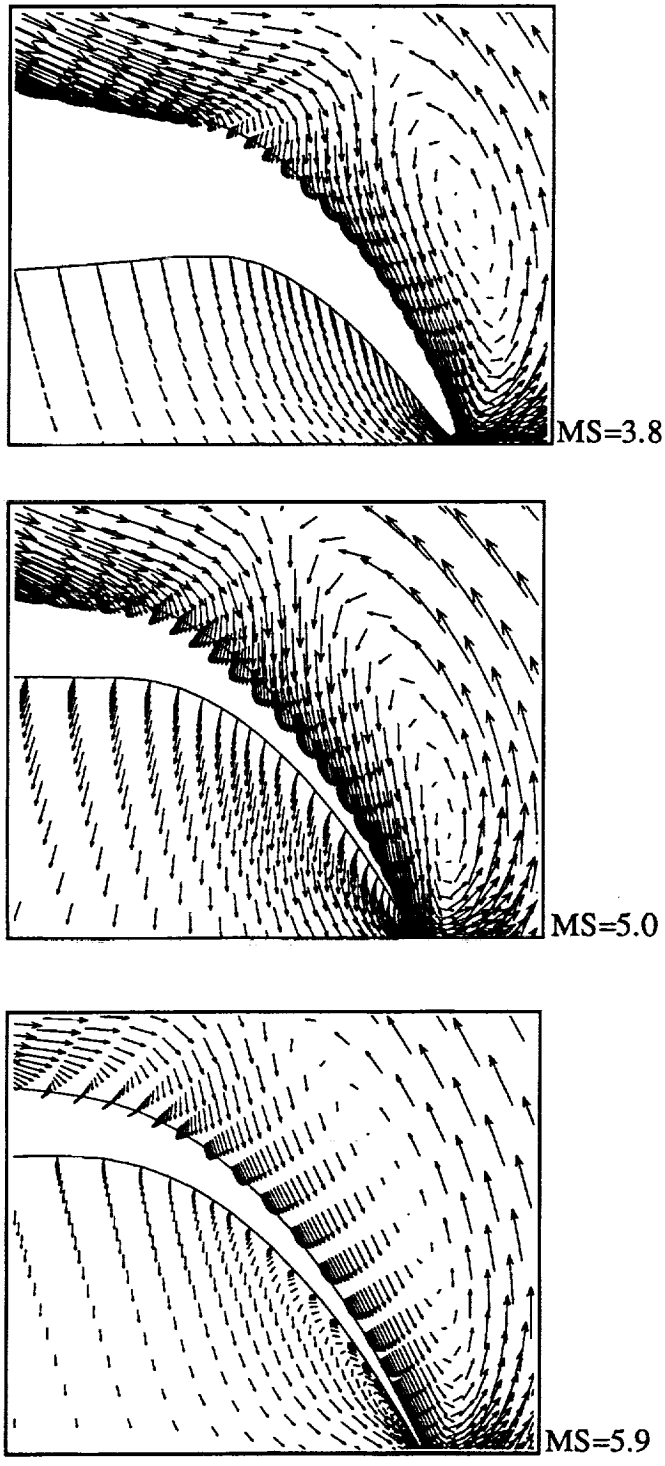

Figure 37. Cross-flow velocity vectors on the MA Flap at three model stations for α=16.1°. Solution obtained with Spalart-Allmaras turbulence model.

REPORT DOCUMENTATION PAGE

Form Approved
OMB No. 0704-0188

1. AGENCY USE ONLY *(Leave blank)*	2. REPORT DATE	3. REPORT TYPE AND DATES COVERED
	December 1999	Contractor Report

4. TITLE AND SUBTITLE
Low Speed Analysis of Mission Adapive Flaps on a High Speed Civil Transport Configuration

5. FUNDING NUMBERS
C NAS1-19672

WU 537-07-22

6. AUTHOR(S)
Victor R. Lessard

7. PERFORMING ORGANIZATION NAME(S) AND ADDRESS(ES)
ViGYAN, Inc.
30 Research Drive
Hampton, VA 23666

8. PERFORMING ORGANIZATION REPORT NUMBER

9. SPONSORING/MONITORING AGENCY NAME(S) AND ADDRESS(ES)
National Aeronautics and Space Administration
Langley Research Center
Hampton, VA 23681-2199

10. SPONSORING/MONITORING AGENCY REPORT NUMBER
NASA/CR-1999-209524

11. SUPPLEMENTARY NOTES
Langley Technical Monitor: Guy T. Kemmerly

12a. DISTRIBUTION/AVAILABILITY STATEMENT
Unclassified–Unlimited
Subject Category 02 Distribution: Nonstandard
Availability: NASA CASI (301) 621-0390

12b. DISTRIBUTION CODE

13. ABSTRACT *(Maximum 200 words)*

Thin-layer Navier-Stokes analyses were done on a high speed civil transport configuration with mission adaptive leading-edge flaps. The flow conditions simulated were Mach = 0.22 and Reynolds number of 4.27 million for angles-of-attack ranging from 0 to 18 degrees. Two turbulence closure models were used. Analyses were done exclusively with the Baldwin-Lomax turbulence model at low angle-of-attack conditions. At high angles-of-attack where considerable flow separation and vortices occurred the Spalart-Allmaras turbulence model was also considered. The effects of flow transition were studied. Predicted aerodynamic forces, moment, and pressure are compared to experimental data obtained in the 14- by 22-Foot Subsonic Tunnel at NASA Langley. The forces and moments correlated well with experimental data in terms of trends. Drag and pitching moment were consistently underpredicted. Predicted surface pressures compared well with experiment at low angles-of-attack. Above 10 angle-of-attack the pressure comparisons were not as favorable. The two turbulent models affected the pressures on the flap considerably and neither produced correct results at the high angles-of-attack.

14. SUBJECT TERMS
High speed research; High Speed Civil Transport

15. NUMBER OF PAGES
81

16. PRICE CODE
A05

17. SECURITY CLASSIFICATION OF REPORT	18. SECURITY CLASSIFICATION OF THIS PAGE	19. SECURITY CLASSIFICATION OF ABSTRACT	20. LIMITATION OF ABSTRACT
Unclassified	Unclassified	Unclassified	UL